The Development of Radiofrequency Imaging Techniques and Compact NMR Systems to Improve Access to Medical Technology

A THESIS
SUBMITTED TO THE FACULTY OF THE GRADUATE SCHOOL
OF THE UNIVERSITY OF MINNESOTA
BY

Efraín Torres Jr.

IN PARTIAL FULFILLMENT OF THE REQUIREMENTS
FOR THE DEGREE OF
DOCTOR OF PHILOSOPHY

Advisor: Michael Garwood

September 2023

Acknowledgements

I would first like to thank my advisor: Professor Michael Garwood. I first came to Dr. Garwood during my junior year of my undergraduate years. I emailed him enthusiastically, asked to speak with him in person, and met him during that summer. I was amazed by his creative spark, enthusiasm for the field, and motivation to develop novel, cutting edge technology. I left our first meeting with him, and Dr. Garwood emailed me stating that he was ”Excited to work on science with me.” I was as well, and these past four years have been everything and more than I could have imagined. He has trained, mentored, and guided in me what it means to develop impactful solutions.

I would like to thank all members of the Garwood lab and the Center for Magnetic Resonance Research (CMRR). The group and research center is truly unique and a place where innovation can flourish. I would like to in particular thank Dr. Michael Mullen. Dr. Mullen helped teach me MRI physics, answered the hundreds of questions I asked him, and aided me in anything else that I asked him. I learned a tremendous amount from him, and I continue to till this day. I would also like to thank CIERMag and their wonderful group of researchers. CIERMag is a wonderful group of researchers who make our work possible. Without them, and their cutting-edge spectrometer system, we would not have been able to develop our approaches and implement them so rapidly on our systems. In particular, I would like to thank Dr. Daniel Pizetta. Dr. Pizetta, throughout my PhD years, was extremely supportive in solving software bugs that I reported and in training me to utilize the spectrometer. I would also like to thank Parker Jenkins. Parker and I attended our undergraduate years together, and when he joined the Garwood lab. I was thrilled to have him be formally a part of the team. Parker is a highly creative and hard working friend who is a thrill to work with. So much so that we started a company together to further the mission.

Lastly, but most importantly, I would like to thank my family. My soon-to-be wife Sarah has supported me throughout my entire PhD journey. She has been there during the ups and downs and has been a constant support system as I have pushed both the edge of my work and myself in pursuit of impactful technology. Without her by my side every day, I could not have accomplished this. I would like to thank my family and my brothers. Everything that I have done and will do are for them and my community. My parents immigrated to the United States without graduating from middle school, but they worked and gave everything to us. All in hopes that we could pursue this elaborate thing we call the American Dream. My father every day got up at 4am and would go do his janitorial work, and if needed he would return to work at midnight, at times pulling multiple weeks of nonstop working. He showed me what it means to work hard for your family; he showed me what it means to work with pride; and he showed me how I should approach my work. My mother took care of me and my brothers, always bringing us anywhere while she worked herself. She instilled in mean what it means to love your family and your community. Always being proud of the Mexican culture that paints our skin. To my brothers, they have served as the example. To José Luis, the first in our family to attend college. Thank you for guiding me and nurturing a fighting spirit that I carry with me today. To Julio, thank you for showing me how to retain that passion through difficulties and how to become a great and caring father. You demonstrate the strong work-ethic my family is built around, and it serves as an example for me.

And lastly, I would like to thank the obstacles that life put in my way throughout this journey. To the concussion that limited my cognitive abilities for months, to COVID that shut down my city, to the riots that locked me in my apartment, to the barriers I felt every day as one of the only Latinos in a PhD program, I am grateful for all of these experiences. Without them, I would not be who I am today. They, alongside my family, have taught me to overcome.

To Sarah, my love, who keeps me grounded and makes every day great. To my family, who gave everything for me to have a chance.

Abstract

Magnetic Resonance Imaging (MRI) is a seminal tool in modern medicine, but its high cost and complexity drastically limits its availability. MRI systems only serve approximately 10 percent of the population. A need exists to develop affordable, accessible, and clinically valuable technology. This thesis work is focused on developing technology that could make MRI systems more readily available.

First, we explored the use of a 0.5 T Halbach magnet, which is a cost-effective and lightweight alternative to traditional magnets. We successfully demonstrate how simple radiofrequency coils and adiabatic pulses can compensate for large magnetic imperfections often found in Halbach magnets. To demonstrate its clinical utility, an R_1 relaxometry study was performed on ^{19}F oxygen-probes that were implanted in tissue-engineered grafts.

Second, we challenge the conventional use of B_1 coils. Traditionally B_1 coils are only used for spin tipping. We propose and demonstrate a novel approach that enables B_1 coils to not only tip spins but also encode spatial information. This advance could eliminate the need for costly, complex, and noisy B_0 gradient coils altogether, setting the stage for a new generation of MRI systems based solely on B_1 encoding.

This thesis work aims to democratize MRI by leveraging affordable Halbach magnets and innovative B_1 encoding techniques. Our hope is that these advancements will lead to a redesign of MRI systems, making this life-saving technology much more accessible to under-served communities.

Contents

List of Tables

List of Figures

Chapter 1

Introduction

1.1 Clinical Motivation

Magnetic Resonance Imaging (MRI) is a robust imaging technique capable of structurally and functionally imaging various parts of the body. By employing radiofrequency waves and circumventing the use of ionizing radiation, unlike x-ray-based imaging approaches, it allows for both safe and repeatable imaging. With MRI, doctors have access to a wide variety of contrast types and high-resolution images, empowering them to make life-saving diagnoses. Because of this, MRI is often referred to as the 'gold standard' of medical imaging technology. It is routinely employed across multiple areas of healthcare, including cancer detection, diagnostic evaluation, and preventative imaging.

The most urgent challenges faced by modern-day MRI are not related to its clinical utility, but rather its clinical accessibility. Currently, 90 percent of the global population lacks access to MRI scanners due to their exorbitant costs [1]. The purchase, maintenance, and installation costs of MRI scanners routinely amounts to millions of USD. Consequently, MRI remains an imaging modality that is predominantly available in only the wealthiest countries and communities. Given this situation, we firmly believe that the MRI scientific community has a responsibility to reevaluate its approach and develop technology that is both highly affordable and clinically valuable.[2]

1.2 Designing a New Class of Systems

With this thesis work, we advocate for the removal of B_0 gradient coils and the utilization of highly compact and affordable magnet types to enhance affordability and accessibility.

B_0 gradient coils are primarily responsible for spatial encoding and are present in every clinical MRI scanner on the market. Currently, B_0 gradient coils constitute approximately 30 percent of the total MRI machine cost [3], occupy a substantial portion of the bore space, and significantly contribute to the noisy imaging environment that discomforts patients. By eliminating B_0 gradient coils, we not only reduce procurement and maintenance expenses but also pave the way for a more patient-friendly scanner design. However, achieving this goal requires a novel form of spatial encoding. B_1 imaging serves as a potential substitute for B_0 gradient coils. B_1 fields can spatially encode and generate images using RF coils, which are inherently cheaper than B_0 gradient coils. Although these imaging approaches have previously demonstrated success, they remain under-utilized and under-developed. A primary focus of this thesis work is to demonstrate, validate, and further develop B_1 imaging approaches so that they can fully replace B_0 gradient coils.

A second approach to reducing the cost of MRI systems involves the use of compact, inhomogeneous, and ultimately more cost-effective magnet designs. Conventional MRI magnets are low-temperature superconducting magnets, requiring liquid helium and kilometers of superconducting wire to meet stringent homogeneity requirements [4]. This thesis concentrates on the development of MRI systems that leverage significantly more affordable permanent magnet designs. The permanent magnets used in our custom systems cost one-tenth of their superconducting counterparts; however, their inherent inhomogeneity is 100 times that of clinical scanners. Our B_1 imaging approaches were intentionally designed to function within such inhomogeneous magnet environments. In this thesis, we present a methodology to redesign MRI systems.

1.3 Overview of Topics

Chapter 2 covers the fundamentals of magnetic resonance with a focus on relaxometry. Chapter 3 reviews the development of a novel low-cost, lightweight, and portable 0.5 T relaxometry system. The system is experimentally validated and demonstrated clinical utility through a ^{19}F relaxometry study with tissue engineered grafts. Chapter 4 covers the fundamentals of spatial encoding with an emphasis on both B_1 and B_0 encoding approaches. Chapter 5 presents a novel phase-encoding B_1 imaging approach named Frequency-modulated Rabi Encoded Echoes (FREE). It is validated through experimental imaging on a 1.5 T MRI scanner. Chapter 6 presents FREE's frequency-encoded method and demonstrates its viability on a 0.5 T scanner. Lastly, Chapter 7 speaks on the future of this technology, and its potential impact.

Chapter 2

Magnetic Resonance Theory

2.1 Nuclear Magnetic Resonance

To comprehend Magnetic Resonance Imaging (MRI), it is essential to study the fundamental forces at play in Nuclear Magnetic Resonance. Let us begin by examining the fundamental particles involved. Three primary subatomic particles exist: protons, neutrons, and electrons, each of which is composed of even smaller particles [5]. These particles possess inherent properties that facilitate the field of electromagnetism and, consequently, MRI. Of particular interest to MRI are two intrinsic properties: charge and spin [6].

2.1.1 Charge

Charge is an intrinsic electrical property exhibited by particles. Neutrons possess no charge, while protons and electrons carry charges of +1 and -1, respectively. These particles, due to their charge, produce an associated magnetic field when in motion. The magnetic field generated by these particles, in conjunction with their interactions with external electromagnetic fields, give rise to the signals observed in MRI [7].

Protons are the predominant nuclei of interest in traditional clinical imaging. As a result, a key focus lies in understanding the behaviors and interactions of protons with external magnetic fields. Faraday's work demonstrated the concept of electromagnetic induction, revealing that a changing magnetic field can induce an electric current. He showed that a changing magnetic field induces current in a loop of wire when passing through it. The magnetic field that passes through the wire is defined as the magnetic flux, Φ. Faraday's law provides a comprehensive description of this phenomenon, highlighting the relationship between changing magnetic fields, magnetic flux, and induced currents in conducting loops [5].

$$\varepsilon = -N\frac{\Delta\Phi}{\Delta t} \tag{2.1}$$

Where N is the loops of wire, and $\Delta\Phi/\Delta t$ is the change of magnetic flux over time. We subsequently define the magnetic flux for a generic surface as follows:

$$\Phi_B = \int\int_{\mathrm{A}} \mathbf{B} \cdot d\mathbf{A} \tag{2.2}$$

When protons move through a loop of wire, their spin induces a small but detectable current. In the context of MRI, we measure the collective behavior of protons present in the human body. With billions of protons available, the potential for generating electromagnetic forces (emfs) is significant. However, in their natural state, these protons exhibit random orientations. The cumulative effect of the randomly oriented proton populations leads to signal cancellation, resulting in an absence of a measurable signal. The next intrinsic property of interest, spin, enables us to polarize, manipulate, and ultimately encode the proton's emf [5].

2.1.2 Spin

Spin is a quantized and intrinsic form of angular momentum that exists in all fermions. For protons, their spin is characterized by a value of $\pm 1/2$. In the framework of Quantum Mechanics, the state of spin and its interactions with external phenomena, such as radiofrequency waves, are described through probabilistic models and the Schrödinger equation. These quantum mechanical principles provide the most accurate representation of NMR phenomena and MRI experiments. However, classical mechanics offers a simpler explanation that quickly translates to experimental results. In this discussion, we will focus on the classical description of MRI. Spin is classically described as if the particle is truly ”spinning” around its axis (Fig. 2.1).

This classical description will be used due to its simplicity, but it's important to recognize that particles are not literally spinning [6], [8].

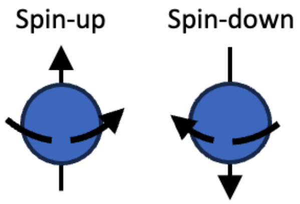

Fig. 2.1. In the classical description of proton spin states, a proton can exist in either a spin-up or spin-down state. In the spin-up state, the proton can be visualized as being aligned with the positive z-direction and exhibiting clockwise rotation. Conversely, the spin-down state corresponds to the opposite behavior, with the proton's angular momentum exhibiting counterclockwise rotation.

2.1.3 Interactions with a Strong Magnetic Field

Zeeman Splitting

In the presence of a strong magnetic field, protons orient themselves either parallel or anti-parallel to the magnetic field. Zeeman splitting describes the splitting of energy levels caused by an external magnetic field. For a spin 1/2 system, two spin states exist: ± 1/2. The spin-up state, characterized by parallel alignment, represents the lower energy state, whereas the spin-down state, characterized by anti-parallel alignment, represents the higher energy state. In MRI, a volume of spins is placed in an external magnetic field, denoted as B_0. This magnetic field produces a population-level event that aligns spins in either their up or down state [8].

As the spins polarize themselves into either their parallel or anti-parallel state, a population difference arises. The majority of spins occupy the lower energy state (spin up), resulting in a slim majority. This population difference gives rise to a net longitudinal vector aligned in the direction of the magnetic field (typically denoted as +z). This vector, known as the magnetization of the spins, represents the overall equilibrium state and encompasses both the spin up and down states [8]. The resulting net longitudinal equilibrium magnetization, M_0, is defined by equation 2.3.

$$M_0 = \frac{\rho_0 \gamma^2 \hbar^2}{4kT} B_0 \tag{2.3}$$

$\hbar$ represents the Planck constant; ρ_0 is the nuclear spin density; k stands for the Boltzmann constant; and T denotes temperature. The total equilibrium magnetization determines the net signal available for detection. To maximize the detectable signal, traditional MRI approaches have focused on enhancing the strength of the static magnetic field, B_0, by utilizing superconducting magnets [8].

Magnetic Moment and Precession

Spins have angular momentum that arises from their intrinsic spin-state. This angular momentum, in the presence of an external magnetic field, produces precession. The equilibrium magnetization, M_0, precesses about the B_0 field, as shown in Fig. 2.2. The precessional frequency of spins around the B_0 field is defined by the Larmor frequency [9], [10]:

$$\omega_0 = -\gamma B_0 \tag{2.4}$$

where γ is the nucleus-specific gyromagnetic ratio (which is 42.58 MHz/T for proton). The gyromagnetic ratio ultimately determines the precessional frequency at a specific magnetic field. Table 2.1 displays different gyromagnetic ratios.

Table 2.1: Gyromagnetic ratio and natural abundance of nuclear spins in the human body.

Atom	Gyromagnetic Ratio (MHz/T)	Abundance in Human Body
Hydrogen	42.58	88 M
Sodium	11.27	80 mM
Phosphorous	17.25	75 mM
Oxygen	-5.77	17 mM
Fluorine	40.08	4 µM

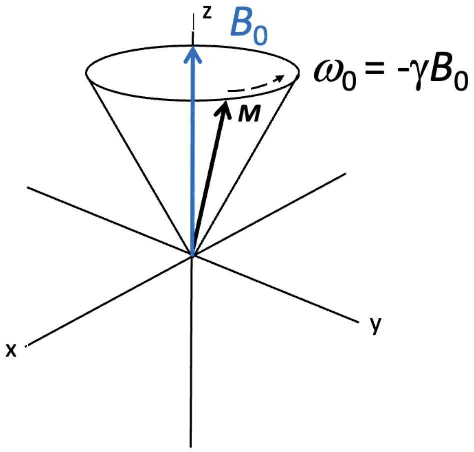

Fig. 2.2. When a spin is subjected to a strong magnetic field, it becomes polarized and assumes either a spin-up or spin-down state. In the depicted scenario, the spin is in the spin-up state. Once polarized, the angular momentum, which arises from its intrinsic spin-state, causes the spin to undergo precession around the direction of the magnetic field. The frequency of this precession, known as the Larmor frequency, is determined by the strength of the magnetic field and the gyromagnetic ratio of the spin (as shown in Equation 2.4). This precession forms the basis of MRI signals.

2.1.4 Polarized Spins Interaction with a B_1 field

RF Excitation

The magnetization signal can be described by its z-, y-, and x-components. The $M_z(t)$ and $M_{xy}(t)$ respectively describe the longitudinal and transverse components, where $M_{xy}(t)$ is a complex number defined: $M_{xy}(t) = M_x(t) + M_y(t)i$. MRI does not traditionally measure the longitudinal component but instead measures M_{xy}. To produce a detectable signal using the polarized spins, a transceiver is placed perpendicular to the direction of the B_0 field and transmits a radiofrequency (RF) field. The RF oscillating field has the same frequency as the spins (equal to the Larmor frequency). A resonance condition is met, leading to an energy transfer between the spins and the RF field, which tips the spins out of their equilibrium state [7], [11]–[13].

The RF field excites the spins by tipping them out of the z-axis. While the magnetization precesses, now in another plane, a detectable emf is measured by RF coils in the x- and y-axes. The Bloch equations describe the spins' behavior [14]:

$$\frac{dM_{x(t)}}{dt} = (\gamma \mathbf{M}(t) \times \mathbf{B}(t))_x - \frac{M_x(t)}{T_2} \tag{2.5}$$

$$\frac{dM_{y(t)}}{dt} = (\gamma \mathbf{M}(t) \times \mathbf{B}(t))_y - \frac{M_y(t)}{T_2} \tag{2.6}$$

$$\frac{dM_{z(t)}}{dt} = (\gamma \mathbf{M}(t) \times \mathbf{B}(t))_z - \frac{M_z(t) - M_0}{T_1} \tag{2.7}$$

B represents the magnetic field that the spins, **M**, are experiencing. Traditionally, **B** is composed of an RF component in the xy direction, denoted as B_1, and a z-component that constitutes the main magnetic field, B_0. T_1 and T_2 denote relaxation constants that bring the spins back to equilibrium.

T_1 and T_2^* Relaxation

When the spins are in a polarized state, they are said to be in equilibrium. When this equilibrium state is disturbed, such as by an RF excitation pulse, the spins undergo relaxation processes that return them to their equilibrium states. Two primary relaxation processes exist: a loss of signal coherence (T_2^* relaxation) and the return of the magnetization to its equilibrium state (T_1 relaxation). Different environments, such as different tissue types, exhibit distinct relaxation time constants [15], [16].

The longitudinal relaxation time constant, referred to as T_1, characterizes the relaxation of the excited magnetization's z-component. T_1 represents the time, in seconds, required for the magnetization to recover approximately 63 percent of its equilibrium value. T_1 relaxation is said to be the longer process due to the transfer of energy. When a spin-system is excited, the spins are placed out of equilibrium. Energy must flow back from its perturbed state into equilibrium. T_1 relaxation describes this process. T_1 relaxation describes the change in magnetic energy density back to its equilibrium state (parallel to the polarizing field) [17]. In other words, the rate at which spins return the energy received from an RF pulse back to its lattice structure (restoring equilibrium). The relaxation time constant, or spin-lattice relaxation, depends on the difference between M_0 and M_z as well as the energy transfer rates between the spins and surrounding lattice structure. T_1 widely varies in the human body and depends on different tissue types and properties. T_1 is typically on the order of seconds. T_2^* characterizes the observed relaxation and dephasing of the spins' transverse component and represents the time, in seconds, it takes for the spins' transverse signal to lose 63 percent of its peak signal value. T_2^* is composed of two components: $T_2^{'}$ and T_2, as described by the following equation:

$$1/T_2^* = 1/T_2^{'} + 1/T_2 \tag{2.8}$$

$T_2^{'}$ originates from variations in the spins' Larmor frequencies. A difference in Larmor frequencies leads to the spin population having various precession rates - losing coherence rapidly. These variations can arise from factors such as B_0 gradient coils (which will be discussed later) or inhomogeneities in the B_0 field. Unlike T_2, $T_2^{'}$ is reversible, meaning that the dephasing caused by these variations can be undone with pulse sequences. T_2 is irreversible and stems from local, random, time-dependent field variations resulting from spin-spin interactions within the spins themselves and their surrounding environment [16]. Spins, in addition to responding to magnetic fields, produce their own magnetic fields. These tiny magnetic fields interact with each other and their own electron orbitals through what is known as hyperfine interactions. These interactions lead to a rapid loss of coherence (i.e., dephasing). Figure 2.3 illustrates the decay of the magnetization signal, as described by the Bloch equations [17]. T_2^* is typically on the order of milliseconds and like T_1 is highly dependent on tissue types and properties.

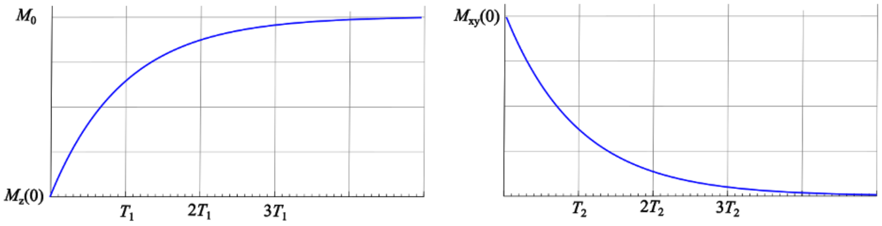

Fig. 2.3. This figure illustrates the relaxation process of the longitudinal (M_z) and transverse components (M_{xy}) of the spins, assuming that they have been tipped into the transverse plane.

T_1 and T_2 are crucial time constants in clinical imaging and vary across different tissue types. Advanced pulse sequence designs leverage specific T_1 and T_2 values to produce images with different contrasts. Subsequently, MRI images can be tailored to enhance or suppress the signal intensity of specific tissue types based on their T_1 and T_2 values. For example, FLAIR (Fluid-Attenuated Inversion Recovery) images take advantage of the T_1 values of fluid (typically in the brain) to minimize the signal from fluid, thus highlighting other structures of interest. By manipulating pulse sequences and optimizing imaging parameters based on T_1 and T_2 values, radiologists can customize image contrast to facilitate better tissue characterization and diagnostic information. Table 2.2 shows an example of different T_1 and T_2 values of different tissues, while Figure 2.4 demonstrates various contrast-based images.

Table 2.2: Different T_1 and T_2 values for different tissue types

Tissue	T_1 (ms)	T_2 (ms)
Grey Matter	950	100
White Matter	600	80
Muscle	900	50
Cerebrospinal Fluid	4500	2200
Fat	250	60

The First Rotating Frame

Although the Bloch equations capture the behavior of spins in the presence of a main magnetic field and an RF pulse, MR signals are traditionally described in the first rotating frame. In this first rotating frame, rather than **M** precessing at the Larmor frequency about a B_0 field, **M** is stationary. The Bloch equations are expanded on to arrive at the first rotating frame. γB_1 is a field applied in the xy plane and γB_0 is the main magnetic field in the z direction.

$$\frac{dM_x}{dt} = M_y \gamma B_0 - M_z \gamma B_1 \sin(\omega_0 t) - \frac{M_x}{T_2} \tag{2.9}$$

$$\frac{dM_y}{dt} = M_z \gamma B_1 \cos(\omega_0 t) - M_x \gamma B_0 - \frac{M_y}{T_2} \tag{2.10}$$

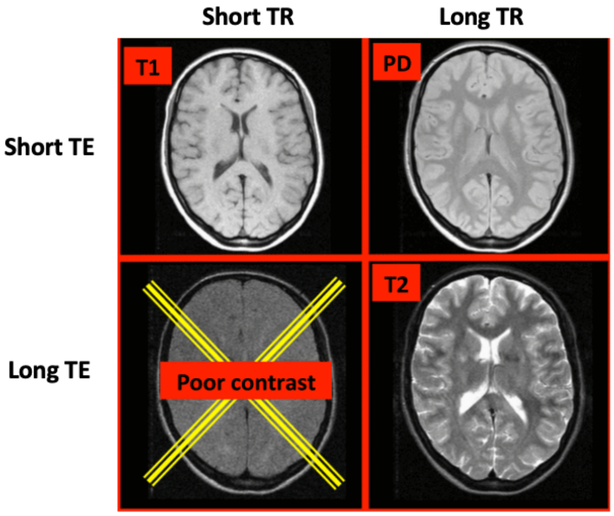

Fig. 2.4. Brain MRI images are shown, each acquired using different pulse sequences that yield different contrast types. These contrast variations serve to enhance or suppress the signal intensities of specific tissue types. The timing parameters of the pulse sequences are determined based on the T_1 and T_2 values of the tissues being imaged (Courtsey of Allen D. Elster, MRIquestions.com).

$$\frac{dM_z}{dt} = M_x\gamma B_1 \sin(\omega_0 t) - M_y\gamma B_1 \cos(\omega_0 t) - \frac{(M_z - M_0)}{T_1} \tag{2.11}$$

A simple proof demonstrates how to define the first rotating frame. We define a novel frequency, known as ω_{eff}, which is defined as $\omega_{\text{eff}} = \omega_0 - \omega_c$ in place of ω_0 and γB_0 is replaced with Ω, which represents resonance offset.

$$\frac{dM_x}{dt} = M_y\Omega - M_z\gamma B_1 \sin(\omega_{\text{eff}} t) - \frac{M_x}{T_2} \tag{2.12}$$

$$\frac{dM_y}{dt} = M_z\gamma B_1 \cos(\omega_{\text{eff}} t) - M_x\Omega - \frac{M_y}{T_2} \tag{2.13}$$

$$\frac{dM_z}{dt} = M_x\gamma B_1 \sin(\omega_{\text{eff}} t) - M_y\gamma B_1 \cos(\omega_{\text{eff}} t) - \frac{(M_z - M_0)}{T_1} \tag{2.14}$$

In the first rotating frame, $\omega_c = \omega_0$ making $\omega_{\text{eff}} = 0$ and the Bloch equations:

$$\frac{dM_x}{dt} = M_y\Omega - \frac{M_x}{T_2} \tag{2.15}$$

$$\frac{dM_y}{dt} = M_z\gamma B_1 - M_x\Omega - \frac{M_y}{T_2} \tag{2.16}$$

$$\frac{dM_z}{dt} = -M_y\gamma B_1 - \frac{(M_z - M_0)}{T_1} \tag{2.17}$$

The above equations demonstrate the magnetization in the first rotating frame. In the first rotating frame, the B_1 field is a constant field vector, rather than an oscillating field. The first rotating frame of reference is routinely used due to its simplicity in conceptualizing the effects of various RF fields. The equations further simplify if we study the case of no resonance offset ($\Omega = 0$).

$$\frac{dM_x}{dt} = -\frac{M_x}{T_2} \tag{2.18}$$

$$\frac{dM_y}{dt} = M_z\gamma B_1 - \frac{M_y}{T_2} \tag{2.19}$$

$$\frac{dM_z}{dt} = -M_y\gamma B_1 - \frac{(M_z - M_0)}{T_1} \tag{2.20}$$

The first rotating frame Bloch equations can be used to investigate resonance offset effects and RF pulse performance. A variety of pulse sequences are routinely evaluated using the Bloch equations.

The FID Experiment

In MRI's first experiment [18], spins, such as protons from water molecules, are placed in a static magnetic field (B_0), which polarizes the spins in the +z direction. A constant amplitude pulse with a carrier frequency matching the Larmor frequency of the spins is transmitted from an RF coil oriented perpendicular to B_0 in the +x direction. This waveform meets the resonance condition and transfers energy to the spin population.

The RF field "tips" the spins out of their aligned state along the z-axis and into the xy plane. As a result, the spins now reside in the xy plane and are oriented towards the y-axis. RF pulses are calibrated to produce various angles of rotations; traditionally, RF pulses are optimized to rotate the magnetization vector 90-degrees to the transverse plane. By changing the characteristics of the RF pulses (e.g., power,

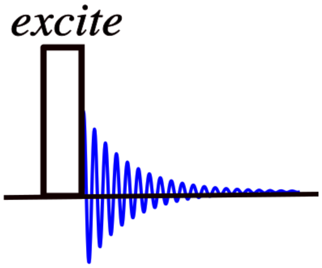

Fig. 2.5. The spins initially start polarized in the +z direction. To manipulate the spins, an RF pulse is applied at the Larmor frequency. In the figure above, an RF square pulse is depicted in the first rotating frame. As a result of this pulse, the spins tip into the transverse plane and precess. The precession produces a measurable signal (depicted in blue). The exponentially decaying signal is known as Free Induction Decay (FID).

length, or waveform), a wide range of flip angles and effects can be achieved.

Once in the transverse plane, the spins undergo dephasing and relaxation based on their T_1 and T_2 time constants. Placing a transceiver or receiver along the y-direction, a decaying signal is measured, known as Free Induction Decay (FID). The transverse signal in the FID sequence exhibits an exponential decay. Figure 2.5 provides an illustration of the signal and pulse sequence [15].

The Spin-Echo Experiment

In the absence of T_1 and T_2 effects, the decay of the Free Induction Decay (FID) signal arises from spins experiencing different resonance frequencies, which is described by $T_2^{'}$ [19]. This discrepancy in resonance frequencies typically arises from imperfections in the main magnetic field, known as B_0 inhomogeneity, or other local fluctuations. When spins located at different positions encounter varying B_0 field values, rapid dephasing occurs due to the differences in resonance frequencies [15].

To counteract the effects of B_0 inhomogeneity, a spin-echo experiment is employed to refocus the spins and generate a recoverable signal. This pulse sequence, as illustrated in Figure 2.6, involves the application of additional RF pulses to rephase the spins and produce an echo signal. The spin-echo sequence compensates for the dephasing caused by B_0 inhomogeneity, resulting in a coherent and detectable signal.

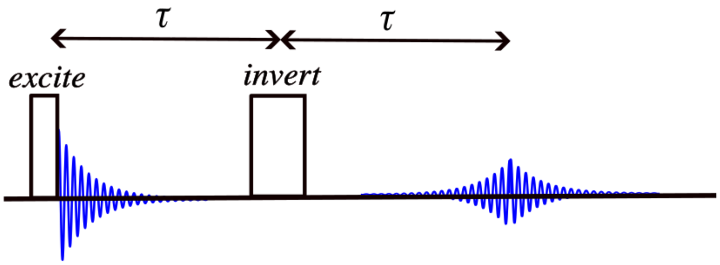

Fig. 2.6. The spin-echo pulse sequence begins by tilting the polarized spins from the +z axis into the transverse plane. As time progresses, the spins experience dephasing due to local inhomogeneities in the magnetic field, but they have not completely relaxed back to the +z axis. A second pulse, twice the duration of the first, is applied, resulting in a 180-degree planar rotation. This reversal of precessional frequencies causes the dephased spins to refocus, realign, and then dephase again, resulting in the formation of an echo.

We now describe the pulse sequence in detail. First, an excitation pulse tips the spins into the transverse plane. Then, after a certain period of time (defined as τ), a second pulse with a larger amplitude inverts the plane. This plane inversion reverses the direction of the spins' precession, causing spin refocusing τ after the second pulse. Figure 2.6 shows the pulse sequence and provides an example. Classically, the initial excitation pulse is calibrated to produce a 90-degree plane rotation, while the inversion pulse produces a 180-degree plane rotation. A spin-echo effectively recovers the signal lost to $T_2^{'}$, but not T_2 [15].

The acquisition of an echo not only captures the initial FID signal but the whole complex signal. This provides the advantage of acquiring additional data and, more importantly, supplying the necessary information for a complex Fourier transformation (FT), which is commonly employed for data reconstruction. By measuring an echo, a complex FT can accurately categorize negative and positive frequencies. As will be described, the complex FT plays a vital role in reconstructing the data and extracting meaningful information from the acquired signals.

2.2 Radiofrequency Pulses

Radiofrequency (RF) pulses are the primary mechanism of signal creation in MRI. There are two main categories of RF pulses: amplitude-modulated and frequency-modulated pulses.

2.2.1 Spin Tipping with Amplitude-Modulated Pulses

Amplitude-modulated (AM) pulses, such as the sinc pulse, are commonly used in MRI to rotate spins into the transverse plane for data acquisition. They purely modulate the amplitude of the transmission waveform and transmit the wave at a constant carrier frequency, ω_c (typically set to the Larmor Frequency). In the laboratory frame, a sinc pulse is defined as

$$AM(t) = sinc(t)cos(\omega_0) \tag{2.21}$$

while in the the rotating frame, they are defined as:

$$AM(t) = sinc(t) \tag{2.22}$$

Figure 2.7 shows a sinc pulse in the lab and first rotating frame [20].

Throughout this section, pulses will be plotted and discussed in the first rotating frame. For a square pulse, the flip angle of excitation is defined by:

$$\theta = -\gamma B_1 T_p \tag{2.23}$$

where B_1 is the RF field in Tesla and T_p is the pulse length in seconds. Prior to experiments, pulses are typically calibrated to produce the maximum flip-angle.

The AM pulse is transmitted at the Larmor frequency of interest. As a result, in the presence of B_0 inhomogeneity, spins with different precessional frequencies may experience varying flip angles. Spins that are off-resonant are tipped by a B_{eff} instead of a B_1, where:

$$\mathbf{B}_{\text{eff}} = (-\Omega/\gamma)\hat{\mathbf{z}} + B_1\hat{\mathbf{x}} \tag{2.24}$$

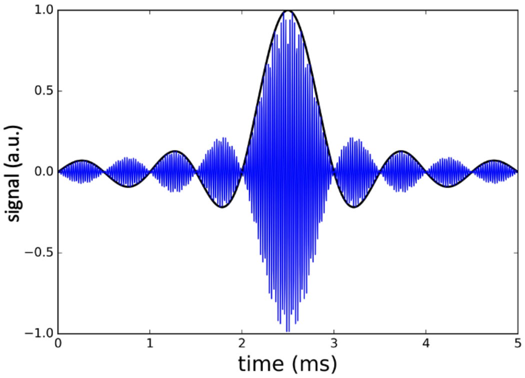

Fig. 2.7. A widely utilized amplitude modulation function in MRI is the sinc pulse. The sinc pulse is showed with its carrier frequency and without it. The blue line represents the RF waveform that emits from the waveform generator. The pulse is transmitted for spins at a field strength of 0.5T. The black line depicts the demodulated signal, also known as the RF waveform signal in the first rotating frame.

$\Omega = \omega_0 - \omega_{\text{RF}}$ defines resonance offset present from the B_0 magnet or RF pulse. We can approximate the effect of off-resonance on the pulse's performance by examining the Fourier transformation of the pulse. This approximation, known as the small-tip angle approximation [21], closely aligns with numerical Bloch simulations.

Traditional MRI heavily relies on AM pulses, calibrated to produce a variety of flip angles in different pulse sequences. However, in most cases, variations in B_1 or B_0 can lead to changes in flip angles, which can ultimately degrade the image. MRI pulse sequences typically demand highly uniform B_1 and B_0 fields to minimize these variations. Volumetric coil designs are generally successful in producing highly uniform B_1 fields, while a large superconducting magnet is often effective in generating uniform B_0 fields. An alternative approach that addresses the challenges posed by B_1 and B_0 inhomogeneities is the use of adiabatic pulses. Adiabatic pulses offer a robust method for achieving uniform inversions and excitations in the presence of both B_1 and B_0 field inhomogeneities.

2.2.2 Spin Tipping with Adiabatic Pulses

Frequency-modulated Pulses

Frequency-modulated (FM) pulses are distinct from amplitude-modulated (AM) pulses as they simultaneously modulate both the pulse amplitude and carrier frequency. FM pulses are characterized by two modulation functions: an amplitude modulation function ($\omega_1(t)$) and a frequency modulation function ($\Delta\omega(t)$). A general FM(t) modulation function is defined as follows [22], [23]:

$$\Delta\omega(t) = \omega_c - \omega_{RF}(t) \tag{2.25}$$

In the FM function, the pulse transmit frequency, denoted as $\omega_{RF}(t)$, varies over time about a center frequency (ω_c), usually set to the Larmor frequency of interest. Figure 2.8 illustrates an example of a Hyperbolic Secant (HS) pulse, along with its associated AM and FM functions. HS pulses are widely favored in MRI due to their favorable performance in the presence of B_0 and B_1 inhomogeneities [24].

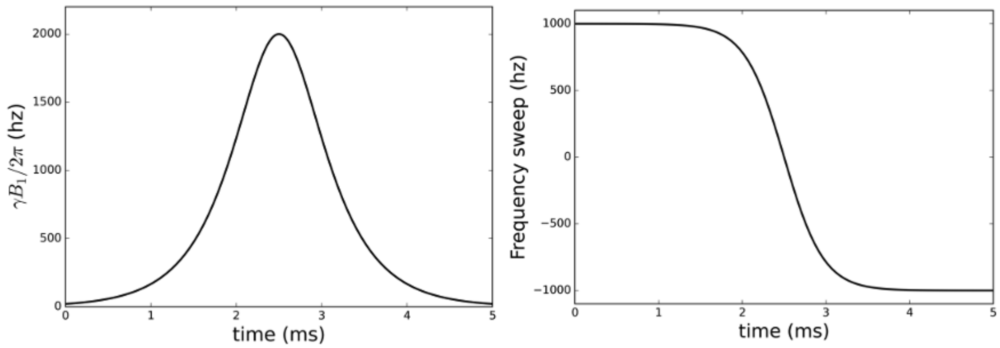

Fig. 2.8. The figure on the left depicts the amplitude modulation function of an HS (Hyperbolic Secant) pulse, while the figure on the right represents the frequency modulation function of the same HS pulse. HS pulses have the ability to uniformly invert spins even in the presence of B_1 and B_0 inhomogeneities, provided that the pulses satisfy the adiabatic condition. Specifically, the pulse is resistant to B_0 off-resonance effects within the bandwidth (in this case, ±1kHz) of the frequency modulation pulse.

One unique feature of frequency-modulated (FM) pulses is the ability to independently define the bandwidth and pulse length. FM pulses are defined by their time-bandwidth product or R-value: $R = T_p \cdot BW$, where BW represents the range of frequencies the FM pulse sweeps, and T_p is the pulse length. In practice, FM pulses are transmitted with an AM(t) and a phase modulation function ($\phi(t)$), rather than an FM(t). The application of PM functions are equivalent to FM functions and are defined as:

$$\phi(t) = \int_0^t \Delta\omega(\tau) d\tau \tag{2.26}$$

Where τ is a dummy integration variable. Spin tipping with PM and FM pulses results in different magnetization trajectories [25], but their net effects result in an inversion of spins and are thus equivalent.

The Adiabatic Condition and Adiabatic Inversions

FM pulses are routinely utilized above the adiabatic condition. If the adiabatic condition is met, spins that begin collinear or perpendicular to ω_{eff} remain approximately so throughout the pulse. The adiabatic condition is:

$$|\omega_{\text{eff}}(t)| >> |d\alpha/dt| \tag{2.27}$$

where $\omega_{\text{eff}} = -\gamma B_{\text{eff}}(t)$, $\omega_1 = -\gamma B_1$,

$$\omega_{\text{eff}}(t) = \omega_1(t)\hat{x'} + (\omega_{\text{RF}}(t) - \omega_{\text{c}})\,\hat{z'},$$

and $\alpha(t)$ describes the angular velocity of ω_{eff} , otherwise defined as:

$$\alpha(t) = \arctan\left(\frac{\omega_1(t)}{\Delta\omega(t)}\right). \tag{2.28}$$

This is where the major benefit of adiabatic FM pulses lies: they uniformly invert across B_0 and B_1 variations within the BW of the FM(t), and for B_1 values past the adiabatic condition (Fig. 2.9). As a result, adiabatic pulses are routinely used as inversion pulses in imperfect magnets [22], [23].

The application of an FM pulse introduces a Ω-dependent quadratic phase [26]. Thus, although AFPs produce uniform inversions in highly imperfect magnets, the quadratic phase must be removed. To correct this, a second, equivalent pulse can

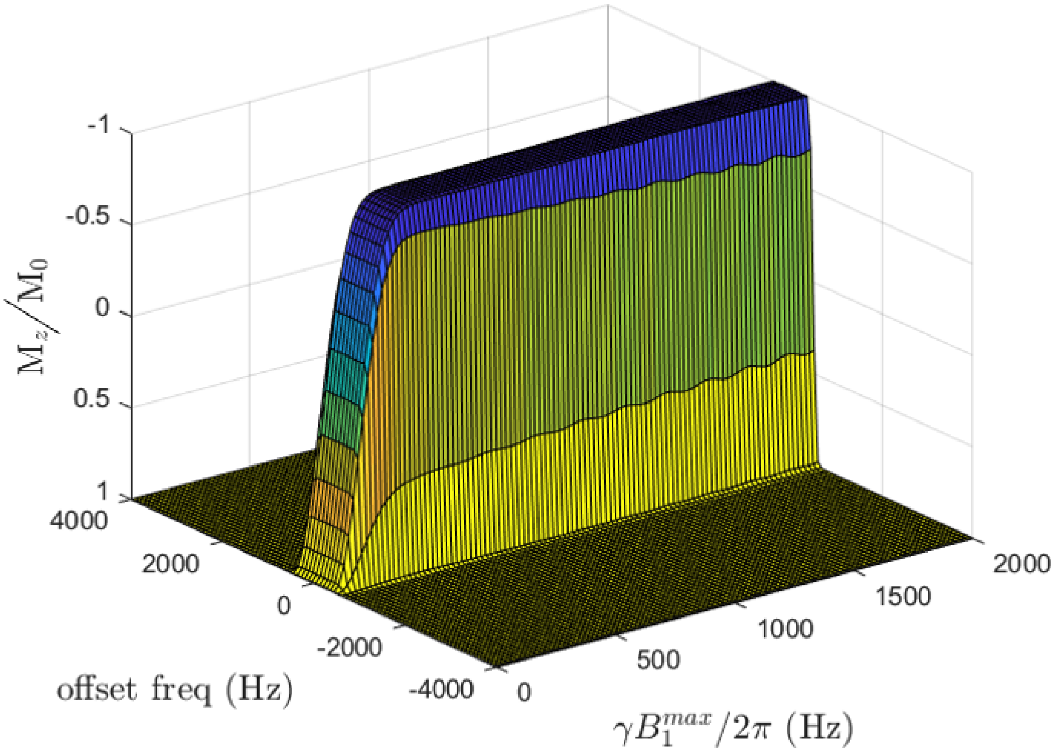

Fig. 2.9. The presented simulation illustrates the inversion profile of an adiabatic HS (Hyperbolic Secant) pulse. The inversion profile is depicted across B_1 and B_0 inhomogeneities. The profile demonstrates that beyond the adiabatic threshold (greater than 250 Hz), the inversion becomes uniform across different B_1 and B_0 values. The pulse length and bandwidth was 24 ms and 1 kHz respectively.

be sequentially applied to unwind the quadratic phase and restore signal coherence. Despite their advantages, adiabatic pulses do have some drawbacks. They typically require higher power to ensure adherence to the adiabatic condition and are generally longer than their AM counterparts.

Propagator Analysis

The final rotation angle, and any resulting phase, produced by an FM pulse was traditionally numerically calculated. Although accurate, once a volume of interest is under investigation, calculations can be cumbersome and slow. A propagator analysis enables the analytical determination of an arbitrary set of spins phase and behavior throughout the FM pulse in the presence of any B_1 and B_0 field. A propagator analysis simply applies an analytical rotation to a set of spins using a 3x3 rotation matrix. The propagator matrix for an arbitrary adiabatic full passage [22]:

$$U = exp(i\phi_0 I_z)exp(i\Delta\alpha I_y)exp(-i\phi_0 I_z)exp(i\psi I_z) \tag{2.29}$$

Or expressed in matrix form:

$$\begin{gathered} UI_{\mathrm{x}}U^{-1} = I_{\mathrm{x}}\left(\cos\left(\psi-\phi_0\right)\cos\Delta\alpha\cos\phi_0 - \sin\left(\psi-\phi_0\right)\sin\phi_0\right) \\ +I_y\left(\sin\left(\psi-\phi_0\right)\cos\phi_0 + \cos\left(\psi-\phi_0\right)\cos\Delta\alpha\sin\phi_0\right) + I_z\left(\cos\left(\psi-\phi_0\right)\sin\Delta\alpha\right) \end{gathered} \tag{2.30}$$

$$\begin{gathered} UI_yU^{-1} = I_x\left(-\sin\left(\psi-\phi_0\right)\cos\Delta\alpha\cos\phi_0 - \cos\left(\psi-\phi_0\right)\sin\phi_0\right) \\ +I_y\left(\cos\left(\psi-\phi_0\right)\cos\phi_0 + \sin\left(\psi-\phi_0\right)\cos\Delta\alpha\sin\phi_0\right) + I_z\left(\sin\left(\psi-\phi_0\right)\sin\Delta\alpha\right) \end{gathered} \tag{2.31}$$

$$UI_{\mathrm{z}}U^{-1} = I_{\mathrm{x}}\left(\cos\phi_0\sin\Delta\alpha\right) + I_{\mathrm{y}}\left(\sin\phi_0\sin\Delta\alpha\right) + I_{\mathrm{z}}(\cos\Delta\alpha). \tag{2.32}$$

Where I_x, I_x and I_z describe the x-, y-, and z- components of an isolated spin defined as I. $\Delta\alpha$ is the rotation angle at a specific time point defined by Eq. 2.28 and ϕ_0 is the initial phase of the pulse. ψ is the accumulated evolution angle about ω_{eff} during the pulse length, T_p:

$$\psi(T_p/2) = \int_0^{T_p/2} \omega_{eff}(t)dt \tag{2.33}$$

Although fast and accurate in predicting spins' behaviour in a pulse sequence, a propagator analysis assumes complete adiabaticity, which can experimentally vary especially in instances with weak B_1 fields.

2.3 Relaxometry

2.3.1 T_1 and Inversion Recovery

T_1 values are a function of tissue properties and field dependencies, yet are crucial in clinical imaging. T_1 values thus necessitate empirical determination. Inversion recovery, a fundamental MRI pulse sequence, quantifies T_1 relaxation using a simple inversion pulse. The inversion recovery experiment is depicted in Figure 2.10 [15], [16].

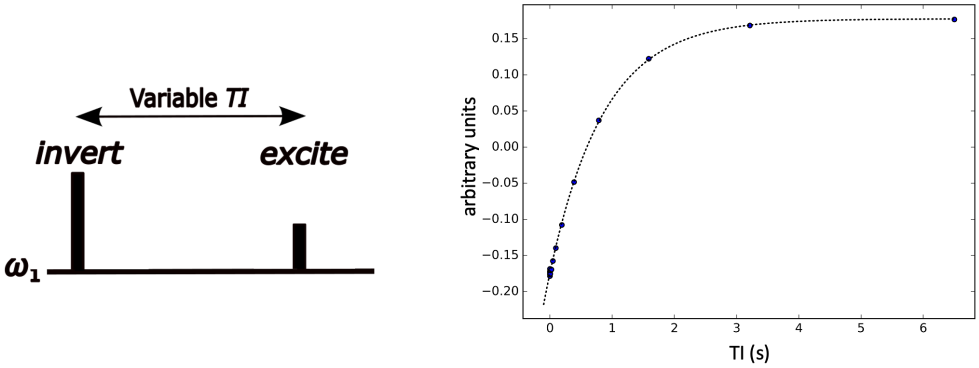

Fig. 2.10. A demonstration of the pulse sequence and its measured effects is presented. Panel A illustrates the pulse sequence with a set delay defined as t. To measure T_1, t is varied. Panel B shows the signal (depicted as an echo) across different t values. The signal of the echo is proportional to the available M_z, allowing for a numerical fitting that ultimately determines T_1.

The initial inversion pulse alters the available magnetization to generate an FID signal. By varying the time interval between the inversion pulse and the subsequent excitation, it becomes possible to plot the data and determine T_1 by fitting the following equation:

$$S_{R_1}(t) = \alpha - \beta \cdot e^{-R_1 \cdot t} \quad . \tag{2.34}$$

Equation 2.34 will be covered in the following chapter. Various advanced inversion recovery sequences are available, such as the T_1 inversion recovery spin-echo. In this sequence, after the 90-degree excitation shown in Figure 2.10, an inversion pulse is applied to refocus the spins into an echo. A notable feature of T_1 inversion recovery approaches is their ability to measure signals at negative, null, and positive values. The optimal IR pulse parameters to determine T_1 have been widely explored [16].

The main drawback of the spin-echo and FID inversion recovery methods is their time-consuming nature. A range of pulse sequences and signal processing techniques have been developed to capture T_1 information more efficiently.

2.3.2 T_1 and Saturated Recovery

Inversion recovery sequences demand nearly complete relaxation of the magnetization before acquiring another point on the T_1 curve [27], resulting in reduced speed of the pulse sequence. In contrast, saturated recovery (SR) sequences enable rapid acquisition of T_1-dependent signals [15], [16].

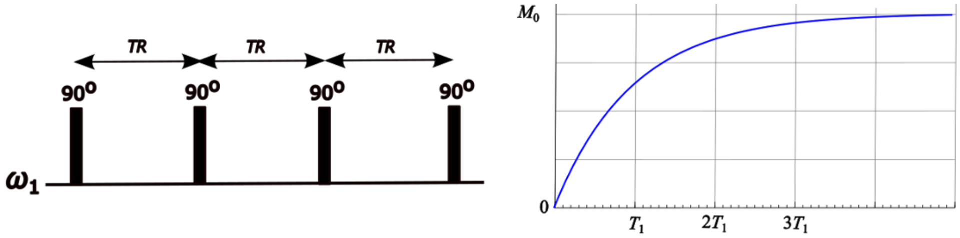

Fig. 2.11. A demonstration of the saturated recovery pulse sequence. A train of 90-degree RF pulses tip the spins. A short repetition time (TR) is placed between the pulses. The resulting FID can be fit in a T_1 curve. Although notably, the T_1 lacks the full dynamic range of an inversion recovery experiment.

SR pulse sequences utilize a series of 90-degree pulses and measure the resulting FID. The acquired data can be fitted to equation 2.34. However, saturated recovery approaches suffer from a reduced dynamic range, which affects their accuracy in measuring T_1. Unlike IR approaches, SR cannot measure negative magnetization values, thus diminishing their overall precision. While saturated recovery can measure the null point to $+M_0$, an inversion recovery experiment can measure a range from -M_0 to $+M_0$.

Chapter 3

The development of a 0.5 T NMR system to perform relaxometery on TEG devices

3.1 Introduction

Macroencapsulation devices, known as tissue engineered grafts (TEGs), are therapeutic devices that enable the implantation and immunoprotection of therapeutic cells [28], [29] without the need for lifelong systemic immunosuppression. TEGs show great potential for treating a variety of diseases, including diabetes. Pancreatic islet transplantation [30], [31] inside a TEG offers promise as a functional cure for type 1 diabetes [32]. The TEG's immunoprotective membrane makes it possible to safely use human islets or human derived stem cells, which are more readily available.

These "bioartificial pancreata" are intended to be implanted subcutaneously. To ensure therapeutic islet cell viability and function after implantation, TEGs must provide adequate oxygenation to the cells within them [33]–[35]. Inadequate oxygenation can compromise cell viability, function, and the overall efficacy of the treatment [36]. Delivery of supplemental oxygen (DSO) maintains the TEG's ambient oxygenation within healthy levels [37] and enables cells encapsulated within the TEGs to remain viable and functional over long periods of time [38]. An *in vivo* method of measuring average partial pressure of oxygen (pO_2) [39] levels within the TEG in humans would greatly enhance our understanding of the need and the efficacy of oxygen delivery to the cells within TEGs.

The measurement of pO_2 levels *in vivo* provides two critical insights: 1) determination of the required levels of DSO, and 2) knowledge of events that alter oxygenation, such as cell proliferation, death, inflammation, and vascularization. The gold standard for *in vivo* oxygenation measurement is Eppendorf needle probes; however, these require multiple invasive procedures to measure the average oxygenation of an entire volume [40] and have a limited depth for measurements [41]. The invasive nature of this procedure places a significant burden on the patient and compromises the integrity of the TEG.

NMR does not have these shortcomings and offers the more feasible solution. An NMR oxygen probe can be implanted alongside pancreatic islet cells to enable non-invasive in-vivo measurements of pO_2 through the probe's affect on spin relaxation. In this study, the fluorinebased oxygen probe perfluoro-15-crown-5-ether (PFCE) was selected [42], [43]. The spin-lattice relaxation rate constant ($R_1 = 1/T_1$) of PFCE is dependent on the neighboring temperature and pO_2 levels, while being independent of gas solubility [44]. This work explores the feasibility of measuring R_1 at a low field (0.5 T), as a step towards future clinical use in guiding DSO in TEGs.

In a previous study [44], the pO_2 and temperature dependencies of the PFCE's R_1 were obtained empirically at 16.4 T. Although the work showed the feasibility of measuring pO_2 in TEGs *in vivo*, 16.4 T MRI systems are not widely produced and are thus not easily accessible. 16.4 T systems cannot meet the accessibility needs of the current large number of diabetic patients [3].

To address these challenges, we developed a novel, compact, and affordable [45] NMR relaxometer for measuring oxygen in implanted TEGs. To demonstrate feasibility, we performed a validation study that measured the oxygen- and temperature-dependent R_1 values of PFCE within a TEG.

Magnet specifications	Metric
Length	40 cm
Bore diameter	19 cm
Mass	150 kg
Field strength	0.5 T
Configuration	4 – ring Halbach

Table 3.1: Description of the magnet

3.2 Methods:

3.2.1 The NMR System:

^{19}F spectra were acquired with a custom NMR system interfaced to the 0.5 T Halbach magnet (Fig 3.1, Table 3.1). The custom magnet assembly was designed and built by The RE Magnet Studio Ltd. following the design approach of Spherical Harmonic Decomposition previously described [45].

The calculated magnetic fields [46] of the 0.5 T Halbach array showed the 5 - gauss line to be approximately 0.5 meters from the front of the magnet. The magnet's design caused a rapid field drop off immediately out of isocenter (Fig. 3.2). No passive, nor active shimming was performed on the magnet, leading to broad resonance linewidths.

A heat regulator system (designed and manufactured by The RE Magnet Studio Ltd.) minimized magnet temperature variation and thus field drift. To achieve this, flexible resistive heating elements were attached to the magnet and connected to a proportional-integral-derivative (PID) control system. A Pt-100 temperature sensor measures and inputs the magnet's temperature to a control system that increases (or decreases) the power delivered to the heating elements until the desired temperature (set by the regulator's control interface) is reached within ± 0.01 degrees.

The following grounding configuration provided the least noise. The spectrometer, computer, and RF power amplifier utilized a true earth ground, while the active T/R switch and magnet utilized a floating ground. The system lacks a Faraday cage; thus, to minimize electromagnetic interference, a laser cut acrylic panel was fabricated to fit the back of the magnet's bore. The panel has copper glued to the bore-facing

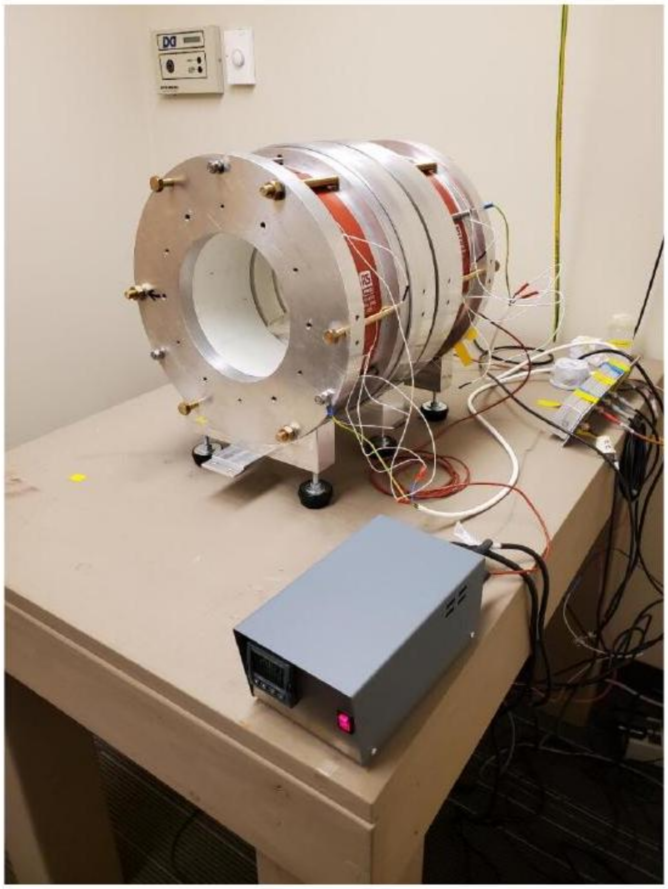

Fig. 3.1. The 0.5 T Halbach magnet used in experiments. To minimize resonance drift, a heat regulator system (grey box) controls the temperature of the magnet via flexible heaters (red).

side, while the other side is not covered. The copper element serves as the grounding element. The grounding panel has a BNC adapter connection that enables RF coils to be placed inside the magnet. The RF coil was connected to the preamplifier through the grounding panel. A custom-built solenoidal coil (4 turns, diameter = 5 cm) was used as the RF transceiver.

Data were acquired with a custom-built two-channel transmit and receive CIER-Mag Digital Magnetic Resonance Spectrometer (DMRS) (source: University of São Paulo) [47]. Each transmit channel can perform amplitude modulation in a four-quadrants approach (amplitude dynamics of 16 bits), along with frequency modu-

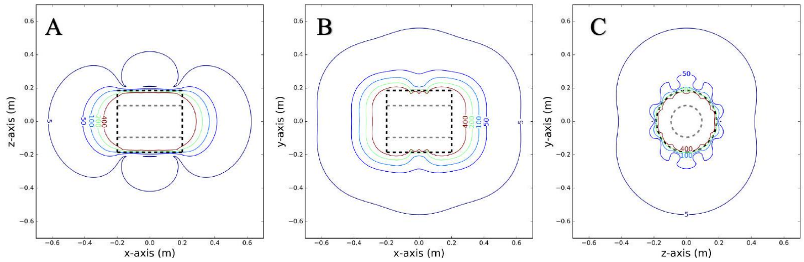

Fig. 3.2. The 0.5 T Halbach magnet field lines in Gauss. The magnet's outer dimensions are shown in black dashed lines, while the magnets inner dimensions are shown in grey dashed lines. The Gauss lines are shown in the following planes: A) $xz(y = 0)$, B) $xy(z = 0)$, and C) $yz(x = 0)$.

lation (24 bits -0.373 Hz resolution over $+/-3.125$ MHz modulation bandwidth) and phase modulation (14 bits $-0.088°$ resolution). The DMRS software was structured by the Python Magnetic Resonance Framework [47], and the system provides an integrated development environment (IDE) to help on the design of NMR Methods using high level programming capabilities. Pulse sequences are written using a custom coding language (F-language) [48], [49], which allows access to all features of the DMRS synthesized hardware. Supporting RF hardware included a CPC 500 W amplifier (model: 9T500M-16C), and a Varian T/R switch and preamplifier (model: 0191432205).

3.2.2 RF pulses and pulse sequence:

The 0.5 T magnet is not shimmed, and thus, ^{19}F spectral linewidths are broad, typically $\sim$ 10kHz in a 5 cm sphere. To properly measure R_1 from the TEGs within such an inhomogeneous field, broadband pulses are required. For this reason, two broadband pulse types were chosen: a short square pulse for excitation and a flattened adiabatic hyperbolic secant pulse ($n = 5$) [24] for refocusing in a double spin-echo sequence.

The square pulse was 50 μs in length, while the adiabatic HS pulse had a time-bandwidth product of $60(= 12,000 \text{ Hz} \cdot 0.005 \text{ s})$. The RF power was set to produce a peak surface γB_1 of 5 kHz for all pulses. A custom Python-based Bloch simulator was used to investigate the achievable excitation and inversion bandwidths with the RF power available. The pulses were simulated across a broad range of resonance offsets (±8 kHz) with a peak γB_1 of 5 kHz. Figure 3.3 shows the excitation and inversion pulses had sufficient bandwidths to overcome the broad ^{19}F linewidth.

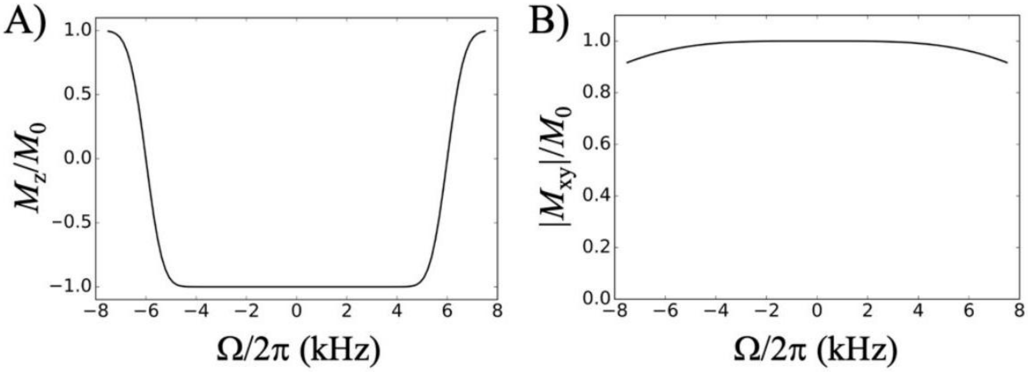

Fig. 3.3. Bloch simulations showing the broad spectral bandwidth of the RF pulses used in this study. A) Inversion profile of the flattened hyperbolic secant pulse, HS5 (time-bandwidth product = 60), showing a highly uniform 180° flip over a bandwidth of $\sim$ 10 kHz. B) Excitation profile of a 50 μs square pulse, showing relatively uniform excitation over a similar bandwidth. In both experiments and simulations, γB_1 was 5 kHz. These simulations demonstrate the efficacy of broadband pulses to excite and refocus magnetization, despite the inhomogeneous B_0 of the 0.5 T magnet.

An adiabatic inversion-recovery double spin-echo sequence (Fig. 3.4) was used to measure the R_1 of TEGs. For all experiments, the receiver bandwidth was 40 kHz, $TE = 18$ ms, and echoes were sampled using 128 data points. TI was logarithmically incremented between 10 μs and 6.5 s [50]–[53] in 20 steps. TR was 7 s, and 3 echoes were averaged per TI value (total scan time = 7 min). Additional experiments were performed using only 1 or 2 averages (scan times of 4.66 and 2.33 min, respectively) to test experimental variation.

3.2.3 R_1 fitting:

The resulting data were manually phased to remove any DC phase component. Following phasing, apodization of the time-domain data was performed using a Gaussian curve (defined by SciPy, Python v3.9). Apodization with an approximately matched windowing function minimized line broadening and drastically reduced the

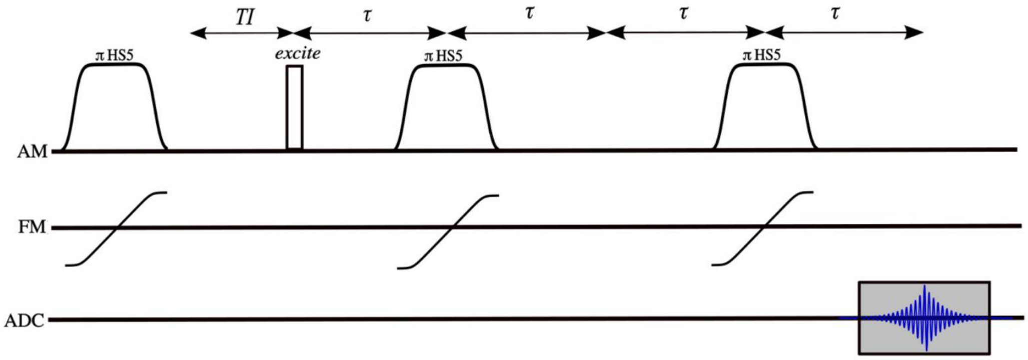

Fig. 3.4. The broadband double spin-echo sequence used for all experiments. To measure R_1, an adiabatic full passage precedes a variable inversion time (TI), followed by a square excitation pulse and two adiabatic full passages separated by proper delays to form a double spin echo. All adiabatic pulses were flattened hyperbolic secants ($n = 5$) with time-bandwidth product of 60. A 50μs square pulse was used for excitation. The application of two FM pulses after spin excitation removes all residual B_0 - and B_1-dependent phase and completely refocuses spins across a broad bandwidth. To measure R_1, TI was logarithmically stepped. The adiabatic pulse sequence allowed accurate R_1 estimation, despite broad ^{19}F linewidth.

impact of noise on the data. The Gaussian curve was defined by a modified normal distribution curve ($\mu = 0, \sigma = 0.05$) that had a vector length equal to the time-domain signal. To extract R_1, the integral of the real component (after apodization and phasing) for each TI value was computed, and their values were fit across TI values with the three-parameter equation,

$$S_{R_1}(t) = \alpha - \beta \cdot e^{-R_1 \cdot t} \quad , \tag{3.1}$$

using the SciPy optimize package. α and β were used as scaling factors that fit the experimental data. They described the signal intercept and intensity, respectively. The optimization package used a nonlinear least square fit to achieve convergence.

3.2.4 System Performance:

To assess scanner performance, measurements of the system's noise figure, SNR, ^{19}F spectral linewidth, and frequency stability were performed. The noise figure was measured by inputting a known noise source and measuring the baseline difference. The SNR, linewidth, and frequency stability were measured on a TEG containing 150 μL of PFCE inside the solenoidal coil. The SNR measurement was based on a single shot of the adiabatic double spin-echo sequence, leaving out the initial inversion pulse. SNR was calculated according to

$$SNR = \frac{\max(|s(t)|)}{\sigma(|n(t)|)} \cdot \rho, \tag{3.2}$$

where $s(t)$ is the time domain signal, while $n(t)$ is a segment of noise from $s(t)$. $n(t)$ was defined with 60 points or 1 ms of data. $\sigma(|n(t)|)$ defines the standard deviation of the absolute noise. ρ is a Rayleigh correction factor which equals 0.66 [4].

3.2.5 TEG Preparation Protocol:

R_1 measurements were performed on active TEGs. Each TEG was prepared by submerging it in 100% ethyl alcohol for 15 minutes followed by 70% ethyl alcohol for 15 minutes. Once wet, the TEG was placed in a Phosphate-Buffered Saline (PBS, Bio-Rad Laboratories) and 5% Penicillin Streptomycin (penstrep, Nvitrogen Life Technology) solution and stored overnight. This initial procedure wet the TEG's membranes to allow for liquid transfer through the TEG. The PBS washing step removes any residual alcohol prior to use.

A 10% Thrombin (JMI Topical Solution, Pfizer) solution in saline with calcium and magnesium (Bio-Rad Laboratories) was placed into a 5 mL petri dish. The TEG oxygen port was cut to 5 mm and placed into the solution. Air bubbles were removed from the TEG by slowly drawing and injecting the surrounding 10% Thrombin solution through the TEG with a syringe. A 1:1 emulsion of PFCE and Porcine Plasma (Sigma-Aldrich) was mixed. 300 μL TEGs were used for this study with a 1:1 ratio of 150 μL of PFCE and porcine plasma. The emulsion was vortexed, and a Hamilton syringe loaded the emulsion into the TEG. The needle was disconnected from the syringe while still connected to the TEG. The TEG was left to crosslink in the 10% thrombin solution for 5 minutes. The needle was then disconnected, and the TEG was again submerged for 10 minutes to finish crosslinking. Following this, the TEG oxygen port was sealed with a biocompatible NuSil silicon glue. The prepared TEG was transferred to a 50 mL conical with a PBS and 5% Penicillin Streptomycin solution. R_1 measurements at a variety of experimental conditions were performed. The following protocol varied experimental conditions.

3.2.6 Experimental variation of oxygen and temperature:

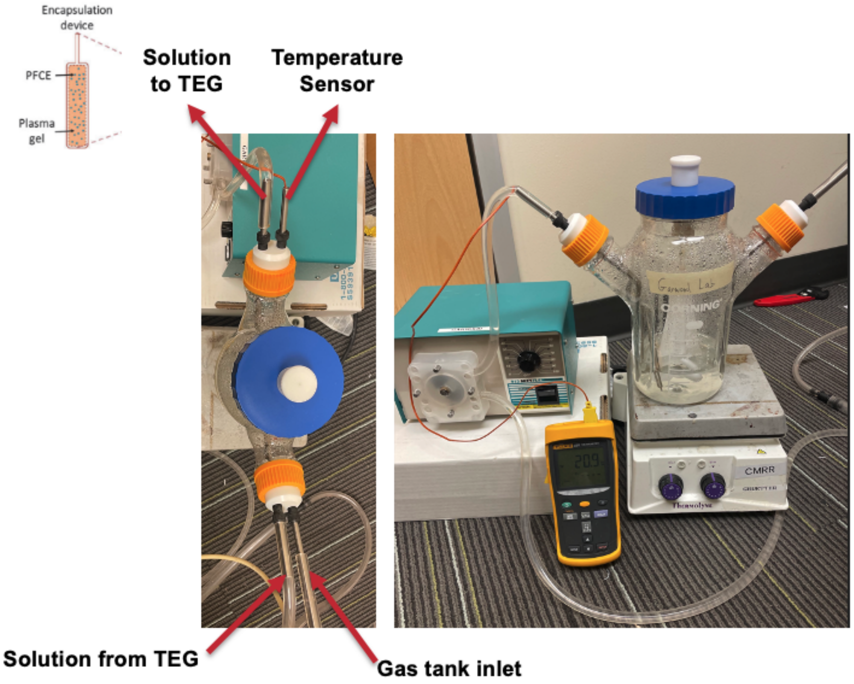

Fig. 3.5. An external solution of phosphate-buffered saline is heated and oxygenated to the wanted experimental conditions. The solution is then pumped into a conical holding the tissue engineered graft (TEG). This experimental setup enabled the accurate control of the TEG's oxygenation and temperature values.

The TEG was submerged in a 50 mL conical and placed inside the solenoid. A tubing setup comprised of 1/3-inch diameter oxygen impermeable tubing (Saint Gobain) connected the 50 mL conical, containing the TEG, to a spinner flask. 550 mL of PBS and 5% Penicillin Streptomycin was placed in the spinner flask. The spinner flask was followed with a peristaltic pump to adjust the flow rate of solution throughout the system. Tygon tubing connected junctions. A tee-junction port was added just before the inlet of the conical for fiber-optic measurement of oxygen saturation with a PreSens (Oxy-1SMA, O2) oxygen sensor 3.5.

The spinner flask had four ports. The first port connected the peristaltic pump and pumped solution from the spinner flask to the TEG, the second port returned solution from the conical containing the TEG to the spinner flask, the third port connected to auxiliary gas tank (either $0\%, 10\%, 20\%$, 30% O_2, source: Minnesota Oxygen), and the fourth port had a thermocouple that measured the temperature of the solution. The spinner flask was placed on top of a hot plate to agitate the solution during oxygenation and heat the solution to the desired temperature. A second oxygen sensor (Pasco airlink, PS-2196) measured room soluble oxygen levels in PBS. The auxiliary tanks bubbled gas into the solution until the desired oxygenation level (measured by the in-port sensor) was reached. This process took 15-20 minutes. If needed, the solution was rewarmed or bubbled between experiments.

Four oxygenation levels were measured: $0, 76, 133$, and 228 mmHg. These values were measured across four different temperature values: 21,33,43, and 53°C. They were selected due to previous clinical validation at similar oxygenation and temperature levels [44]. A total of thirty-six R_1 measurements were taken, with each measurement taking 7 minutes. The measurements took place over 3 consecutive days. In between days, the secondary solution was replaced, while the TEG was refrigerated in a new PBS and Penicillin Streptomycin 50 mL conical. Through all cases, the temperature of the magnet was kept steady at 28°C via its heat regulator (Fig. 3.6).

The resulting data were fit to:

$$R_1 = A + B \cdot pO_2 + C \cdot T + D \cdot pO_2 \cdot T \tag{3.3}$$

where T and pO_2 have units in Celsius and mmHg. A is a term describing dipole-dipole interactions between the nuclear magnetic moments, B arises due to additional dipole-dipole interactions between ^{19}F nuclei and the unpaired electrons of the dissolved oxygen gas, C accounts for the temperature dependence of the correlation time, and D describes the contribution of oxygen and temperature cross-interactions, particularly the temperature dependence of Henry constant [43], [54], [55]. For this study, B is the primary parameter of interest since it describes the pO_2 sensitivity at the field strength used.

3.2.7 Extracting temperature- and oxygen-sensitivity of R_1 at 0.5 T

To perform a multi-parameter fit for Eq. 3.3, an objective function was defined:

$$\operatorname{argmin}_{R_1} |R_1^{\text{exp}} - R_1|^2 \tag{3.4}$$

${R_1}^{\text{exp}}$ is the experimentally measured R_1 at every temperature and oxygenation condition. R_1 is the output of Eq. 3.1, with A, B, C, and D randomly initialized. A Python script minimized the objective function using SciPy's minimization packages; Powell optimization [56] converged the results. The experimental R_1 measurements of all thirty-six measurements were used for minimization. Additionally, three lines of fits were produced - one per temperature condition - demonstrating the probe's oxygen-dependent R_1 values.

3.3 Results

3.3.1 The System

The measured noise figure was 1.15 dB. The measured SNR on an activated TEG was 26.15. The grounding panel (Fig. 3.1) reduced BNC cable noise by -15.2 dB. The heat regulator system kept the magnet's resonance variation within ±200 Hz, while keeping the magnet's temperature steady at 28°C (Fig. 3.6). The magnet was kept at a higher temperature than the room (22°C – 24°C) to reduce temperature variations. Heat regulation reduced field drift by 97%, while the homogeneity of the magnet remained constant with temperature variations.

In experiments, the ^{19}F linewidth varied between 6 - 10kHz, depending on the movement and positioning of the TEG in solution. Broadband pulses, with bandwidths greater than or equal to 10 kHz, appeared to be effective in all experimental conditions.

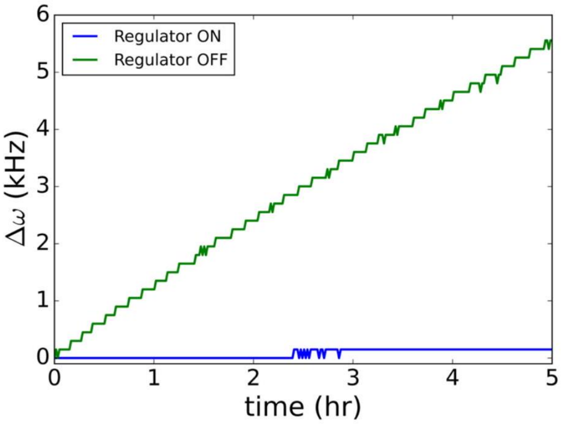

Fig. 3.6. Experimentally measured resonance offset ($\Delta\omega$) of the 0.5 T Halbach with and without temperature regulation. The graph shows the resonance frequency variation of the Halbach over a period of 5 hours. The blue line represents the variation with temperature regulation, while the green line represents the variation without temperature regulation. The resonance frequency varied by > 5000 Hz without temperature regulation, while the variation reduced to only ~ 200 Hz with the heat regulator. The step-like pattern present in both plots is due to the limited spectral resolution of the measurement.

3.3.2 Pulse Sequence and data post-processing:

Logarithmically stepping TI and performing data apodization (Fig. 3.7) allowed an effective fit (Fig. 3.8) of Eq. 3.1. Fits for R_1 values yielded $R^2 > 0.98$ for all temperature and oxygen conditions.

A PBS solution with 5% Penicillin Streptomycin (and overnight refrigeration) was effective at preventing degradation of the TEG between experiments. Fitting errors were low (< 0.1 s), and a linear regression of the temperature- and oxygen-dependent R_1 data demonstrated strong pO_2 sensitivity and linearity ($R^2 > 0.98$ for all curves) (Fig. 3.9, Table 3.2).

A comparison between three identical R_1 measurement protocols demonstrated that no averages were needed. A 3 average, 2 average, and no average scan showed a minimal increase in error. The R_1 error for each condition was ±0.011 s, ±0.018 s, and ±0.020 s, while the scan times for each protocol was 7 min, 5.33 min, and 2.33 min respectively.

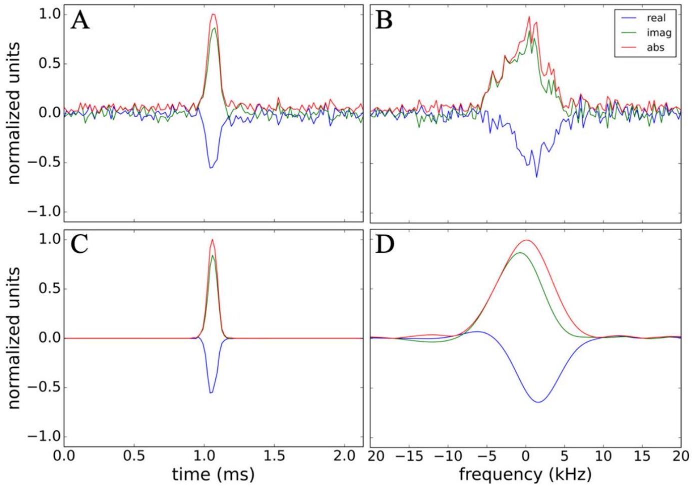

Fig. 3.7. Panel A-B show a ^{19}F double spin-echo measurement conducted on an activated TEG under room temperature conditions without any averaging at 0.5 T. In the time-domain representation (A) and spectrum (B), a noisy echo is observed. To improve the quality of the data, apodization using a Gaussian function was applied. The resulting data, as shown in panels C-D, exhibit significant enhancement in both the time-domain (C) and the spectrum (D) of the echo following apodization. The spectrum shows the approximate linewidth of the experiments, while the time-domain signal shows the drastic reduction of noise after processing.

Parameters	**0.5 T**	**16.4 T**
A $[\mathrm{s}^{-1}]$	2.40	1.65
B $[\mathrm{s}^{-1} \cdot \mathrm{mmHg}]$	$6.39\mathrm{e}-3$	$3.85\mathrm{e}-3$
C $[\mathrm{s}^{-1} \cdot \mathrm{C}^{-1}]$	$-6.01\mathrm{e}-2$	$-1.93\mathrm{e}-2$
D $\left[\mathrm{s}^{-1} \cdot \mathrm{mmHg}^{-1} \cdot \mathrm{C}^{-1}\right]$	$-3.43\mathrm{e}-5$	$-5.67\mathrm{e}-5$

Table 3.2: A Powell minimization of Eq. 3.4 defined the following parameters at 0.5 T. The parameters are compared to the fit values at 16.4 T

3.4 Discussion:

TEGs require supplemental oxygen delivery to prevent anoxic and hypoxic conditions. Hypoxic conditions would deteriorate the cellular populations, while hyperoxic conditions would produce damaging free radicals [38]. A methodology must exist to deliver sufficient oxygen to avoid both conditions. A subsequent question to answer is: How does one appropriately measure oxygen levels *in vivo* to ensure appropriate

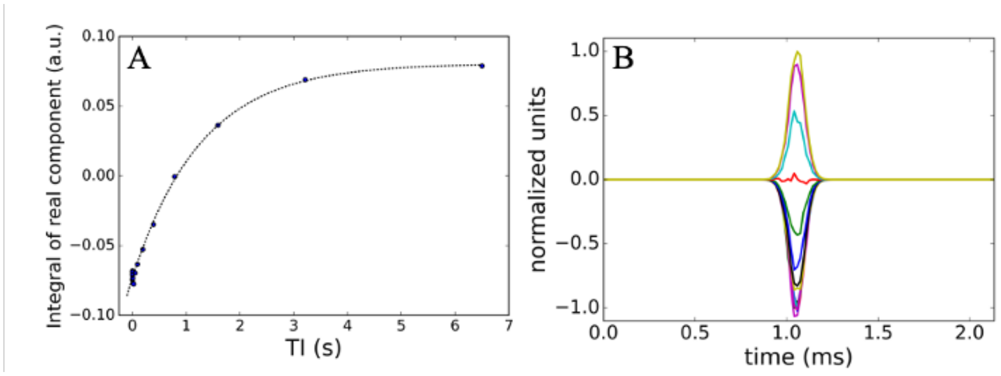

Fig. 3.8. Example of R_1 fitting (A) and a time-domain (echo) data (B) from an experiment on a 300 μL TEG containing 150 μL of an oxygen probe (Perfluoro-15-crown-5-ether). The resulting fit (A) is represented by the dashed line, while the blue dots represent the experimental values. A T_1 of 0.868 s was measured. B) The real component of each spin-echo signal, post apodization, used for the T_1 fit is shown in panel B. Different colors represent different TI values.

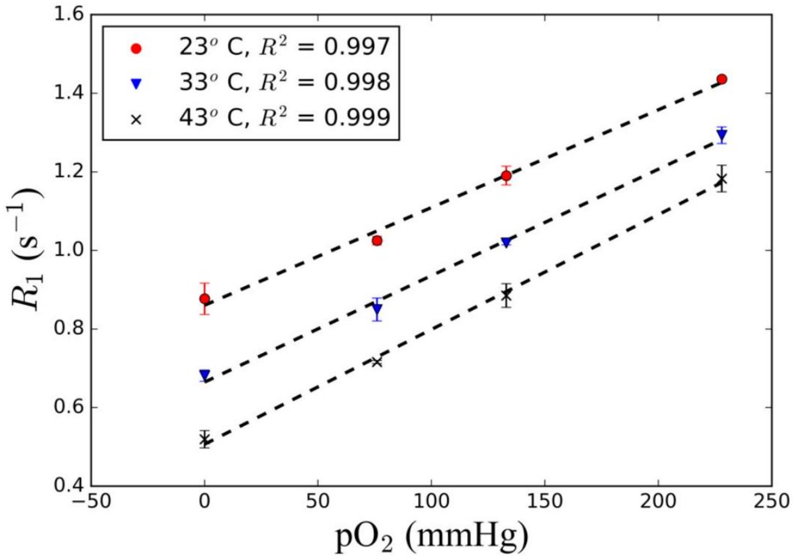

Fig. 3.9. A linear fit of the temperature- and oxygen- dependent R_1 values are shown. Three R_1 measurements were taken per condition and averaged. Error bars show one standard deviation. A strong linear fit was shown for three temperature conditions ($R^2 > 0.995$).

and effective oxygen delivery? Previous studies showed that NMR can measure pO_2

levels in vitro [44] and *in vivo* [42], but they relied on traditional MRI and NMR systems. These systems cannot scale or match the potential demand of future diabetic patients. An effective NMR solution must scale with the potential global reach of TEGs. Here, we presented a compact and affordable 0.5T NMR system that can scale with the future need for TEGs and address oxygenation needs. This system functions with a compact spectrometer based on low-cost electronic components and requires only modest RF power (500 W) to drive a small and simple transceiver coil geometry (e.g., a solenoidal or surface coil). As such, future installations of systems like these in clinics or hospitals should be feasible.

The adiabatic inversion-recovery double spin-echo sequence enabled accurate R_1 estimations despite broad linewidths. Although in the future passive or active shimming could be used to improve SNR, this study shows that, with the broadband adiabatic spin-echo sequence, narrow linewidths are not essential, and thus, this approach may reduce engineering requirements and costs. To be readily accessible to diabetes patients, the NMR system must be able to perform in a variety of temperatures and environments. Permanent magnet NMR systems typically suffer from field drift from temperature variations, but the heat regulator system kept the system's temperature stable and thus largely eliminated frequency drifts. Another disadvantage of permanent magnet systems is the inability to turn the magnet off, as can be done with superconducting systems where the magnet can be quenched for user safety. Future designs will need to minimize safety issues through supplemental designs around the magnet. While for the presented 0.5 T system, the fringe fields rapidly decayed reducing safety concerns.

The system's SNR proved sufficient despite a low volume of ^{19}F perfluorocarbons (150 μL). The success of our system relied on simple engineering solutions. For example, electromagnetic interference due to the lack of a Faraday cage was largely avoided using a custom grounding panel. In the future, however, a more elaborate solution will be required; patients, when placed in the scanner, will be an effective source of EMI. The patient's body can act as an antenna and bring EMI directly to the probe. This is a known issue for portable MRI systems with no Faraday cage. Two primary approaches are used. First, grounding the patient, through a conductive rope or cover, effectively grounds the EMI brought in by the patient. Second, deep learning or signal processing approaches have been shown to remove EMI [57]–[59] through using externally facing coils that measure EMI directly.

If TEGs can cure type 1 diabetes, a widespread need for a portable oxygen-measurement device will be required. This device will need to be portable, affordable, and accessible. Current MRI scanners, although technically effective at measuring pO_2, cannot solve future patient needs. Clinical MRI scanners require MRI technicians, specialized hospital real estate, and a tremendous financial investment. Currently, 90% of the world [1] lacks access to MRI scanners because of these requirements; and it is expected to significantly impact the effectiveness of TEG devices if MRI solutions do not exist. Here, we presented the development of a potential 0.5 T solution. The system was validated through pO_2 temperature and oxygen measurements. The measured pO_2 sensitivity was 1.62-fold larger than that previously measured at 16.4 T [44]. The 0.5 T system seems to provide sufficient field strength to measure pO_2 in perfluorocarbon-containing TEGs. While most importantly, the 0.5 T system works to closely meet the requirements of future patients. The scanner is portable (150 kg), affordable (components totaled $< \$100,000$), and accessible (minimal power requirements) and future software updates could empower the system to be run with minimal training. A system like this might enable TEG devices to meet their full potential in treating the world's diabetic population.

Chapter 4

Magnetic Resonance Imaging

This chapter covers additional background required for chapter 5 and 6.

4.1 Spatial Encoding

Previous sections have covered FID, inversion-recovery, and spin-echo experiments. While these experiments are essential for understanding MRI principles, they do not explain how anatomical images are reconstructed from acquired data. To address this, we now cover how to spatial encode the spins of interest.

To achieve spatial encoding in MRI, the concepts of spatial frequencies and encoding techniques are introduced into the imaging system. This is accomplished through the utilization of the k-space formalism, which provides a framework for determining what signal to acquire in order to reconstruct the region of interest. We begin by describing k-space [60].

4.1.1 Spatial Encoding Principles: k-space

The term 'k-space' [61] refers to the spatial frequency domain in MRI, and the objective of MRI approaches is to sample a sufficient range of spatial frequencies to enable signal reconstruction. The spatial frequency domain is closely related to the temporal frequency domain, which is obtained by applying the Fourier transformation to a time-domain signal. The primary distinction lies in their units: spatial frequen-

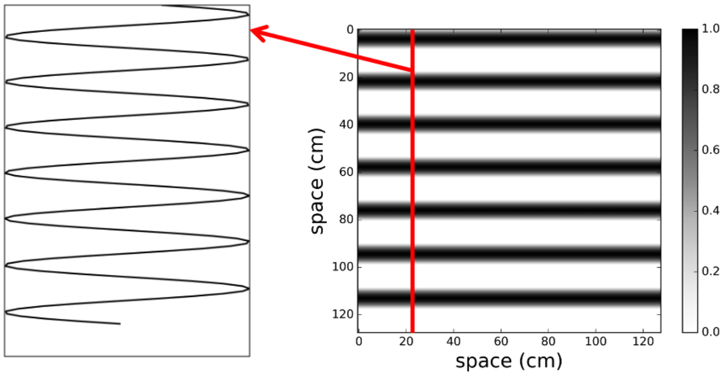

Fig. 4.1. The figure depicts a spatial frequency map on the right and a corresponding vertical slice of the map on the left. It illustrates that spatial frequency is analogous to temporal frequency, with spatial frequency having periodicity in terms of spatial dimensions (such as cycles per meter) instead of time (such cycles per second).

cies are measured in m^{-1}, while temporal frequencies are measured in s^{-1}. Figure 4.1 highlights the similarities between spatial and temporal frequencies.

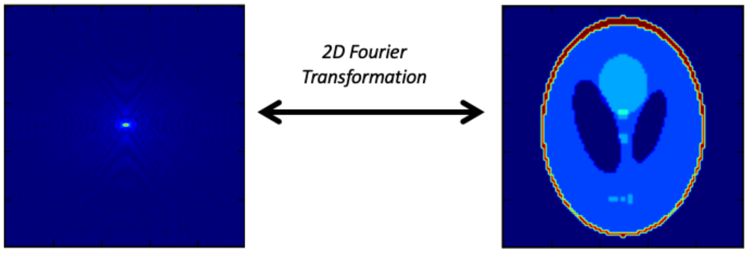

Fig. 4.2. The image on the left represents the magnitude of k-space data for a brain, while the image on the right displays the corresponding reconstructed brain image. The transformation between k-space and image space is achieved through a 2D Fourier transformation (FT) .

MRI approaches manipulate spins to sample a broad range of spatial frequencies. Using Fourier approaches, we reconstruct our object. Figure 4.2 shows the difference between a brain image and its k-space representation.

Spatial frequencies are acquired in MRI by deliberately modulating the Larmor frequencies of the spins in order to precisely control their phase and sample different k-values. This modulation is accomplished using gradient coils. These large coils generate a spatially-dependent magnetic field along a specific axis, causing the Larmor frequency of the spins to change linearly across space [4], [60].

By applying B_0 gradient coil, different spatial frequencies can be encoded. This encoding process is mathematically described by the following equation:

$$k(t) = \gamma \int_0^t dt' G_r \tag{4.1}$$

where k(t) denotes the spatial frequency in time and G_r describes an arbitrary B_0 gradient coil otherwise defined as:

$$G_r = \frac{d\mathbf{B}_0}{dr} \tag{4.2}$$

A linear G_r introduces a linear phase, ϕ_G, across space. The resulting signal at an arbitary phase is defined as:

$$s(t) = \int_0^z \rho(z) e^{i\phi_{G,t}} dz \tag{4.3}$$

Rewritten in terms of k-space values, equation 4.1 can be used to redefine equation 4.3 as such:

$$s(k) = \int_0^z \rho(z) e^{-i2\pi kz} dz \tag{4.4}$$

To achieve different k-values, the length of application and/or strength of the B_0 gradient coil is modulated [4], [60].

In MRI, it is common to employ three pairs of B_0 gradient coils to generate gradients along each spatial direction. These gradients are typically denoted as G_x, G_y, and G_z coils. By utilizing multiple B_0 gradient coil pairs, it becomes possible to traverse through two-dimensional (2D) and three-dimensional (3D) k-space by sampling k-values that are linear combinations of different coil sets. These coil pairs using three primary mechanisms for encoding: phase-encoding, frequency-encoding, and slice-selection. We will now describe each encoding approach in detail.

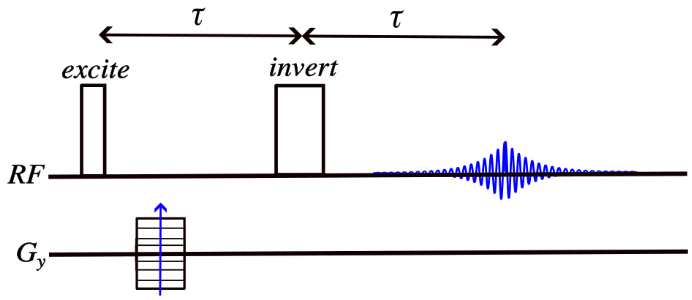

Fig. 4.3. In this 1D phase-encoding experiment, a spin-echo pulse sequence is utilized to generate detectable echoes, while a G_y coil encodes. The phase-encoding process is done by applying a phase-encoding gradient (G_y) before the echo is produced. The duration of the phase-encoding gradient remains constant across multiple experiments, while its amplitude is increased incrementally in N steps. This leads to N experiments, each producing a phase-encoded echo. Applying a Fourier transform (FT) to the collected data, the phase-encoded echoes reconstruct a 1D image. This approach allows for spatial encoding along a single dimension.

4.1.2 Phase Encoding with B_0 Gradient Fields

Instead of sampling the data during the application of the gradient coil, phase-encoding gradient coils are applied with a specific amplitude and duration to position the spins at a particular k-value. The gradient coils are then turned off to allow for data acquisition. Therefore, it is more accurate to represent the k-space equation as follows:

$$k_y = \gamma \int_0^{t'} dt' G_y \tag{4.5}$$

Phase-encoding is inherently slow. In a Cartesian approach, phase-encoding gradients acquire one k-space point for every instance that the G_y gradient coil is applied. An example of a 1D imaging pulse sequence is shown in Figure 4.3 [4], [60].

4.1.3 Frequency Encoding with B_0 gradient fields

Frequency-encoding is the counterpart of phase-encoding. Instead of transitioning to a single k-space point and acquiring the data, frequency-encoding traverses through k-space, and we acquire data during the traversal. This leads to much more

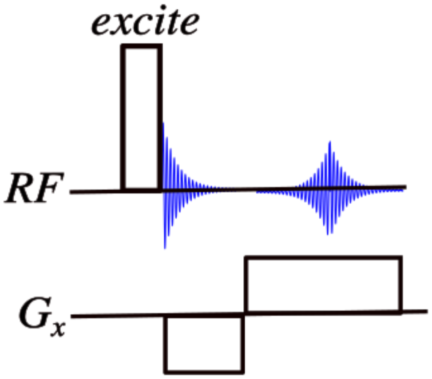

Fig. 4.4. The pulse sequence depicted is a Gradient-Recalled Echo (GRE). First, an RF excitation pulse is applied to tip the spins from their equilibrium state into the transverse plane. Then, a Gx gradient, referred to as the dephasing lobe, is rapidly applied to cause the spins to dephase. Afterwards, a refocusing lobe is applied, which is again the Gx gradient but now with double the length and opposite polarity. The refocusing lobe reverses the spins dephasing and thus refocuses the spins in an echo that is sampled.

data per unit time, and the resulting k-space equation can be defined as:

$$k_x(t) = \gamma \int_0^t dt' G_x(t) \tag{4.6}$$

$G_x(t)$ describes the frequency-encoding gradient. During the k-space traversal, changes in the amplitude, polarity, or length of the B_0 gradient coil can all lead to different k-space values.

A widely used MRI pulse sequence is the Gradient-Recalled Echo (GRE) [62]. In a GRE sequence, spins are initially tipped into the transverse plane. Following this, a frequency-encoding gradient is applied to intentionally induce dephasing by introducing significant variation in the static magnetic field (B_0) across space, which rapidly decreases T_2'. To refocus the spins, the gradient's polarity is flipped, and the duration of its application is doubled. This refocusing step enables the acquisition of an echo signal that traverses k-space. Figure 4.4 illustrates the pulse sequence of a GRE. Using frequency-encoding, we can sample entire lines of k-space at once, rather than a single point at a time (as in phase-encoding) [4], [60].

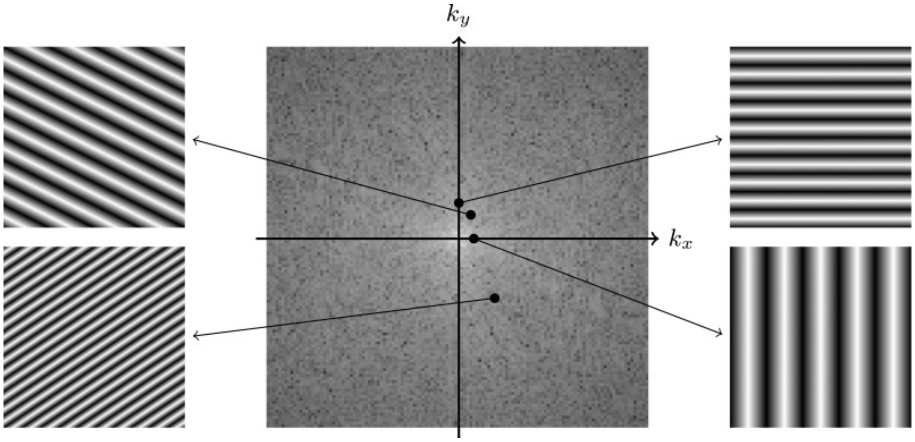

Fig. 4.5. 2D k-space is shown, where k_x represents the horizontal spatial frequencies, and k_y represents the vertical spatial frequencies. Each quadrant of the figure displays the spatial frequencies that result from the combined effects of their corresponding k_x and k_y coordinate frequencies (Courtsey of Allen D. Elster, MRIquestions.com).

4.1.4 2D Imaging with Phase Encoding and Frequency Encoding Gradients

If only a single B_0 gradient coil was used, only 1D phase or frequency encoding could be done. As a result, only 1D imaging could be performed. Fortunately, superposition holds and our 1D k-space formalism quickly expands to 2D. 2D k-space now samples more complex (e.g., diagonal, horizontal, and vertical) spatial frequencies. Figure 4.5 shows an example of different 2D k-space values.

To encode and reconstruct a 2D image in MRI, it is necessary to sample k-values with both k_x and k_y components. This can be achieved by utilizing both phase-encoding and frequency-encoding gradients. In this description, phase-encoding gradients are applied in the y-direction, while frequency-encoding is performed in the x-direction. Consequently, phase-encoding introduces vertical (k_y) traversals in 2D k-space, while frequency encoding introduces horizontal (k_x) traversals [4], [60].

By combining phase-encoding and frequency-encoding gradients, different regions of 2D k-space can be traversed and sampled. Various pulse sequences can be employed, utilizing different settings of the G_y and G_x coils, to navigate specific regions of 2D k-space and acquire the necessary data. A common approach is the 2D

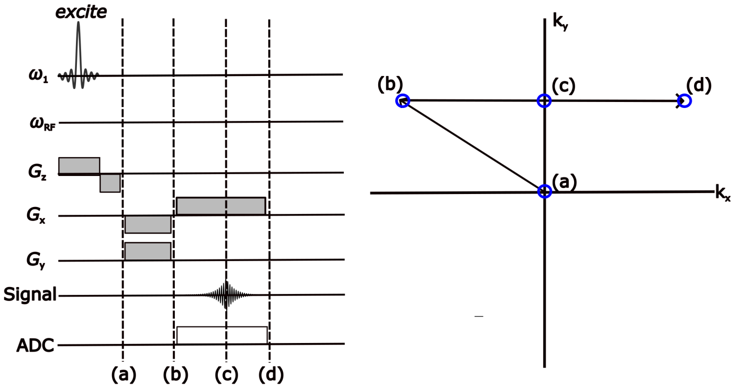

Fig. 4.6. A 3D pulse sequence is shown; the k-space trajectory is shown on the right and labels indicate the k-space point in the pulse sequence equivalently labeled on the left. The G_x and G_y gradients are simultaneously applied to "blip" to a specific position in k-space that has a negative k_x and positive k_y value. Following this, the G_x gradient is responsible for generating a gradient recalled echo. This sequence is repeated with different trajectories until sufficient k-values are sampled to reconstruct the image. The coordinated action of the G_x and G_y gradients enables the efficient encoding and acquisition of spatial information in MRI.

Cartesian trajectory, which is characterized by horizontal and vertical lines in k-space. The corresponding pulse sequence for the 2D Cartesian trajectory is depicted in Figure 4.6, demonstrating the steps involved in acquiring the required k-space data for image reconstruction [15], [63].

4.1.5 Slice Selection with B_0 Gradient Fields

Phase and frequency encoding gradients encode 2D k-space, allowing for subsequent reconstruction of 2D images using the Fourier transformation. However relying solely on frequency and phase encoding is insufficient, as objects are volumetric in nature. A need exists to selectively choose a specific slice from a volumetric object. Slice-selection (or G_z) gradients achieve this. These gradients induce a linear variation in the Larmor frequency along the z-direction. By leveraging this variation, we can selectively excite a desired slice using a narrow-band excitation pulse.

During the excitation process, a gradient in the z-direction is applied and a slice-selective RF excitation pulse is applied with its carrier frequency centered at the

Larmor frequencies of interest. Due to the variation of Larmor frequencies induced by the G_z gradient; a slice is excited. The thickness of the slice is determined by the bandwidth of the excitation pulse [64].

Figure 4.7 demonstrates a pulse sequence depicting the selective excitation process, while Figure 4.8 illustrates the effect of a B_0 gradient across an object, highlighting the slice-selective nature of the excitation.

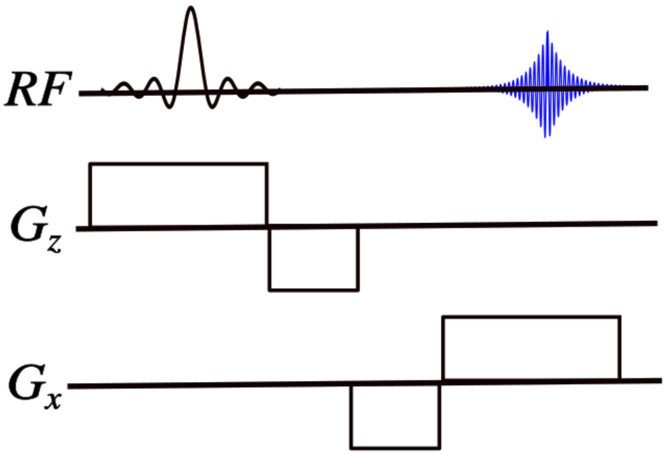

Fig. 4.7. During the transmission of the RF excitation pulse, a slice-select gradient (Gz) is simultaneously applied in the z-direction. This gradient induces a linear variation of the Larmor frequencies along the z-axis. The excitation pulse, typically a narrow-band sinc pulse, selectively excites a slab of spins within the imaging volume. This allows for the imaging of a specific slice or slab of anatomy. However, due to the presence of the B_0 gradient, the excited spins also acquire an unwanted linear phase. To correct for this phase, a gradient with the opposite polarity is applied for half of the excitation duration after the excitation pulse. This reverse gradient effectively unwinds the accumulated phase. Once the slab is selectively excited, a gradient-recalled echo (GRE) experiment is refocuses an echo.

During the transmission of a narrow-band pulse, the slice selection gradient is activated. As a result, the spins at the end of the pulse accumulate a phase that is linearly dependent on the varying B_0 field along the slice. To eliminate this phase and effectively refocus the spins, the polarity of the gradient is reversed and applied for half the duration of its initial activation. This reversal effectively nullifies the

B_0-dependent phase introduced during the slice selection process, thereby achieving complete refocusing of the spins.

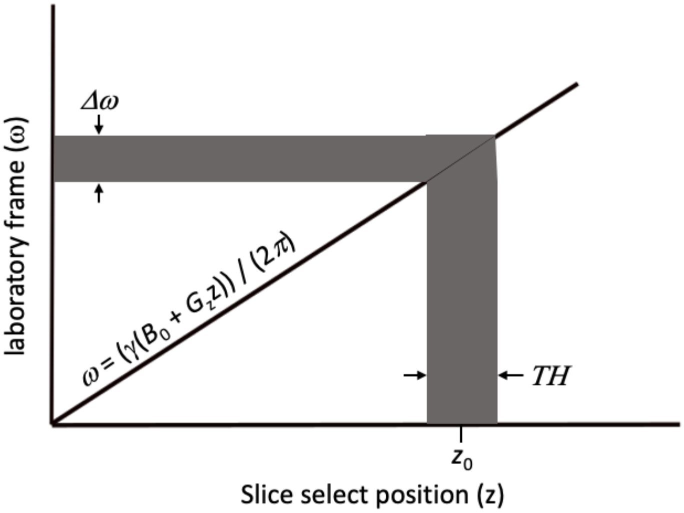

Fig. 4.8. This figure illustrates the spatial modulation of the magnetic field (B_0) using the slice selection gradient (G_z). The slice selection gradient induces a linear variation in the Larmor frequency along the z-axis. This modulation allows for the selective excitation of spins within a specific slice. By applying a narrow-band excitation pulse during the activation of the slice selection gradient, spins located at a particular position (z_0) are excited. The thickness of the selected slice, denoted as TH in the figure, is determined by the bandwidth of the excitation pulse applied while the slice selection gradient is active. In summary, the slice selection gradient in conjunction with the excitation pulse enables the targeted excitation of spins within a specific slice, providing the ability to selectively image a particular region of interest .

The characteristics of the slice profile are determined by the RF waveform used for excitation. A close approximation of the slice profile can be obtained by performing a Fourier transformation of the initial excitation pulse (at low nutation angles). Figure 4.9 illustrates a range of slice profiles achieved by using different excitation pulses.

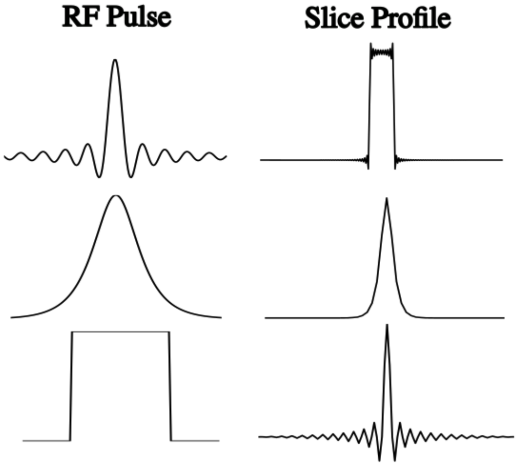

Fig. 4.9. Left displays the radiofrequency (RF) pulse used to selectively excite a slice. The RF pulse is designed to have a specific frequency and duration to target the desired slice thickness. Right illustrates the resulting slice profile. The resulting profile depends on the characteristics of the RF pulse, including its shape and duration.

4.1.6 Volumetric Imaging: A variety of pulse sequences

The approaches covered in the previous sections are the simplest experiments, but demonstrate the fundamentals of spatial encoding. Using G_x, G_y, and G_z coils, MRI pulse sequences can encode in a variety of methods. The presented approaches used Cartesian sampling and leveraged slice selection. Other methods of 3D imaging are possible. For example, phase-encoding can be done in two dimension (e.g., y- and z- phase-encoding) with frequency-encoding in a third. This encoding scheme encodes slabs rather than thin slices and has advantages in SNR, but is typically slower than 2D imaging with slice selection [60].

Additionally, beyond traditional Fourier reconstruction methods, a range of non-Fourier techniques is available for reconstructing images from non-Cartesian trajectories. These methods offer enhanced imaging capabilities and greater flexibility in capturing various types of spatial information. Readers should be aware of the extensive array of available pulse sequences, such as radial and spiral methods, as well as techniques like multi-slice excitation, which have been developed and are routinely employed in clinical practice. Figure 4.10 visually illustrates a diverse set of achievable k-space trajectories, highlighting the versatility of MRI imaging approaches.

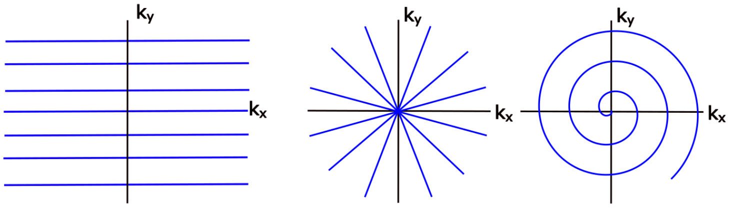

Fig. 4.10. The figure presents three commonly used k-space trajectories in clinical MRI. The blue lines indicate the k-space sampling pattern. On the left is a 2D Cartesian trajectory, which samples k-space in a grid pattern along both the x and y axes. In the center, there's a radial k-space trajectory, where samples are collected radially, emanating from the center outward. On the right, a spiral k-space trajectory is displayed, characterized by a spiral pattern. Each trajectory offers its own set of advantages and considerations, particularly in relation to imaging speed, artifact sensitivity, and available reconstruction methods.

A major advantage of MRI is its versatility in encoding schemes and pulse sequences. Each pulse sequence has its trade-offs in speed, signal-to-noise, and image resolution. Dependent on the clinical need, MRI technologists may utilize different pulse sequences for different patients and clinical questions [63].

4.2 B_1 Imaging Approaches

Traditional MRI uses B_0 gradient coils to spatially encode by spatially-varying the Larmor frequencies. In place of this, B_1 imaging approaches employ spatially-varying B_1 coils to alter the spins nutation frequency, otherwise known as Rabi frequencies, across space. The spatially-varying B_1 coil can thus control the phase of spins using the spatially-dependent frequencies, bypassing the need for B_0 gradient coils. In B_1 imaging, Rabi frequencies, rather than Larmor frequencies, do the encoding. If successful, B_1 imaging offers several advantages over B_0 imaging:

1. B_1 coils offer high waveform fidelity, facilitating the implementation of complex waveforms.

2. B_1 coils operate silently, eliminating the noise commonly associated with B_0 gradient coils.

3. B_1 coils are significantly more cost-effective when compared to B_0 gradient coils, reducing cost.

4. B_1 coils are compact and can be placed directly on the patient, resulting in closer proximity to the imaging target.

Despite these advantages, B_1 imaging remains underutilized and underdeveloped, and to date, has not been integrated into any clinical scanners. This thesis will briefly cover three B_1 imaging approaches and outline the specific drawbacks and challenges associated with each, and end with the presentation of a novel B_1 imaging approach.

4.2.1 Rotating Frame Zuegmatography

The first B_1 imaging approach, Rotating Frame Zuegmatography (RFZ), postulated that Eq. 4.6 can be rewritten in terms of B_1:

$$G_r = \frac{dB_1(r)}{dr} \tag{4.7}$$

and

$$k_r(t) = \gamma \int_0^t dt' G_r(t') \tag{4.8}$$

where r denotes space. In the RFZ method, a B_1 gradient is used to transmit RF pulses that achieve both spatial encoding and excitation simultaneously. At the end of each pulse, the phase of the spins are linearly dependent on the B_1 gradient. RFZ varies the lengths of the pulses and introduces a variable spatial phase, thereby enabling the sampling of different k-values. Figure 4.11 illustrates the RFZ pulse sequence employed. As a phase-encoding approach, RFZ produces N phase encodes in N experiments [65].

RFZ, despite being the inaugural B_1 imaging technique and having had some success in imaging, encountered several challenges:

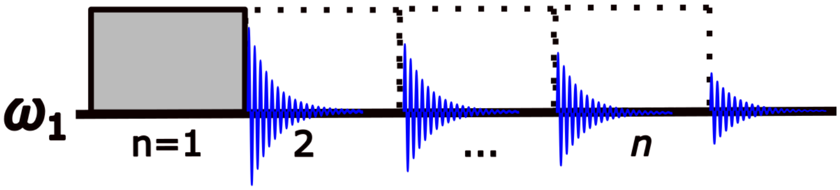

Fig. 4.11. The Rotating Frame Zuegmatography (RFZ) pulse sequence is depicted. A B_1 field gradient transmits a square wave whose pulse length is incrementally increased. The varying pulse lengths introduce various levels of phase. The resulting free induction decay (shown in blue) is sampled to capture the phase-encoded data, which is reconstructed with a Fourier Transformation.

1. Lengthening the AM pulse to introduce more phase alters the pulses' excitation bandwidth. This posed issues when encoding spins with different Larmor frequencies, which could result from inhomogeneous magnets.
2. B_1 gradients are unable to transmit a spatially uniform flip angle when AM pulses are used. As a result, RFZ changes the flip angle profile for each shot, which diminishes the available signal for encoding and degrades image quality.
3. In the presence of off-resonance, spins do not tip to the yz-plane but precess around a cone, as shown in Figure 4.12. This behavior significantly limits the effectiveness of RFZ in scanners with inhomogeneous magnets.

These challenges have impeded the widespread clinical adoption of RFZ as a B_1 imaging method. Despite these limitations, RFZ continues to serve as a valuable foundation for further explorations and understandings in the field of B_1 imaging.

4.2.2 Transmit Array Spatial Encoding

Transmit Array Spatial Encoding (TRASE) [18], [66] provides an alternative B_1 phase-encoding method. Unlike RFZ, TRASE employs specialized RF coils that are explicitly designed for phase encoding [67]. These coils are wound with an extensive amount of wire and serve two main functions:

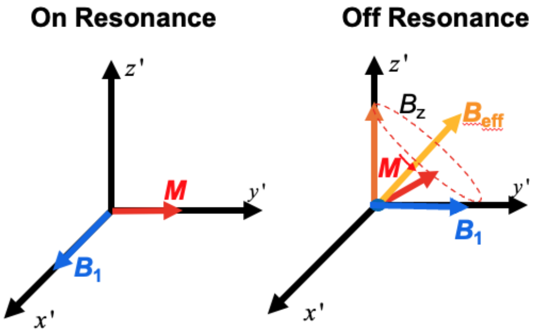

Fig. 4.12. The figure illustrates the outcome of transmitting a 90-degree B_1 pulse under two different conditions: on resonance and off resonance. In the on resonance scenario, where the frequency of the pulse matches the spins' resonance frequency, the spins are tipped perfectly in the -y' direction. However, in the off-resonance case, where there is an additional field (B_z) due to B_0 inhomogeneity, the spins undergo precession around the effective magnetic field (B_{eff}) rather than reaching the -y axis. This off-resonance effect results in a deviation of the spin orientation from the desired location.

1. The specialized RF coils aim to ensure a uniform inversion of spins across the designated imaging region.
2. The topology of these coils are engineered to leave a linear phase variation across the space being imaged. Remarkably, this linear phase is a direct result of the coils' design, obviating the need for specific pulse sequences.

TRASE techniques have shown the ability to mimic many B_0 phase-encoding methods. However, it's crucial to acknowledge the limitations that come with TRASE. First, TRASE methods are vulnerable to B_0 field variations, posing challenges in maintaining consistent and accurate spatial encoding across the imaging area. Second, TRASE constitutes a specialized hardware solution, relying on a particular coil geometry that constrains its flexibility in clinical settings.

While TRASE has pioneered a unique approach to B_1 imaging using specialized RF hardware, its hardware-dependent nature could limit its practicality in clinical scenarios. Moreover, its susceptibility to B_0 off-resonance still calls for the use of expensive homogenous superconducting magnets.

4.2.3 Bloch-Siegert Shift Encoding

Bloch-Siegert shift encoding takes advantage of highly off-resonant RF pulses [68] [69]. When a pulse is transmitted that is highly off-resonant and satisfies the following condition

$$\frac{\Delta\omega_{RF}}{\omega_{B_1}} >> 1 \tag{4.9}$$

a frequency shift of the Larmor frequency occurs. This takes the form of:

$$\omega_{BS} = \frac{\omega_{B_1}^2}{2\Delta\omega_{RF}} \tag{4.10}$$

Assuming a fairly homogeneous B_0 field upon transmission, the phase accrued by a Bloch-Siegert pulse is equal to:

$$\phi_{BS} = \int_0^t \omega_{BS}(t)dt. \tag{4.11}$$

The phase can be varied linearly by introducing a B_1 gradient:

$$\phi_{BS}(r) = \int_0^t \omega_{BS}(r,t)dt \tag{4.12}$$

where,

$$\omega_{BS}(r) = \frac{\omega_{B_{1(r)}}^2}{2\Delta\omega_{RF}} \tag{4.13}$$

Bloch-Siegert shift encoding is another phase encoding that has shown a variety of 1D and 2D results. Additionally, slice-selection using the BS-effect has likewise been shown [70]. Of the approaches covered, Bloch-Siegert imaging shows the most promise in clinical utility. Despite this, the primary downsides of BS-encoding lies in the use of high-power pulses and sensitivity to off-resonance.

4.2.4 RF Imaging Challenges

A variety of approaches have demonstrated effective phase encoding using RF imaging pulse sequences and hardware. Despite these advancements, three primary challenges persist across all methodologies presented: 1) SAR constraints, 2) off-resonance effects, and 3) slow imaging rates [71]. Slow imaging arises from most RF imaging approaches being phase-encoding methods, although they could be accelerated using fast spin-echo train techniques. SAR constraints, as described by Equation 4.14, are substantially mitigated by the use of mid to ultra-low field systems due to the B_0^2 term [72].

$$SAR = \frac{\sigma A^2 \gamma B_0^2 B_1^2 D}{2\rho} \tag{4.14}$$

Additionally, experimental B_1 imaging with spin-echo trains was able to safely be completed half the FDA safety factor (10-g SAR of 5.0 W/kg) [73]. Despite this, sensitivity to off-resonance effects remains an unresolved issue across all B_1 imaging approaches. We will now introduce a novel B_1 imaging method capable of operating in highly imperfect B_0 fields. This technique, termed Frequency-modulated Rabi Encoded Echoes, is capable of both phase and frequency encoding and has been experimentally demonstrated on 1.5 T and 0.5 T systems. Notably, the 0.5 T system operated without the need for passive or active shims and without B_0 gradient coils.

Chapter 5

Phase-Encoding Frequency-modulated Rabi Encoded Echoes

5.1 Introduction

MRI permits robust, high-resolution imaging with tunable contrast that makes it an indispensable tool in clinical medicine and biomedical research. Several groups have focused on redesigning key components of the MRI system in order to lower the financial burden of the technology and increase its access to a wider array of communities [1], [3], [74], [75]. Attempts at improving portability have mainly focused on ultralow field MRI (< 0.1 Tesla [T]), coupled with artificial intelligence techniques to improve image reconstruction and de-noising. Other approaches have focused on reducing the cost by specifically targeting B_0 gradient systems. Elimination of the conventional linear B_0 gradient coils would reduce the maintenance needs and operational requirements of the system. Moreover, gradient coils occupy precious space within the magnet bore while creating potentially damaging levels of acoustic noise [76]. As a viable alternative, silent MRI without B_0 gradients would lower the financial burden of MRI and improve the portability, thus increasing the accessibility of this technology.

This work introduces a method to encode information using a spatially dependent RF field (B_1), which allows for the removal of one or more of the B_0 gradient coils conventionally used in MRI. Previous radiofrequency imaging (RFI) techniques have pursued this goal with limited success. In particular, rotating frame zeugmatography [65] and other early RFI approaches are limited by their sensitivity to resonance offset, $\Omega = \omega_0 - \omega_{\mathrm{RF}}$, where ω_0 is the Larmor frequency and ω_{RF} is the B_1 carrier frequency. With these methods, spatial information is encoded by evolving spins about an effective field ($\mathbf{B}_{\text{eff}}$),

$$\mathbf{B}_{\text{eff}} = B_1\widehat{x'} + (-\Omega/\gamma)\hat{z'} \tag{5.1}$$

in the rotating frame (x', y', z'), where γ is the gyromagnetic ratio. Transmit array spatial encoding, a more recent approach, faces a similar issue [77] and requires specialized coils with complex pulse patterns. Whereas Bloch-Siegert shift encoding [68] has demonstrated promising results, it requires high power to add phase shifts from off-resonant pulses and is still susceptible to resonance offset effects.

The technique introduced herein, frequency modulated Rabi-encoded echoes (FREE), is a frequency modulated (FM) RFI method that accomplishes spatial encoding using adiabatic full passage (AFP) pulses in spin-echo sequences. FREE encodes spatial information in the phase of the magnetization, similar to conventional phase encoding, which results when adiabatic pulses are transmitted with a spatially varying RF field amplitude $B_1(r)$, where r is varying position. Simulations show FREE signal intensities to be minimally affected by resonance offset, and multidimensional MRI is feasible when combining FREE with conventional frequency encoding using a B_0 gradient.

5.2 Theory

5.2.1 FREE spatial encoding

When using an AFP as the refocusing pulse in a spin-echo sequence, the phase of the resulting transverse magnetization is a function of the temporal and spatial properties of the RF field, $B_1(r,t)$ [22], [24]. This B_1-dependent phase is additive to the B_0-dependent quadratic phase resulting from the FM sweep [22], [26]. When executed adiabatically, an AFP performs a slow sweep of $\mathbf{B}_{\text{eff}}$ such that a perpendicular magnetization vector remains approximately perpendicular with $\mathbf{B}_{\text{eff.}}$ To help visualize this, a trajectory of a magnetization vector during a single AFP pulse is depicted in Figure 5.1. The B_1 dependence of the resulting magnetization phase has previously been exploited for B_1 mapping [78], whereas here it is exploited to accomplish B_1-dependent phase encoding.

The application of two AFP pulses with identical time-bandwidth product in a double spin-echo sequence leads to refocused magnetization, removing all B_0 - and B_1-dependent phase factors. With AFP pulses, the bandwidth BW_Ω of refocusing can be held fixed when increasing the pulse duration T_{p} simply by scaling the amplitude of the pulse's phase-modulated function proportionately, as described below. A key parameter in FREE is the unitless time-bandwidth product, $R\,(= T_{\text{p}} \cdot BW_\Omega)$. Application of two AFPs with differing R values leads to residual B_1-dependent phase in the echo, with some dependence on Ω. FREE exploits the B_1-dependent phase in conjunction with a B_1-coil map to perform phase encoding.

The FREE implementation introduced herein is a simple multi-shot double spin-echo (DSE) sequence utilizing two AFP pulses. Although many different pulse shapes can be used, pulses of the hyperbolic secant (HSn) family [24] were chosen. In the FREE sequence (Figure 5.2), the phase induced by one HSn pulse of a given R value is modulated by a second HSn pulse having a different R value to impart an approximately linearly varying spatial phase. BW_Ω is held constant as T_{p} of one of the HSn pulses changes from one excitation of the sequence (shot) to the next. The difference in the time-bandwidth product ($\Delta R = \Delta T_{\text{p}} \cdot BW_\Omega$) of each shot causes a proportional change in the phase to be imprinted on the ensuing echo.

HSn pulses remain a popular class of AFP pulses due to their ability to deliver uniform inversion profiles across large bandwidths. In angular velocity units, the amplitude-modulated (AM) and FM functions of an HS1 pulse can be written as

$$\omega_1(t) = \omega_1^{\max} \operatorname{sech}\left(\beta\left(\frac{2t}{T_{\text{p}}} - 1\right)\right) \tag{5.2}$$

$$\omega_{\text{RF}}(t) = \omega_{\text{c}} + A \tanh\left(\beta\left(\frac{2t}{T_{\text{p}}} - 1\right)\right), \tag{5.3}$$

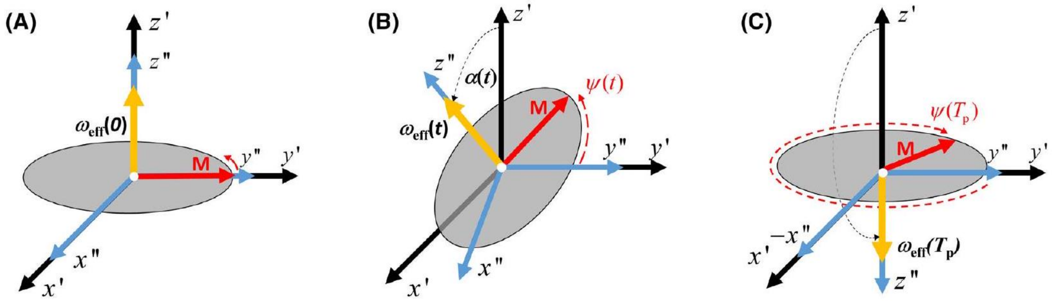

Fig. 5.1. A depiction of the trajectory of an arbitrary **M** and its phase accumulation throughout an AFP in a first (x′, y′, z′) and second (x″, y″, z″) rotating frame of reference. At the beginning of the AFP pulse (A), **M** is in the transverse plane and all rotating frames are aligned. During the AFP (B), **M** evolves at the ω_{eff} as the effective field rotates by $\alpha(t)$, ending with flipped transverse magnetization (C). Phase $\psi(t)$ is accrued over the duration of the AFP. At the end of the pulse, the second rotating frame is inverted relative to the first frame, and the final phase accrued is $\psi\,(T_{\text{p}})$. AFP, adiabatic full passage; **M**, magnetization vector; ω_{eff} , effective frequency

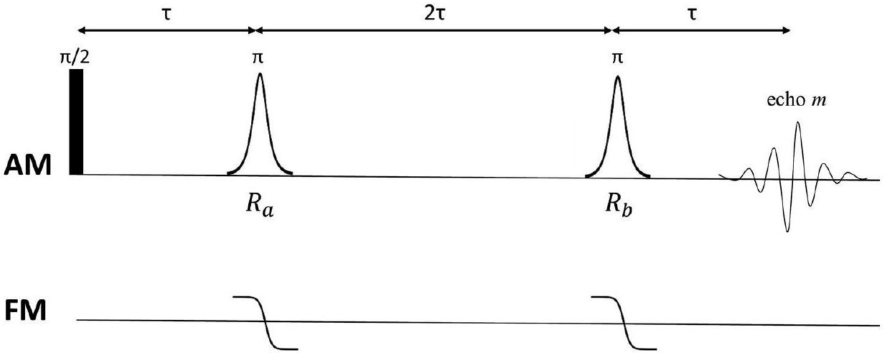

Fig. 5.2. Differences in R value between two AFPs (here denoted as R_{a} and R_{b}) in a double spin echo sequence imprint phase in the resulting echo (m). The black excitation pulse can be any pulse that produces a $\pi/2$ flip, such as an adiabatic half passage or a square pulse when applied with a coil producing a uniform B_1 field. Holding the value of R_{a} constant while sweeping the R_{b} permits linear phase to be encoded across shots. FREE is performed as presented here in a double spin echo sequence, with multiple shots linearly sweeping the R values to sample phase in accordance to the Nyquist criteria. FREE, frequency-modulated Rabi-encoded echoes; m, echo number

where $\omega_1^{\max}$ is the peak Rabi frequency that varies spatially in FREE; ω_c is the center frequency of the FM sweep; A is the frequency-sweep cutoff ($= 0.5\ BW_\Omega$); and β is a unitless truncation factor set such that $\operatorname{sech}(\beta) = 0.01$ (i.e., the amplitude modulated function truncates at 1% of maximum). For an HSn pulse with $n > 1$, the FM function must be obtained by numerical integration according to

$$\omega_\mathrm{RF}(t) = \omega_\mathrm{c} + \int_0^t A \operatorname{sech}^2\left(\beta\left(\frac{2v}{T_\mathrm{p}} - 1\right)^n\right) dv, \tag{5.4}$$

where n is a parameter that controls the flatness of the AM function, [24] and v is a dummy integration variable. In a reference frame that rotates at the instantaneous frequency $\omega_\mathrm{RF}(t)$, the magnetization evolves about $\mathbf{B}_\mathrm{eff}$ at an effective frequency dictated by the vector sum of the AM and FM functions,

$$\omega_\mathrm{eff}(t) = \omega_1(t)\hat{x'} + (\omega_\mathrm{RF}(t) - \omega_\mathrm{c})\,\hat{z'} \tag{5.5}$$

In practice, these types of AFP pulses are implemented using a phase-modulated function, which is related to the FM function by

$$\phi(t) = \int_0^t (\omega_\mathrm{RF}(v) - \omega_\mathrm{c})\, dv. \tag{5.6}$$

In the analysis to follow, the variable ψ is the $\omega_1^{\max}$ -dependent phase of the transverse magnetization produced by an AFP pulse in the FREE sequence. A plot of ψ as a function of $\omega_1^{\max}$ is shown in Figure 5.3. Within the approximation that ψ is a linear function of $\omega_1^{\max}$, the double spin-echo FREE method is similar to conventional phase encoding with a B_0 gradient.

5.2.2 Propagator analysis

By assuming the adiabatic condition is fully satisfied and that the net rotation of $\mathbf{B}_\mathrm{eff}$ approaches π, an analytical expression for the double spin-echo FREE sequence can be obtained using propagator analysis [6]. When starting with transverse magnetization, the B_1-dependent phase accrued from an HSn pulse is given by

$$\psi(r) = \pm\frac{T_p}{2}\int_{-1}^{1}\omega_{\text{eff}}(\tau, r)d\tau \tag{5.7}$$

where $\tau = 2t/T_{\text{p}} - 1$, and the effective evolution frequency according to Equation 5.5 is expressed as

$$\omega_{\text{eff}}(r,\tau) = \sqrt{\left(\omega_1^{\max}(r)\operatorname{sech}\left(\beta\tau^n\right)\right)^2 + \left(\frac{\int_0^{\tau} A\operatorname{sech}^2\left(\beta\tau^n\right)d\tau}{\int_0^{1}\operatorname{sech}^2\left(\beta\tau^n\right)d\tau}\right)^2} \tag{5.8}$$

The sign in Equation 5.7 depends on the direction of the frequency sweep, which is taken to be positive in the present work. For compactness, the r-dependence of ψ is assumed in the analysis going forward.

The propagator describing any AFP pulse that is executed adiabatically is

$$U = \exp\left(i\phi_0 I_{\text{z}}\right)\exp\left(i\Delta\alpha I_{\text{y}}\right)\exp\left(-i\phi_0 I_{\text{z}}\right)\exp\left(i\psi I_{\text{z}}\right), \tag{5.9}$$

where $\Delta\alpha$ is the total angle swept by $\mathbf{B}_{\text{eff}}$ and ϕ_0 is the initial phase of the pulse. When assuming the adiabatic condition is fully satisfied, the transformations applied to the components of the magnetization vector can then be described analytically [22]:

$$\begin{gathered}UI_{\text{x}}U^{-1} = I_{\text{x}}\left(\cos\left(\psi-\phi_0\right)\cos\Delta\alpha\cos\phi_0 - \sin\left(\psi-\phi_0\right)\sin\phi_0\right) + \\ I_{\text{y}}\left(\sin\left(\psi-\phi_0\right)\cos\phi + \cos\left(\psi-\phi_0\right)\cos\Delta\alpha\sin\phi_0\right) + I_z\left(\cos\left(\psi-\phi_0\right)\sin\Delta\alpha\right)\end{gathered} \tag{5.10}$$

$$\begin{gathered}UI_{\text{y}}U^{-1} = I_{\text{x}}\left(-\sin\left(\psi-\phi_0\right)\cos\Delta\alpha\cos\phi_0 - \cos\left(\psi-\phi_0\right)\sin\phi_0\right) \\ +I_{\text{y}}\left(\cos\left(\psi-\phi_0\right)\cos\phi_0 + \sin\left(\psi-\phi_0\right)\cos\Delta\alpha\sin\phi_0\right) + I_{\text{z}}\left(\sin\left(\psi-\phi_0\right)\sin\Delta\alpha\right)\end{gathered} \tag{5.11}$$

$$UI_{\text{z}}U^{-1} = I_{\text{x}}\left(\cos\phi_0\sin\Delta\alpha\right) + I_{\text{y}}\left(\sin\left(\phi_0\right)\sin\Delta\alpha\right) + I_{\text{z}}(\cos\Delta\alpha) \tag{5.12}$$

From this general propagator, an inversion of $\mathbf{B}_{\text{eff}}$ (i.e., $\Delta\alpha = \pi$) can be expressed in rotation matrix form as

$$U_\pi = \begin{bmatrix} -\cos(2\phi_0 - \psi) & -\sin(2\phi_0 - \psi) & 0 \\ -\sin(2\phi_0 - \psi) & \cos(2\phi_0 - \psi) & 0 \\ 0 & 0 & -1 \end{bmatrix} \tag{5.13}$$

Concatenating two AFP pulses with equal pulse parameters ($R_\mathrm{a} = R_\mathrm{b}$ in Figure 5.2) leads to an identity transform, for example,

$$U_{\pi,a} U_{\pi,b} = \begin{bmatrix} 1 & 0 & 0 \\ 0 & 1 & 0 \\ 0 & 0 & 1 \end{bmatrix}. \tag{5.14}$$

Similarly, for the case of $\phi_0 = 0$, a rotation matrix can be obtained for two AFPs of the same BW_Ω but with differing T_p values,

$$U_{\pi,a} U_{\pi,b} = \begin{bmatrix} \cos(\psi_a - \psi_b) & -\sin(\psi_a - \psi_b) & 0 \\ \sin(\psi_a - \psi_b) & \cos(\psi_a - \psi_b) & 0 \\ 0 & 0 & 1 \end{bmatrix}. \tag{5.15}$$

Equation 5.13 is the Euler matrix for a rotation about the z-axis, and as such the net phase after applying two AFP pulses is

$$\Delta\psi = \psi_a - \psi_b. \tag{5.16}$$

The propagator (Equation 5.15) demonstrates phase encoding based on a $B_1(\mathrm{r})$ gradient through the analysis of a multi-shot approach of FREE in which one phase encoded data point is acquired per shot. In consecutive shots, the R value of one of the pulses in the DSE is held constant, whereas the R value of the other pulse is incrementally stepped via changing T_p at fixed BW_Ω. Figure 5.4 shows the linear relationship between the phase of the resulting magnetization ($\Delta\psi$) and the peak RF field ($\omega_1^{\max}$) for different shots m, as predicted from this propagator analysis.

The bandwidth of FREE frequencies is given by the difference of the phase angles

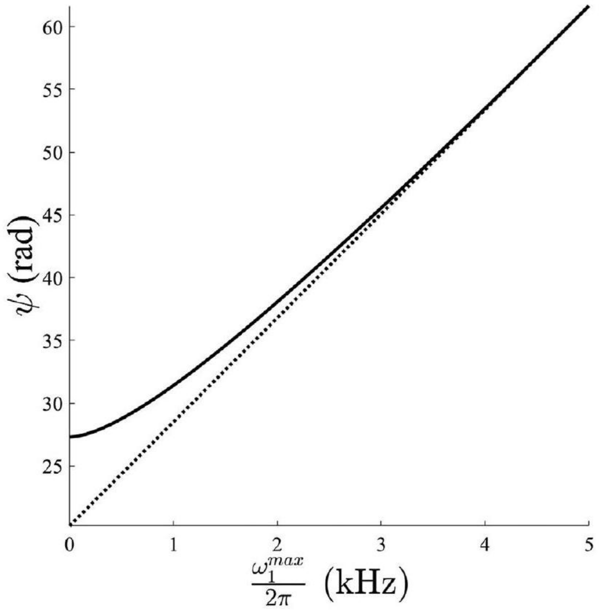

Fig. 5.3. The solid line demonstrates the result of numerical integration of ω_{eff}, which describes the magnetization phase from an HSn pulse (here $n = 1$) across a linearly varying RF field amplitude ($\omega_1^{\max}$) from 0 to 5 kHz, with a $T_{\mathrm{p}} = 20$ ms and $BW_{\Omega} = 2$ kHz. From the plot, clear nonlinearities arise from lower $\omega_1^{\max}$ values. The dashed line is used for comparison to clearly distinguish the nonlinearity present. It is not the result of any integration. That is, at low RF amplitudes, nonlinearity in the accumulated phase arise even with a linear B_1 gradient in space, demonstrating the importance of using high RF amplitudes in FREE. ω_{eff} , effective frequency; T_{p}, length of pulse; BW_{Ω}, pulse bandwidth; HS, hyperbolic secant

(Equation 5.17) divided by the time increment ΔT_{p},

$$BW_{\text{FREE}} = \frac{1}{\Delta T_{\mathrm{p}}} \left(\Delta\psi_{\max} - \Delta\psi_{\min} \right), \tag{5.17}$$

where

$$\Delta\psi_{\max} = \psi_a \left(r_{\max} \right) - \psi_b \left(r_{\max} \right) \tag{5.18}$$

$$\Delta\psi_{\min} = \psi_a \left(r_{\min} \right) - \psi_b \left(r_{\min} \right) \tag{5.19}$$

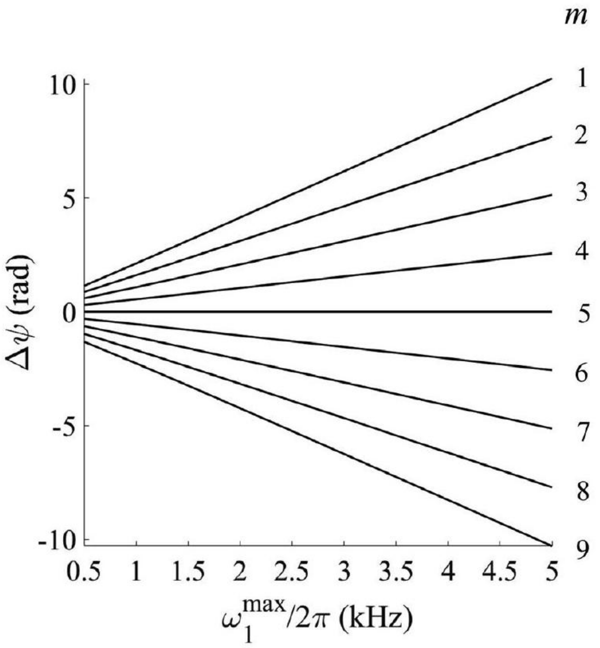

Fig. 5.4. Plot showing how the magnetization phase varies in the FREE sequence as a function of RF amplitude ($\omega_1^{\max}$) and shot number. The calculation is based on the propagator describing two AFPs in a double spin echo sequence. The duration T_p of one AFP was held constant throughout shots (at a $T_\mathrm{p} = 10$ ms), whereas the other was incremented by $\Delta T_\mathrm{p} = 0.15$ ms in consecutive shots, beginning at $T_\mathrm{p} = 3.1$ ms. BW_Ω of both pulses was 5 kHz. Phase accumulated linearly across shots and also while increasing $\omega_1^{\max}$.

The variables $r_{\max}$ and $r_{\min}$ are the coordinates of the maximum and minimum Rabi frequencies, respectively, in the field of view (FOV).

5.2.3 k-space description

The R value of one AFP is incremented by ΔR in consecutive shots of the DSE sequence. The resulting magnetization phase increments are approximately linearly dependent on $\omega_1^{\max}$ and $\omega_{\text{eff.}}$ This process is equivalent to stepping through k-space, as done in conventional phase encoding. To further this analogy, a relationship between Δk and ΔR is developed here for any HSn pulse. [24] Δk is derived by performing the spatial derivative of $\Delta\psi$ in the FREE-encoding direction,

$$\Delta k = \frac{d\Delta\psi}{dr}. \tag{5.20}$$

When assuming ψ has a linear spatial dependence (see Figure 5.3), the expression becomes

$$\Delta k = \frac{BW_{FREE} \cdot \Delta T_p}{FOV} = \frac{BW_{FREE} \cdot \Delta R}{FOV \cdot BW_{\Omega}}. \tag{5.21}$$

In practice, the spatial variation of $\omega_1^{\max}$ may not be linear. As such, the derivative of $\Delta\psi$ (Equation 5.20) is not a constant, and hence Δk is spatially dependent.

By utilizing Δk in Equations 5.20 and 5.21, k-space can be sampled in accordance with Nyquist through multiple shots (m) of the sequence in Figure 5.2. The designation R_{a} and R_{b} are used for the first and second AFP pulses. To sample k-space from $-k_{\max}$ to $+k_{\max}$ with increment $\Delta k, R_{\mathrm{a}}$ is stepped from $R_{\min}$ to $R_{\max}$ while holding R_{b} constant, where

$$R_{\min} = R_b - \frac{M}{2} \cdot \Delta R \tag{5.22}$$

$$R_{\max} = R_b + \frac{M}{2} \cdot \Delta R \tag{5.23}$$

and M is the maximum number of shots, as well as data points, to be sampled. This proposed sequence samples k-space via multiple shots, beginning with sampling $-k_{\max}$ and incrementing by Δk until reaching $+k_{\max}$. To change $\Delta k, BW_{\mathrm{FREE}}$ can be changed in accordance with Equation 5.21. The analysis of Δk above assumes a linear B_1 gradient; when using a nonlinear B_1 gradient, the pixel size changes in accordance with the nonlinearity, creating distortions in the reconstructed object as the number of spins per pixel varies depending on local B_1 gradients.

As in conventional phase encoding, k-space data can be acquired in any order, although FREE offers some added flexibility. Specifically, the multi-shot sequence chosen here minimizes the maximum T_{p} necessary. Rather than holding the stationary pulse constant and incrementing the R value of the modulating pulse from $R_{\min}$ to $R_{\max}$ by ΔR, the modulating pulse is incremented by ΔR until $R_{\min}$ is equal to R_{b}. Then the order of pulses exchanges and the modulating pulse R value increments from R_{b} back to R_{min}. This change makes the maximum $T_{\mathrm{p}} = R_{\mathrm{b}}/BW_{\Omega}$ as opposed to $T_{\mathrm{p}} = R_{\mathrm{max}}/BW_{\Omega}$.

5.2.4 Demodulation of the FREE offset frequency

In addition to the ω_1^{max}-dependent phase, a constant amount of phase is added to all transverse magnetization components with each increment of the pulse duration ΔT_{p}. This phase modulation is analogous to having a constant offset frequency in the FREE dimension. Thus, to properly position the object in the image, it should be accounted for (demodulated) in reconstruction.

In the analysis to follow, Ω represents any constant offset that occurs, for example due to chemical shift, inhomogeneity of B_0, and/or an applied B_0 gradient. For an HS1 pulse, the phase produced can be decomposed into Ω - and ω_1^{max}-dependent components, [79]

$$\psi_{HS1}\left(\Omega, \omega_1^{\mathrm{max}}\right) = \psi_{HS1,1}(\Omega) + \psi_{HS1,2}\left(\omega_1^{\mathrm{max}}\right). \tag{5.24}$$

Of interest here, the $\underline{\Omega}$-dependence can be approximated by the analytical expression, [79]

$$\psi_{HS1,1}(\Omega) = \frac{AT_p}{\beta} \ln\left(\frac{1}{\sqrt{A^2 - \Omega^2}}\right) - \frac{T_p\Omega}{2\beta} \ln\left(\frac{A+\Omega}{A-\Omega}\right). \tag{5.25}$$

An analysis of Equation 5.25 for $\Omega = 0$ allows for this additional phase modulation to be analytically described for FREE using HS1 pulses. When accounting for the difference between two HS1 pulses in a DSE, the added phase is

$$\Delta\psi_{FREE} = -\frac{A\Delta T_p}{\beta} \ln(A), \tag{5.26}$$

and thus, the constant offset frequency along the FREE dimension is

$$\frac{\Delta\psi_{FREE}}{\Delta T_p} = -\frac{A}{\beta} \ln(A) \tag{5.27}$$

For the case of HSn with $n > 1$, the offset frequency must be determined empirically by varying its value until the object is centered along the FREE spatial dimension.

5.3 Methods

5.3.1 Simulations

A MatLab- (MathWorks, Natick, MA, version R2019a) and C + +-based Bloch simulator was created to simulate the FREE experiment for a 1D object defined by the middle slice of the Shepp-Logan phantom [80]. The simulation assumed a linear B_1 profile of the coil; 2000 isochromats across space; and a perfect $\pi/2$ excitation, which can be produced with an adiabatic half passage or a square pulse that is transmitted with a separate coil producing a uniform B_1 field. HS1 pulses with $BW_\Omega = 5$ kHz were utilized as the refocusing pulses. To visualize distortions, the spatially varying fractional pixel error ($\Delta x_{\text{error}}(r)$) was calculated and plotted alongside reconstructions, where

$$\Delta x_{\text{error}}(r) = \frac{\Delta x_{\text{actual}}(r) - \Delta x_{\text{predicted}}(r)}{\Delta x_{\text{predicted}}(r)}, \tag{5.28}$$

and $\Delta x_{\text{predicted}}(r)$ is the predicted pixel size based on $k_{\max}$ for a $10 - \text{cm}$ FOV, whereas $\Delta x_{\text{actual}}(r)$ is the distorted pixel size at each point in space. The fractional pixel error shown is the common error seen between reconstructions. One dimensional reconstruction with two different spatial resolutions ($m = 64$ and 128) were considered. Separate simulations were performed with $\omega_1^{\max}(r_{\max}) - \omega_1^{\max}(r_{\min}) = 5$ kHz and 14 kHz, respectively. In addition, with these same B_1 field settings, the simulations investigated the effect of a relatively large resonance offset in the Larmor dimension ($\Omega = \pm 1.5$ kHz) that is constant across space. Reconstructions for all simulations were performed using a fast Fourier transformation.

5.3.2 Experiments

Data were acquired with a flexible CIERMag digital MR spectrometer [81] configured for two transmit (Tx) and receive channels. Each Tx channel is capable of performing AM modulation in a 4-quadrants approach, with amplitude dynamics of 16 bits, along with FM (24 bits- 0.373 Hz resolution) and phase-modulated (14 bits- 0.088° resolution) capabilities. This digital MR spectrometer was interfaced to a $1.5\ \mathrm{T}, 90 - \mathrm{cm}$ magnet (Oxford Magnet Technology, Oxfordshire, UK) with a clinical gradient system (model SC72, Siemens, Erlangen, Germany), using the software created and controlled by Python MR framework, using Python v3.8, [48], [82] a specialized integrated development environment for creating MR sequences, [47], [48] and Tomografo de Ressonância Magnética-Console [47], [48]. The magnet was designed to operate at 4 T but was ramped down to 1.5 T without adjusting the passive shims, leaving a relatively nonuniform B_0. A single-loop elliptical coil with a major axis diameter of 9.65 cm and a minor axis diameter of 9.55 cm was utilized for RF transmission and reception in all experiments. This elliptical coil provided the approximately linear B_1 profile for encoding and a spatially varying excitation flip angle. Padding (2.5 cm thickness) was placed between the coil loop and the subject's head. From a set of images acquired with incrementally increased excitation pulse power, it was determined that $\omega_1^{\max}/2\pi$ of ~ 3.5 kHz could be attained readily at the posterior edge of the brain.

An optimized multi-shot FREE double spin-echo sequence was utilized with HS8 pulses (Figure 5.5). R values were incremented from $R_{\min} = 20$, with $\Delta R = 0.47$, to $R_{\max} = 35$. All pulses had a BW_{Ω} of 2.9 kHz. The FOV was set to 10 cm by appropriately selecting the ΔR value given the B_1 field map used (Equation 5.21). During imaging, the B_0 gradient along the y-direction (G_{y}) was unused; instead, phase encoding was done with the B_1 gradient of the surface coil. To estimate the spatial variation of Δk using Equation 5.20, a Biot-Savart calculation of the relative $B_1(r)$ of the elliptical coil was performed.

For comparison with FREE, a conventional DSE image was acquired using phase encoding and AFP pulses having a fixed R value of 20. Both DSE and FREE utilized a 2-ms sinc pulse (5 lobes) to select a $5 - \mathrm{mm}$ axial slice, repetition time of 3 s, and a echo time (TE) of 61 ms. The images had a matrix size of 64 (phase encodes) by 128 (readout) with a FOV of 10 cm. No additional filtering was done to the sampled k-space. A protocol approved by the institution's institutional review board for imaging of healthy volunteers was followed, including obtaining written informed consent.

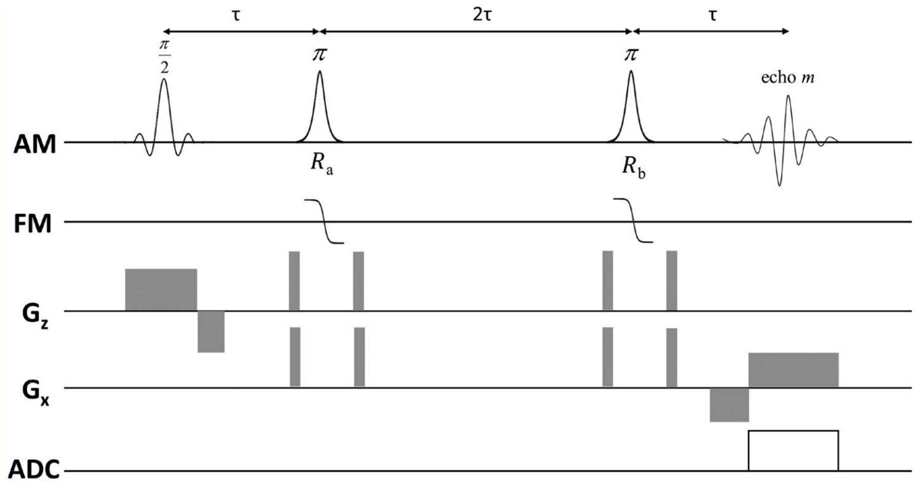

Fig. 5.5. Pulse sequence used to acquire experimental FREE data. Shown is 1 shot of the double-spin echo sequence used to generate a 64 × 128 image. No gradients are utilized in the y-direction; instead, FREE phase encoding is done through the modulation of the difference in the time-bandwidth products (R_a and R_b) of the AFPs in multiple shots. m, echo number (A)

5.4 Results

5.4.1 Simulations

A comparison across different B_1 field settings (Figure 5.6) reveals the benefit of using the maximum available B_1 values to minimize distortions due to the breakdown of the linearity approximation. Although both cases demonstrate accurate reconstruction of the object shape, the smaller B_1 gradient shows greatest image distortion. From a comparison of reconstructions using 64 versus 128 echoes, the results are unchanged except for an expected increase in resolution with $m = 128$.

When a constant resonance offset is applied across space, the object shifts to the right with no noticeable difference in the object shape (Figure 5.6). With the larger B_1 values (Figure 5.6), the amount of shift is significantly reduced. In principle, such shifts can be removed by performing demodulation with a linear phase ramp.

When compared with HS1 pulses, HSn pulses having a large flattening factor ($n = 8$) led to the same reconstructions, with the advantage of allowing smaller values

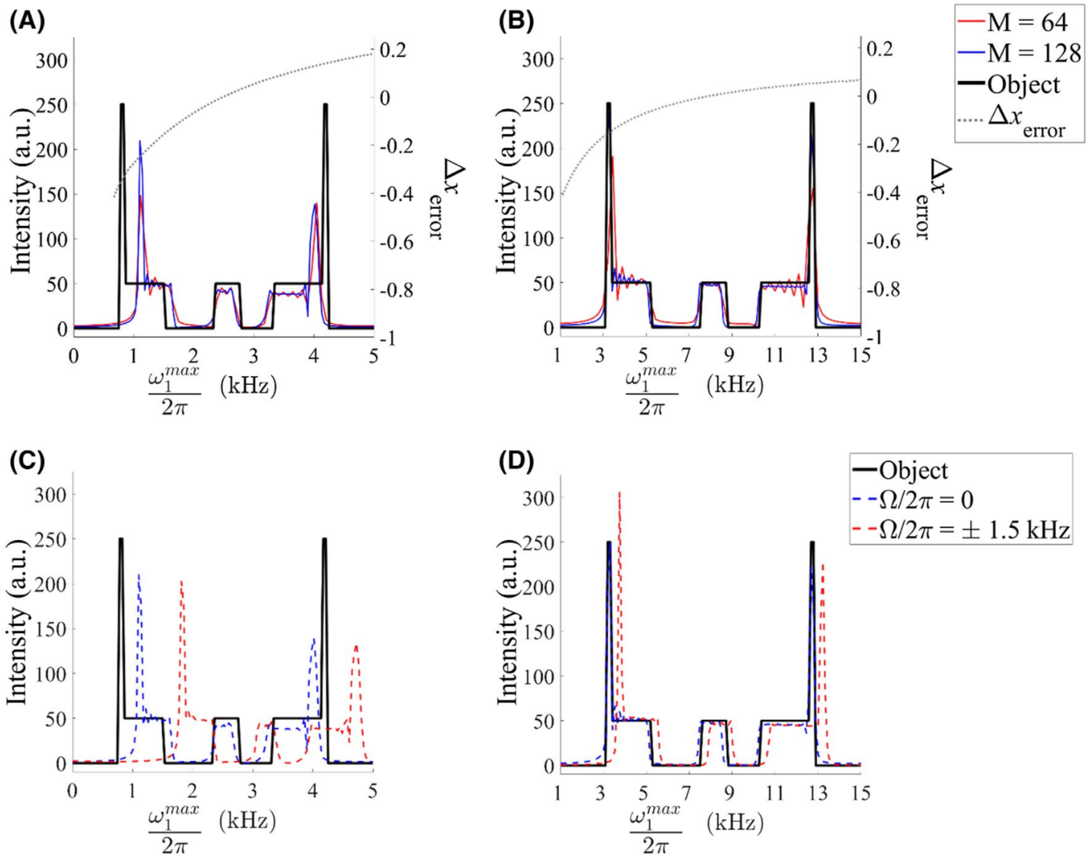

Fig. 5.6. Simulation results for a 1D FREE experiment using HS1 pulses and a linear B_1 gradient. The profile of the 1D object corresponds to the middle slice of the Shepp-Logan phantom. (A and B) Reconstructions are shown for a $\omega_1^{\max}$ range of 5 kHz (A) and 14 kHz (B), using 2 different resolutions, $M = 64$ and 128 . From these results, it can be seen that distortions are greatest when using low B_1 values, but the overall shape of the object remains relatively unchanged. (C) Simulation using a $\omega_1^{\max}$ range of 5 kHz in the presence of a resonance offset ($\Omega/2\pi = \pm 1.5$ kHz) with $M = 128$. (D) Same as C, except with a $\omega_1^{\max}$ range of 14 kHz. These results reveal minimal distortion to the shape of the object in the presence of resonance offset, but the object shifts in position by an amount that increases as the B_1 values decrease. In (A) and (C), $\Delta R = 4.07$, whereas in (B) and (D), $\Delta R = 1.46$. In (A), R-parameters for the 64-point reconstruction are: $R_{\min} = 19.6$, $R_{\max} = 150.R$-parameters for the $M = 128$ reconstruction are: $R_{\min} = 14.3, R_{\max} = 275$. In (B), R-parameters for the 64-point reconstruction are: $R_{\min} = 15.9, R_{\max} = 62.5$. The R-parameters for the 128 -point reconstruction are: $R_{\min} = 19.4, R_{\max} = 112.5$. In (C), the same R-parameters were utilized as in the $M = 128$ reconstruction in (A). In (D), the same R-parameters were utilized as in the $M = 128$ reconstruction in (B).

of R and T_p to be used. When compared to HS1 pulses, HS8 pulses allowed for a reduction in pulse lengths by one third and were thus utilized experimentally.

5.4.2 Experiments

Images obtained from an axial slice through the visual cortex of a human brain are shown in Figure 5.7. To acquire the FREE image (Figure 5.7), the B_1 gradient of the surface coil was used for spatial encoding along the y-direction, whereas the B_0 gradient along the y-direction was unused. The measured average RF power delivered to the surface coil over a 5 -min period was ~ 3.6 W. In contrast to the FREE simulations, which assumed perfect $\pi/2$ excitation, the FREE experiments were performed with a slice-selective (sinc) pulse transmitted with the surface coil, and as such, produced a spatially varying flip angle. Despite using a variable flip angle excitation, no related image artifacts were apparent. A comparison with the conventional DSE image obtained with standard phase encoding along the y-direction (Figure 5.7) reveals the distortion due the nonlinear B_1 gradient of the surface coil in FREE (Figure 5.7). Distortion-correction algorithms known in MRI are expected to be applicable toward FREE given the conceptual equivalency between FREE and phase encoding. Regardless, Figure 5.7 demonstrates successful phase encoding along the y-direction using FREE. As expected, in regions where the B_1 gradient was steepest, the FREE image (Figure 5.7) appears to capture finer brain structures than the conventional phase-encoded image (Figure 5.7). A third phase-encoded image was acquired to generate a qualitative B_1 map (Figure 5.7), from which the RF amplitude was estimated by counting the bands in the image produced by purposefully overflipping magnetization during excitation. Figure 5.7 shows the spatially dependent Δk that occurs due to the nonlinear spatial dependence of $B_1(r)$. This variation in Δk, which at some locations is greater than the Δk of conventional phase encoding, explains the increased resolution seen in some regions of the FREE image.

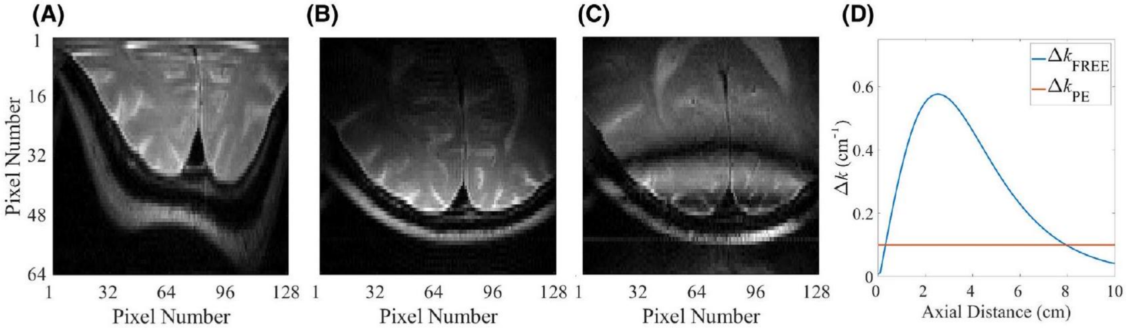

Fig. 5.7. FREE and conventional MRI phase encoding were compared through imaging the back of a participant's head using a surface transceiver coil. Traditional frequency-encoding encoded the x-direction in all images. (A) FREE phase encoding was performed in the y-direction. An optimized FREE double spin echo train multi-shot sequence was utilized for phase encoding and reconstruction was done through the Fourier transformation. (B) Standard MRI phase encoding using a double spin echo sequence. (C) Same as B, except the RF power used for the sinc excitation pulse was increased to that used for the HS8 pulses to allow a rough estimate of the spatial variation of RF amplitude, $\omega_1^{\max}$. (D) Comparison between the spatially varying Δk from FREE, which results from utilizing the nonlinear encoding field of the surface coil and the Δk from a conventional phase encoding system set to a FOV of 10 cm. The spatial variation of Δk shown begins at the coil and extend axially through the center of the coil map. The large variations of Δk leads to the distortions seen in the FREE reconstruction in (A)

5.5 Discussion

Here, a new imaging method that eliminated one B_0 gradient coil along the phase encoding direction was introduced. This multi-shot double spin-echo FREE sequence utilizes the adiabatic condition to attain high immunity to nonuniform B_0 up to the bandwidth of the pulse. If greater resistance to resonance offsets is needed, the bandwidth of the pulses can be increased (e.g., by using larger R values), which will make FREE extremely robust to the expected B_0 inhomogeneity in lower-cost magnet systems. Previous RFI approaches fall short in the presence of large resonance offsets [65], [71], [77] With conventional AM pulses, resonance offset has the effect of tilting $\mathbf{B}_{\text{eff}}$ out of the transverse plane; as a result, the ability to effectively rotate magnetization diminishes as the pulse duration increases. The MRI signal in FREE does not suffer this consequence.

As was the intent of these first experiments, FREE was able to image the human visual cortex without using a B_0 gradient in the y-direction. Phase encoding was done only with the modulation of RF pulses using a simple single loop coil placed on the back of the subject's head. These experimental results effectively show that the phase encoding traditionally done by B_0 gradient coils can be accomplished with a simple B_1-gradient coil. The FREE sequence and experimental results presented here should be seen as a starting point [83]. FREE is not limited to using pulses in the HSn family only. FREE's compatibility with other AFP pulses (i.e., chirp) has not been investigated, although substantial benefits may be possible.

FREE was performed by holding BW_Ω of the pulses constant while changing the length of one of the pulses in a DSE sequence. By using a B_1 gradient and two AFPs with different pulse lengths, transverse magnetization phase can then encode spatial information. Other RFI methods do not utilize FM pulses, and with solely AM pulses, changing the length of the pulse also changes BW_Ω of the pulse. This has the effect of producing variable phase encoding for different isochromats. FREE does not have this issue because holding the BW_Ω constant enables uniform phase encoding for all isochromats.

In FREE, nonlinearity in the spatial profile of the surface coil B_1 caused image distortion and a mismatch between the expected and actual FOV. Such B_1 nonlinearity is the reason local gradients vary over space, creating variable pixel sizes. In the reconstructed image, the variable pixel sizes had a compensatory effect on the loss of signal over space, as explained in the following. With regular (non-FREE) DSE using a surface transceiver coil, pixels originating from increasing distances from the coil have pixels with decreasing signal intensity, creating a shading effect in images. In the FREE image, the pixels tend to increase in size with distance from the coil and thus contain increasing numbers of spins. As such, although FREE's images seem to lack the shading effect present in the regular DSE image, stretching and compression distortions persist in the image. In setting the FOV, there is no guarantee that the sum of the variable pixel sizes over space is equivalent to the intended FOV due to the nonlinearities present in the encoding field. To appropriately set the FOV, a bijective mapping must exist between the nonlinear B_1 coil map and the distorted image [84].

A benefit of utilizing nonlinear encoding fields is the capability to set the FOV to match a portion of the B_1 map where the B_1 gradient is steepest. This effectively allows high-resolution imaging of a portion of the object within an area smaller than the FOV, which can be set to a higher resolution than the rest of the object. In a demonstration of this, finer structures in the visual cortex were more apparent in FREE's reconstruction when compared to conventional phase encoding. With the aforementioned mismatch in FOV and the nonlinearity of the B_1 coil map used, which were not accounted for in the derivation, spatial variation of Δk (and resolution across the object) was anticipated. As expected, the varying spatial resolution produced by $B_1(r)$ of a surface coil resembles the spatial encoding previously shown using nonlinear B_0 gradients [85].

The process by which FREE encodes spatial information is equivalent to conventional phase encoding; thus, many of the approaches already available to MRI for distortion-correction, parameter optimization, and post-processing can be reasonably applied here to tackle the fractional pixel distortion seen at lower B_1 values [67], [84], [86], [87]. Although for some applications FREE may be limited by the linearity of $B_1(r)$, this limitation might be overcome in the future. Currently, to maximize reconstruction quality, RF coils producing a nearly linear B_1 gradient should be used.

Because a DSE sequence with relatively long TE was utilized, T_2 relaxation provided the dominant source of contrast. In the present DSE implementation, the minimum TE was by necessity long; as such, the method is currently not suited to provide T_1 contrast. However, diffusion weighting can be generated simply by including diffusion weighting gradients in the echo delays. Likewise, T_2^* contrast can be generated by displacing the center of the acquisition away from the center of the spin echo created by the second AFP pulse. For FREE, there are two main requirements: the use of FM functions and an approximately linearly varying B_1 map. In experiments, the same RF coil having a nonlinear B_1 profile was utilized both for excitation and AFP encoding. Thus, the sinc excitation pulse produced a spatially varying initial transverse magnetization. This problem might be overcome in the future by using RF coil arrays together with multichannel Tx, whereby excitation is performed in a homogenous Tx mode and spatial encoding uses a spatially varying Tx mode.

The work herein demonstrates a Cartesian sampling approach through a multi-shot sequence where only one point of k-space is acquired per shot. Drawbacks of the current FREE implementation stems from the need for two AFP pulses to modulate the phase of the double spin-echo signal and the need to increase the difference in R value of the two AFP pulses. The latter leads to relatively long pulses and TE. Future work will likely show that multi-echo, single-shot or segmented implementations of FREE are possible, whereby each AFP in the train adds k-space encoding. Single-shot or segmented approaches will allow AFP pulses having a constant R value to incrementally add k-space encoding. In this manner, the AFPs can be synthesized using a low, constant R value that will permit short refocusing pulse length similar to that used in other multi-echo MRI sequences, keeping pulses short and reducing long TE times.

As with all multi-echo sequences, concerns of specific absorption rate are valid for higher B_0 fields, but the expected application of FREE is in the development of lower cost and more accessible systems, which are unlikely to use high field magnets. Low-cost systems are envisioned to operate at low field (0.1 T $-$ 1.5 T) or ultralow field ($< 0.1\ T$). At these field strengths, specific absorption rate concerns will be reduced, and thus the use of larger B_1 bandwidths should be possible, although there is a lower limit to Δk that coincides with the technical limitations of a B_1 coil (e.g., the gradient cannot be made to be infinitely large). We expect future developments of optimized FREE sequences for low field systems that can be performed within safe specific absorption rate limits. At these lower fields, Biot-Savart simulations might adequately estimate B_1 profiles for the purposes of correcting image distortions due to variable resolution (i.e., no need to use Maxwell equations).

The successful phase encoding performed herein demonstrates the technical feasibility of FREE as an RFI approach. Through further developments (e.g., single-shot and segmented multi-echo versions of the sequence) combined with parallel imaging acceleration, 2D FREE acquisitions with orthogonal B_1-gradient coils should be feasible in a reasonable scan time. The realization of full 3D RFI will likely require the development of frequency encoding using a B_1 gradient instead of a B_0 gradient, which will be challenging. Alternatively, because FREE is highly tolerant to resonance offset, frequency encoding might be performed without any B_0-gradient hardware simply by designing a static B_0 gradient into the magnet itself and/or the passive shims.

5.6 Conclusion

The interest in the development of low-cost, portable MRI systems is expected to increase with time, as noted by the increased frequency of published articles on this topic [1], [3], [88]. Techniques and methods optimized for low-cost systems are required to accomplish the goal of a truly low-cost, accessible system that produces high-quality images. FREE looks to make progress in removing the need for B_0-gradient coils in systems and is optimized to perform best at the expected field strengths of portable systems (≤ 1.5 T).

Chapter 6

Frequency-Encoding Frequency-modulated Rabi Encoded Echoes

6.1 Introduction

The high cost of MRI systems relegates its clinical impact to the world's wealthiest communities, and the status quo of MRI remains incompatible with most of the world's population. MRI is too valuable of an approach to be limited; a global need exists to develop greener, cheaper, and smaller MRI systems [1]. B_1 imaging could cut the cost, complexity, and infrastructure demands of an MRI system by removing or reducing the need for B_0 gradient coils. B_1 imaging was first developed with Rotating Frame Zeugmatography [65], but was never adopted due to sensitivity to B_0 off-resonance [71] and slow imaging. A resurgence of B_1 encoding techniques have emerged [68], [83], [89]. In particular, phase-encoding frequency modulated Rabi encoded echo (PE-FREE) [83] is a B_1 imaging approach capable of imaging in highly inhomogeneous B_0 and B_1 fields.

Despite the potential of these B_1 imaging approaches, most are phase-encoding techniques or sensitive to B_0 off-resonance. Phase-encoding limits the speed of acquisition and sensitivity to off resonance limits magnet design. Here, we present

PE-FREE's counterpart: Frequency-encoding FREE (FE-FREE). FE-FREE utilizes nearly simultaneous transmit and receive, AFPs, and B_1 field gradients to acquire one line of k-space per experiment. With this new pulse sequence, we generate rotary echoes with no B_0 gradient coils and image in inhomogeneous B_0 fields. FE-FREE brings us one-step closer to developing a new class of MRI systems with no B_0 gradient coils.

6.2 Theory

6.2.1 Background:

Adiabatic full passages (AFPs) uniformly invert spins across inhomogeneous $\omega_0 = -\gamma B_0$ and $\omega_1 = -\gamma B_1$ fields [22]. AFPs are defined by their amplitude- and frequency- modulation ($AM(t)$ and $FM(t)$) functions and their subsequent time-bandwidth product, $R = T_\text{p} \cdot BW$. T_p is the length of the pulse, and BW is the bandwidth of the FM pulse. In an AFP, the $AM(t)$ and $FM(t)$ respectively modulate the pulse amplitude, ω_1, and transmit frequency, ω_RF. ω_RF modulates about a carrier frequency, ω_c, typically set to the center frequency of interest.

During an AFP, $AM(t)$ and $FM(t)$ define a field in the $\mathbf{x'}$ and $\mathbf{z'}$ direction:

$$\omega_1(t) = -\gamma B_1(t)\hat{\mathbf{x}}' \tag{6.1}$$

$$\Delta\omega(t) = (\omega_\text{c} - \omega_\text{RF}(t))\,\hat{\mathbf{z}}'. \tag{6.2}$$

Their vector sum defines the effective nutation frequency and rotating field during the AFP, ω_eff :

$$\widehat{\omega}_\text{eff}\,(t) = \omega_1(t)\widehat{\mathbf{x}'} + \Delta\omega(t)\widehat{\mathbf{z}'}. \tag{6.3}$$

$\widehat{\omega}_\text{eff}\,(t)$ sweeps from the +z to the −z axis at an angular velocity defined by $\alpha(t)$:

$$\alpha(t) = \arctan\left[\frac{\omega_1(t)}{\Delta\omega(t)}\right] \tag{6.4}$$

The adiabatic condition states that if

$$|\omega_{\text{eff}}\,(t)| \gg |d\alpha/dt| \tag{6.5}$$

spins that begin co-linear or perpendicular with $\widehat{\omega}_{\text{eff}}\,(t)$ remain approximately so while $\widehat{\omega}_{\text{eff}}\,(t)$ sweeps. The adiabatic condition enables a uniform inversion in highly inhomogeneous B_0 and B_1 fields[22]. For this iteration of FE-FREE, we utilize pulses that satisfy the adiabatic condition.

Hyperbolic Secants (HS) are a popular family of FM pulses that smoothly invert spins [24] within the pulse BW. The $AM(t)$ and $FM(t)$ of an HSn pulse are written as:

$$\omega_1(t) = \omega_1^{\max} \operatorname{sech}\left(\beta\left(\frac{2t}{T_{\text{p}}} - 1\right)^n\right) \text{ and} \tag{6.6}$$

$$\omega_{\text{RF}}(t) = \omega_{\text{c}} + \int_0^t A \operatorname{sech}^2\left(\beta\left(\frac{2v}{T_{\text{p}}} - 1\right)^n\right) dv. \tag{6.7}$$

Where ${\omega_1}^{\max}$ is the peak ω_1 during the pulse; β is the truncation factor; n is the pulse order; v is a dummy integration variable; and $A = BW/2$.

6.2.2 Spatial encoding with AFPs:

An AFP inverts and leaves spins with an approximately linear B_1 dependent spatial phase, [78], [83] (Figure 6.1).

FREE imaging precisely controls $\psi(y)$ to spatially encode with B_1 fields. In its phase-encoded form, a spatially varying $B_1(y)$ transmits two AFPs in a double-spin echo pulse sequence with a time-bandwidth difference (ΔR). A ΔR difference creates a residual B_1-phase that is used for phase-encoding. ΔR is stepped to produce phase encoding in a multi-shot or echo-train approach [73], [83]. In FE-FREE, following an excitation pulse, a spatially varying $B_1(y)$ transmits two AFPs sequentially. The first and second AFP respectively add and unwind a phase proportional to their respective R-value. We describe this in detail below.

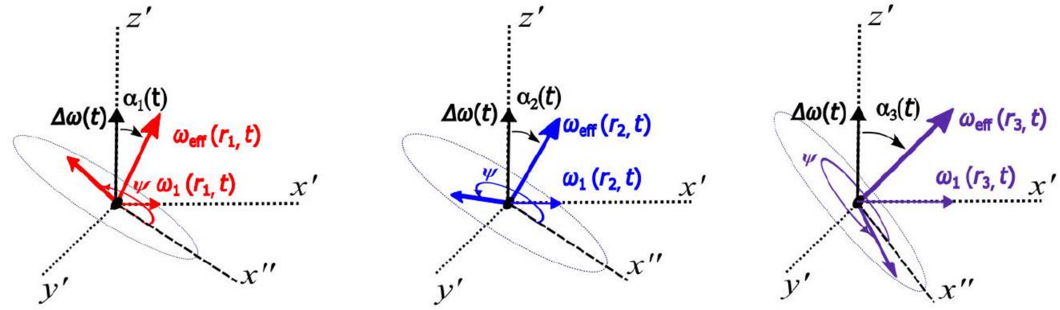

Fig. 6.1. This figure demonstrates the phase accrual of different spins in a B_1 gradient during the transmission of an FM pulse. The ω_{eff} trajectory, during the pulse, is shown for three different spatial locations, r_1, r_2, r_3. Across a B_1 field, the FM component $(\Delta\omega(t))$ remains constant, while the amplitude modulated component $(\omega_1(r_{\text{n}}, t))$ varies with the amplitude of the RF transmission field. If the adiabatic condition is held, the spins remain approximately perpendicular to their respective ω_{eff} fields and accrue a B_1-dependent phase throughout the pulse, $\psi(t).\psi(t)$ is B_1-dependent, and thus spatially dependent, and used for encoding in FREE pulse sequences.

6.2.3 Signal-equation and k-space description of FE-FREE:

The accrual of phase occurs at a rate defined by

$$\psi(t) = \int_0^t \omega_{\text{eff}}(t')\,dt', t \in [0, T_{\text{p}}]\,. \tag{6.8}$$

When using a spatially-varying RF field, $\psi(t)$ and $\omega_{\text{eff}}(t)$ become spatially dependent:

$$\psi(t, y) = \int_0^t \omega_{\text{eff}}\ (t', y)\,dt',\ \text{where } t \in [0, T_{\text{p}}]\ \text{and } y \in [0, FOV_{\text{y}}] \tag{6.9}$$

FOV_{y} defines the spatial length of the B_1 field. The signal equation during an AFP is defined as:

$$s(t) = \int_0^{FOV_{\text{y}}} M_{\text{xy}}(t, y)\exp(-i\psi(t, y))dy \tag{6.10}$$

where M_{xy} is the detectable transverse magnetization. The first and second AFP of FE-FREE (Fig. 6.2) create an approximately linear phase defined by:

$$\psi_{\text{dp}}(t, y) = \int_0^t \omega_{\text{eff}}(t', y)\,dt',\ \text{where } t \in \left[0, T_{\text{p}}^{\text{dp}}\right], y \in [0, FOV_y]\ \text{and} \tag{6.11}$$

$$\psi_{\mathrm{ro}}(t,y)=\int_0^t \omega_{\mathrm{eff}}\left(t',y\right)dt',\ \text{where } t\in\left[0,T_{\mathrm{p}}^{\mathrm{ro}}\right],\ \text{and } y\in\left[0,FOV_y\right] \tag{6.12}$$

$T_{\mathrm{p}}^{\mathrm{dp}}$ and $T_{\mathrm{p}}^{\mathrm{ro}}$ define the pulse lengths of the first and second pulse (dp = dephase, ro = readout).

The k-space trajectory of FE-FREE during the second AFP is defined as

$$k(t)=\frac{d\psi_{\mathrm{dp}}\left(T_{\mathrm{p}}^{\mathrm{dp}},y\right)}{dy}-\frac{d\psi_{\mathrm{ro}}(t,y)}{dy},\ \text{where } t\in\left[0,T_{\mathrm{p}}^{\mathrm{ro}}\right]. \tag{6.13}$$

$k_{\max}$ is defined as

$$k_{\max}=\frac{d\psi_{\mathrm{dp}}\left(T_{\mathrm{p}}^{\mathrm{dp}},y\right)}{dy}-\frac{d\psi_{\mathrm{ro}}\left(T_{\mathrm{p}}^{\mathrm{ro}},y\right)}{dy}. \tag{6.14}$$

To create a rotary echo centered in the second pulse, and thus frequency encoding, ψ_{ro} must be twice that of ψ_{dp}. According to Eq. 6.13, multiple approaches may accomplish this. The simplest approach is doubling the length of the second pulse $\left({T_{\mathrm{p}}}^{\mathrm{ro}}=2{T_{\mathrm{p}}}^{\mathrm{dp}}\right)$ while holding all other pulse parameters constant. This condition creates a rotary echo centered at the second pulse and a symmetric k-space trajectory [90]. The spatial resolution of a symmetric k-space trajectory is defined as:

$$\Delta y=\frac{1}{2\mathrm{k}_{\max}}. \tag{6.15}$$

From resolution, $FOV_{\mathrm{y,}}$ is defined

$$FOV_{\mathrm{y}}=N_{\mathrm{ro}}\cdot\Delta y=N_{\mathrm{ro}}\left(\frac{1}{2\mathrm{k}_{\max}}\right), \tag{6.16}$$

where N_{ro} is the number of points acquired. Δk is dependent on our pulse selection and sampling protocol.

6.2.4 Gapped Acquisition and Δk :

Similar to Sweep Imaging with Fourier Transformation (SWIFT) [91], we repeatedly turn on and off the transmitter during the second AFP of FE-FREE to sample "during" the pulse. The first and second pulses are turned into gapped pulses. Acquisition is done during the gaps of the second pulse, and the first pulse is also gapped

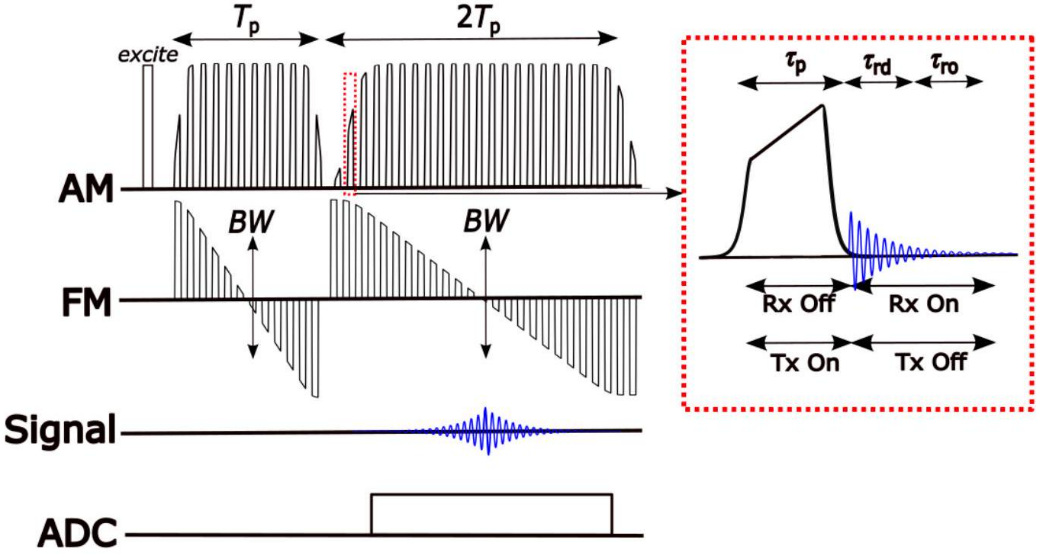

Fig. 6.2. Pulse sequence used to frequency encode with B_1 gradients. A rotary echo is created by setting the time-bandwidth product of R_{ro} to twice that of R_{dp}. The rotary echo is centered during R_{ro} and gaps of length $\tau_{\mathrm{rd}} + \tau_{\mathrm{ro}}$ are inserted between pulse segments of length τ_{p}. To reduce ringdown, the pulse segments are defined by a waveform that smoothly brings the transmit amplitude to zero. Data from τ_{rd} is avoided due to coil ring-down and data from τ_{ro} is used to reconstruct the object. The pulses are run sequentially similiarily to a GRE, but no B_0 gradients are used.

to keep the refocusing condition, outlined in Eq. 6.13. During the gap, the pulse is split into segments encompassing three time periods: the pulse segment, τ_{p}, a delay to avoid ring-down, τ_{rd}, and a readout period, τ_{ro}. To reduce ringdown, we define the pulse segments (τ_{p}) according to a waveform that smoothly brings the transmitter amplitude to zero. The pulse is redefined to:

$$AM_{\Pi}(t) = AM(t) \cdot [\Pi_{\mathrm{n}}(t - ndw) * x(t)] \tag{6.17}$$

Π_n defines a comb function, $x(t)$ the pulse segment, $AM(t)$ the parent AM pulse, and dw the spacing of the pulse segments (Fig. 6.2).

τ_{p} and $\psi(t, y)$ define the $\Delta k(t)$ during our readout pulse:

$$\Delta k(t) = \frac{d\psi_{\mathrm{ro}}(t, y)}{dy}, \text{ where } t \in \left[0, T_{\mathrm{p}}^{\mathrm{ro}}\right] \tag{6.18}$$

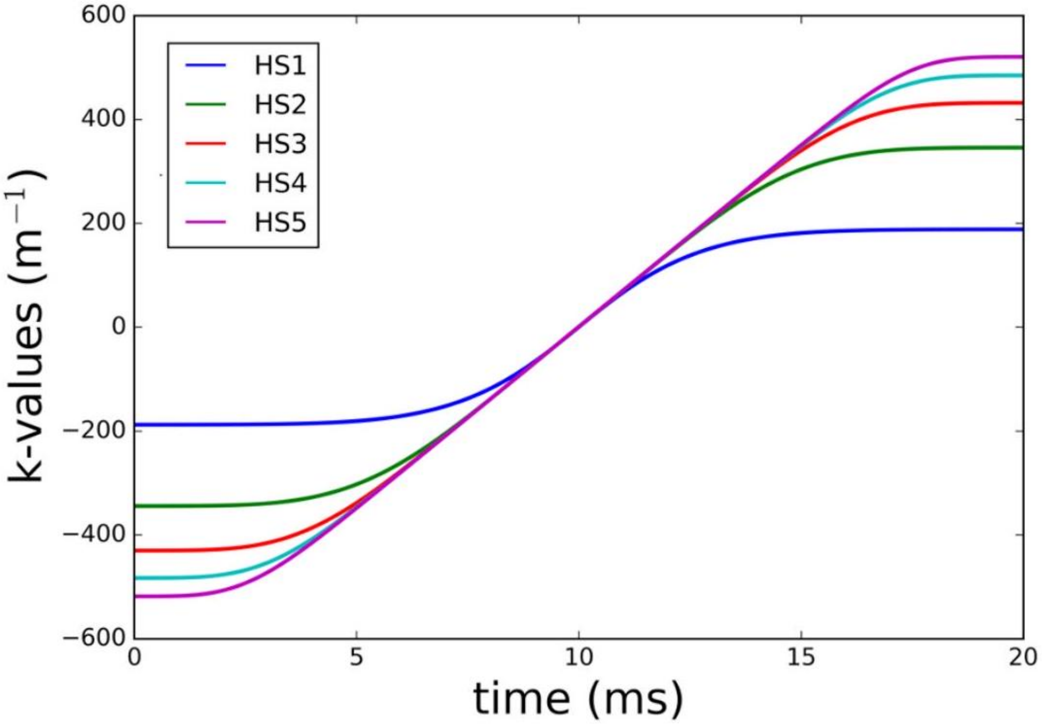

Fig. 6.3. The calculated k-space trajectory for an HS1, HS2, HS3, HS4, and HS5 pulse when used as a refocusing pulse in FE-FREE. The k-space trajectory is calculated using Eq. 6.13. The first and second AFP had a time-bandwidth product of $2,000$ Hz $\cdot\, 0.02$ s and $2,000$ Hz $\cdot\, 0.04$ s respectively. The pulses were transmitted with a linear $\gamma B_1/2\pi$ gradient of 7 kHz $\cdot$ (10 cm)$^{-1}$ with a peak $\gamma B_1/2\pi$ of 10 kHz.Δk and $k_{\max}$ varied according to the order of the pulse. Higher-order HS pulses covered more of k-space and had a larger linear Δk region.

Eq. 6.18 depends on the pulse segment lengths, τ_{p}, between acquisition gaps and the pulse type. Despite uniform sampling in time, Eq. 6.18 demonstrates a nonuniform k-space trajectory and differing $\mathrm{k}_{\max}$ values across different HS pulses (Fig. 6.3).

Non-linearities in our spatial frequencies arise from the spins' nutation frequency, $\omega_{\mathrm{eff}}(t)$. Eq. 6.3 shows when A is the peak Rabi frequency during $\omega_{\mathrm{eff}}\,(t)$, the spins reach their peak Rabi frequency of A and eventually settle at the spatially-dependent ${\omega_1}^{\max}$. This settling time largely depends on pulse parameters and can create nonlinearities in $\omega_{\mathrm{eff}}(t)$ and Δk(t). Selecting A values approximately equal to the weakest $\gamma B_1(y)$ avoids nonlinearities (Fig. 6.4) and holds positions in space at a constant spa-

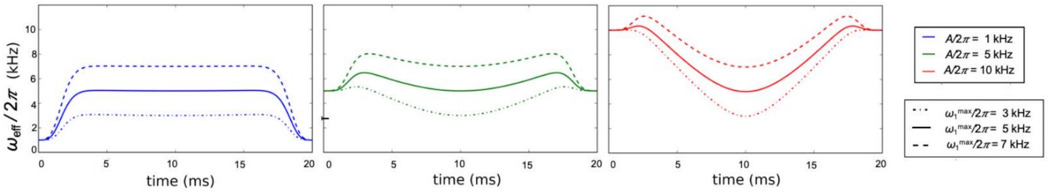

Fig. 6.4. The spins' effective nutation frequency during an AFP are plotted. All pulses used an HS10 with a $T_{\text{p}} = 20$ ms, and the $\omega_{\text{eff}}(t)/2\pi$ was calculated for three $A/2\pi$ values $= 1, 5,$ and 10 kHz and three $\omega_1^{\text{max}}/2\pi$ values $= 3, 5,$ and 7 kHz. To permit a Fourier reconstruction, the effective spatial frequency must remain constant during the acquisition. These calculations show variations in the spins' nutation frequency despite a constant ω_1^{max} frequency for AFPs with a large bandwidth. Data acquired from higher bandwidth pulses require a non-Fourier reconstruction.

tial frequency during periods of acquisition - important to a Fourier reconstruction.

Assuming a linear B_1 field gradient, a small A value, and a constant $\Delta k(t)$, the analytical form of Δk is:

$$\Delta k = \frac{(\psi_{\text{max}} - \psi_{\text{min}})}{\Delta r}, \tag{6.19}$$

where ψ_{max} and ψ_{min} is the phase at the strongest and weakest $B_1(y)$ field values and Δr is the spatial extent of the coil.

6.2.5 Spin-locked magnetization during the ω_{eff} trajectory

During FE-FREE, residual z-magnetization spin locks to ω_{eff} during its trajectory. Residual magnetization arises from unexcited magnetization and or imperfect 90-degree pulses (Fig. 6.5). If a spatially varying B_1 field transmits the 90-degree pulse in FE-FREE, residual M_{z} signal across the sample will spin-lock. Spin-locking produces a signal that mirrors the pulse profile. We correlate the data [91] to remove the pulse waveform, which in our case is approximately equal to the spin-locked signal:

$$H(\omega) = \frac{R(\omega)X^*(\omega)}{|X(\omega)|^2} \tag{6.20}$$

$X(\omega)$ and $R(\omega)$ define the pulse and data spectrum. $H(\omega)$ defines the spin-density profile. Figure 6.5 demonstrates the successful removal of the spin-locked component using Eq. 6.20.

Eq. 6.20 assumes that the spin-locked component matches the pulse waveform; an assumption named the spin-locked matching approximation or SMA. This approximation enables the removal of most spin-locked signal from the data (Fig 6.5). Divergences in SMA result in residual magnetization being present post correlation (Fig. 6.5). Divergences can arise from a loss of adiabaticity or variable $\omega_{\text{eff}}(t)$ trajectories. The former is easily understood, while the latter requires an analysis.

To study the accuracy of SMA, a propagator analysis was performed. A propagator matrix (Eq. 6.21) was defined using the formalism from our original phase-encoding FREE paper [83], which inverts spins with perfect adiabaticity.

$$R_{ro}(t) = \begin{bmatrix} \cos(\psi_{dp} - \psi_{ro}(\mathrm{t}))\cos(\Delta\alpha(t)) & -\sin(\psi_{dp} - \psi_{ro}(\mathrm{t}))\cos(\Delta\alpha(t)) & \sin(\Delta\alpha(t)) \\ \sin(\psi_{dp} - \psi_{ro}(\mathrm{t})) & \cos(\psi_{dp} - \psi_{ro}(\mathrm{t})) & 0 \\ \cos(\psi_{dp} - \psi_{ro}(\mathrm{t}))\sin(\Delta\alpha(t)) & \sin(\psi_{dp} - \psi_{ro}(\mathrm{t}))\sin(\Delta\alpha(t)) & \cos(\Delta\alpha(t)) \end{bmatrix} \tag{6.21}$$

$R_{\text{ro}}(t)$ defines a rotation matrix that inverts spins after they have been dephased by an initial dephaser pulse, like in FE-FREE. The rotation is described in the FM frame with $\Delta\alpha$ defining the rotation angle; an AFP sweeps $\Delta\alpha$ from 0 to π. A simulation was performed to study the spin-locked component in different conditions using the propagator. Figure 6.6 shows the effect of keeping the pulse length the same but modulating the bandwidth. Under low bandwidth conditions, the discrepancy between the normalized spin-locked real component and pulse AM profile is minimal. However, as the pulse bandwidth increases, the $\omega_{\text{eff}}(t)$ trajectory, in the FM frame, deviates from the pulse profile. Like the condition observed in Fig. 6.3, a low bandwidth pulse allows SMA to remain valid, facilitating the recovery of the desired data through correlation. Conversely, larger bandwidths reduce SMA's and Eq. 6.21 accuracy in isolating the rotary echo from the spin-locked components.

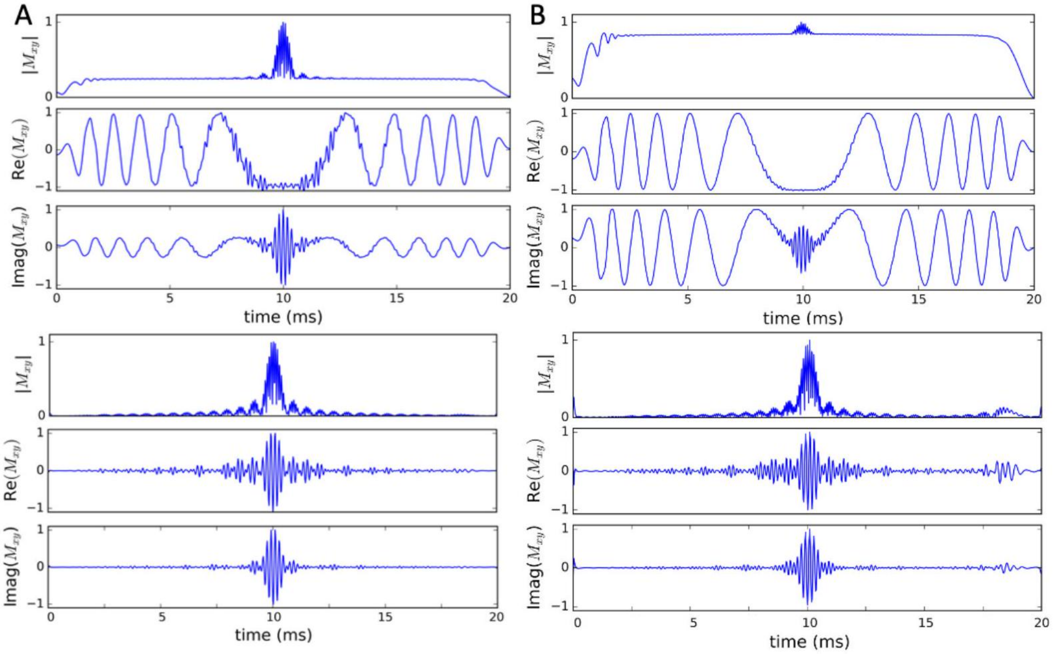

Fig. 6.5. A rotary echo created by FE-FREE was simulated. The rotary echo's magnitude, real, and imaginary components are plotted for two cases: a perfect 90-degree excitation across space (column A) and an imperfect spatial excitation with a B_1 gradient (column B). A 50 μs hard pulse excited the spins in both cases. In the uniform excitation case (left column), a $\gamma B_1/2\pi$ set to 5 kHz achieved a uniform 90-degree flip across space, while in the B_1 gradient case (right column) a B_1 gradient with a minimum and maximum value of 0 and 5 kHz excited spins. The data is acquired in the phase-modulated frame of the pulse. In both cases, spin-locked components are seen that track the waveform of the pulse, but a uniform excitation drastically reduced spin-locking. Correlation was applied to both cases. The bottom row shows the result post-correlation. Correlation extracted the rotary echoes of interest in either case.

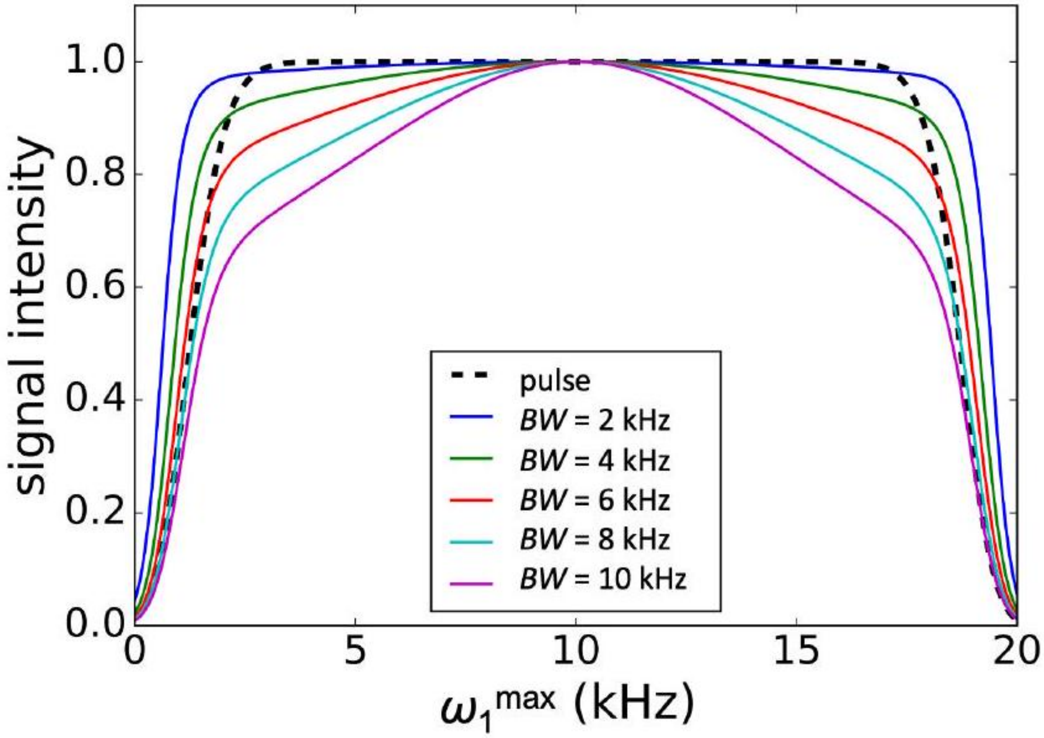

Fig. 6.6. An adiabatic full passage was simulated in the FM frame using a propagator analysis defined in Equation 6.21. The pulse was simulated in inverting spins aligned with the $+z'$ axis. The normalized real component is shown throughout the pulse for different BW values. A B_1 gradient with a bandwidth of 5kHz and a peak amplitude of $\gamma B_1/2\pi = 7$kHz transmitted the pulse. Various conditions were considered, and the results were plotted. In all cases, an HS10 pulse with a duration of 20 ms was utilized. The spins initially aligned with the $+z'$ axis underwent spin locking with the effective field during the inversion. By plotting the real component of the tracked spins, it is evident that at lower bandwidth values, the pulse waveform accurately defines the trajectory of the spin locked component correlation would remove. However, with larger bandwidth values, a notable deviation occurs, rendering the assumption that the spin lock trajectory approximates the pulse waveform inappropriate.

6.3 Methods:

6.3.1 Simulations:

A custom Python Bloch simulator simulated FE-FREE. A γB_1 gradient of $12\ \text{kHz} \cdot (8.5\ \text{cm})^{-1}$ transmitted both AFPs, which were defined by HS10 FM pulses. The time-bandwidth products of the first and second pulse were $0.0125\ \text{s} \cdot 2000\ \text{Hz}$ and $0.025\ \text{s} \cdot 2000\ \text{Hz}$, respectively. $\tau_\text{p} = 31.25\ \mu\text{s}, \tau_\text{ro} = 18.75\ \mu\text{s}$, and one point per gap was collected, resulting in 800 points. The middle 400 points were reconstructed. Reconstructions of the central slice of the Shepp-Logan phantom [80] were evaluated for on- and off resonant cases. Ideal conditions were simulated by assuming a uniform 90-degree excitation, a linear B_1 gradient, no RF coil ringdown, and only M_xy detection. The complex Fourier transformation (FT) reconstructed the object resulting in two copies; one copy is shown in reconstructions. This topic will be further explained in the discussion section.

6.3.2 Experiments:

Magnet and Spectrometer:

Experiments were performed on a 0.5 T Halbach magnet [64] with ±8 kHz of B_0 inhomogeneity across the object. The magnet has a weight of 150 kg, bore of 19 cm, and length of 40 cm. The 0.5 T has no passive shims, Faraday cage, filter panel, or B_0 gradient coils. A heat regulator system, designed by RE magnet studio, kept the magnet's temperature steady at 28^oC, reducing field drift, and a grounding panel reduced RF noise. An active Varian T/R switch, preamplifier (model: 0191432205), and CPC 500W amplifier (model: 9T500M-16C) powered the system. A custom two channel Tx/Rx CIERMag Digital Magnetic Resonance Spectrometer operating at 21.1 MHz [47], [48], [82] deployed the pulse sequence. The receive system has 16 bits of resolution, collecting one data point per microsecond. The DMRS's transmit channels can amplitude modulate in a 4-quadrant approach with 16-bit amplitude dynamics, as well as frequency = (24 bits with 0.373 Hz resolution) and phase modulation (14 bits with 0.022° resolution). A Python MR framework (PyMR) controls the spectrometer. The system is equipped with a development environment

(IDE) specialized for MR sequence design. A custom coding language (F-language) describes the pulse sequences.

Experimental parameters and processing

For FE-FREE, a 10 cm surface coil transmitted a non-linear γB_1 gradient of ~ 2 kHz $\cdot$ (5 cm)$^{-1}$. A 150 μs square pulse excited the spin. The square pulse was calibrated to produce an approximate 90 degree flip at the front of the phantom. HS10 pulses were utilized for both inversion pulses; the first and second time-bandwidth products were 0.010 s $\cdot$ 4,000 Hz and 0.020 s $\cdot$ 4,000 Hz, respectively. $\tau_{\mathrm{p}} = 50$ μs, $\tau_{\mathrm{rd}} = 5$ μs, and $\tau_{\mathrm{ro}} = 45$ μs. The parent pulse was subdivided by pulse segments defined by twenty points (of length τ_{p}), and twenty points were acquired during $\tau_{\mathrm{rd}} + \tau_{\mathrm{ro}}$ by using a Rx bandwidth of ± 200 kHz. The pulse segments were defined with the $AM(t)$ of an HS10 pulse. Data acquired during τ_{rd} was zeroed out. The data was correlated with the pulse waveform and down sampled to one point per gap, resulting in 200 points. We reconstructed the object by applying the Fourier transform to the middle 64 points of the data. A three-chamber saline phantom was imaged (Fig. 6.7).

For PE-FREE, an optimized multi-shot DSE PE-FREE [83] pulse sequence phase encoded with the following parameters: $R_{\mathrm{min}} = 88, R_{\mathrm{max}} = 200, \Delta R = 3.5$, and all pulses had a $BW = 10$ kHz. The same excitation pulse as FE-FREE was used with the same power settings. $TE = 55$ ms$, TR = 9$ s, and 64 points were acquired per echo with a Rx bandwidth of $\pm$15kHz resulting in 128 pts per echo. 5 averages were performed per shot. The 2D Fourier transformation was applied to the NxM dataset, where N is the number of phase encodes, and M the number of points acquired per echo. The reconstruction showed the spin-density profile as a function of space and chemical shift. The same three-chamber saline phantom was imaged for comparison (Fig. 6.7).

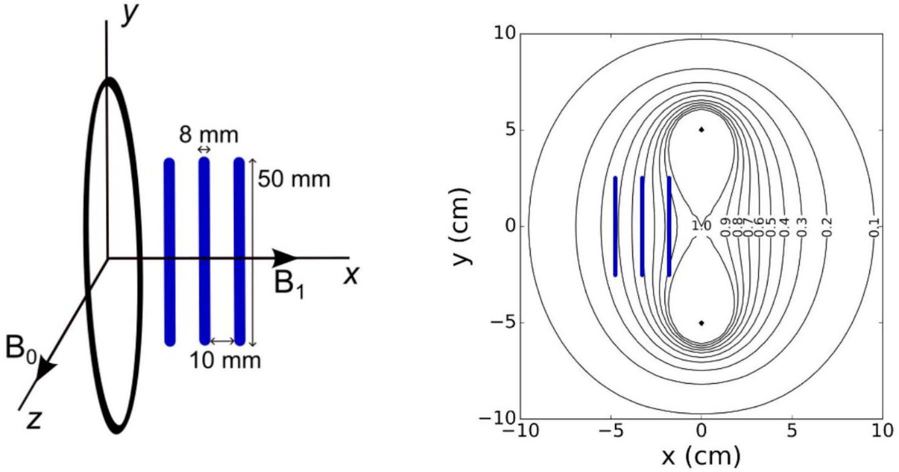

Fig. 6.7. The left panel shows a diagram of the 3-chamber phantom, B_0 field, and B_1 coil. In the Halbach magnet, the B_0 faces in the direction where the y axis typically lies. The three chambers were filled with saline. The right channel shows a contour plot of a normalized Biot-Savart simulation demonstrating the approximate B_1 field maps and their relative location to the 3-chamber phantom.

6.4 Results:

Simulation results showed the ideal settings of a uniform excitation, linear γB_1 field, and no RF ringdown. FE-FREE accurately reconstructed the middle slice of the Shepp-Logan phantom (Fig. 6.8). A constant resonance offset was simulated across space. The reconstruction quality of FE-FREE was optimal when the resonance offset values fell within the pulse's bandwidth. However, as the resonance offset approached and exceeded the bandwidth, the reconstruction quality significantly deteriorated (Fig. 6.8). Acquisition of only the transverse signal fails to acquire the whole magnetization trajectory. As a result, the complex FT distributes energy amongst the positive and negative frequencies symmetrically around the zeroth frequency. Only one copy was shown in results. Experimental 1D PE-FREE images showed all three chambers object, B_1 field distortions, and B_0 inhomogeneity in each chamber (Fig. 6.10). Applying a 2D FT to the phase-encoded echoes, the chemical shift dimension was able to show the line width of each chamber. Experimental 1D FE-FREE images simply showed a distorted three chamber object (Fig. 6.9), no chemical shift information was available. Ring down limited the available signal, while the Fourier transformation limited the maximum available bandwidths. Despite this, the rotary echo was able to be sufficiently sampled to enable the reconstruction of three chambers.

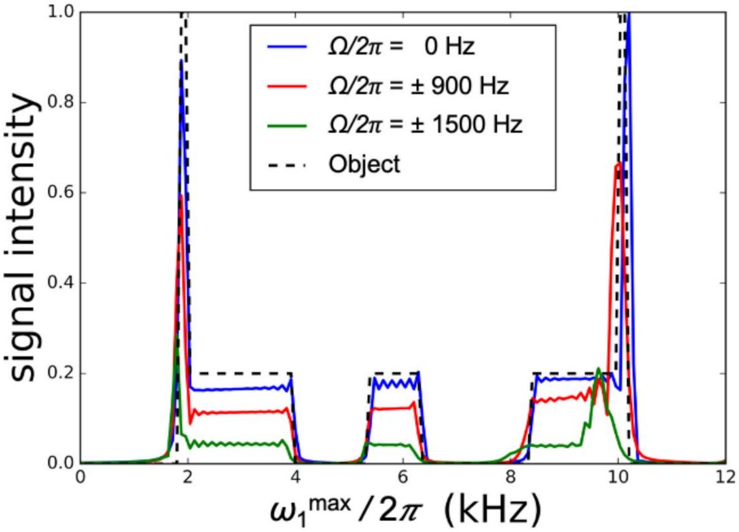

Fig. 6.8. Simulation demonstrations for a 1D FE-FREE experiment. Spins were assumed to begin on the transverse plane. A linear $\gamma B_1/2\pi$ gradient of 12 kHz transmitted the first and second AFP. The first and second AFP had a time-bandwidth product of 0.0125 s · 2000 Hz and 0.0250 s · 2000 Hz, respectively. 800 points were collected throughout the second pulse. The complex Fourier Transform (FT) reconstructed the middle 400 points. Due to the missing z-magnetization, the complex FT produced two copies of the object about the zeroth frequency. The figure shows the positive frequency copy across different off-resonant conditions. The object reconstruction begins to severely degrade once the resonance is outside the A of the pulse.

6.5 Discussion:

We introduced a novel methodology for frequency encoding using B_1 field gradients and AFPs - the first of its kind. The goal of radiofrequency imaging approaches is to offer alternatives to B_0 gradient coils in novel MRI system designs. Most RF imaging approaches focus on phase-encoding [71], [83], [89], which images slowly, encoding

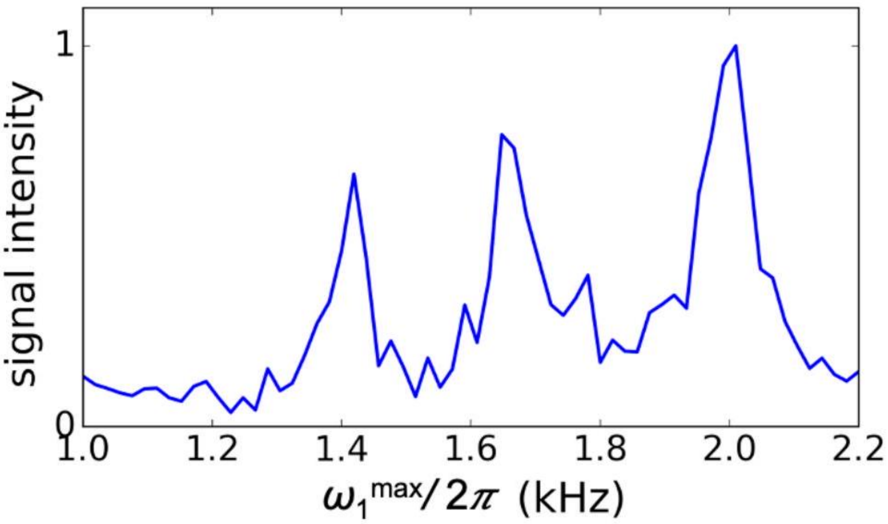

Fig. 6.9. The reconstruction of the FE-FREE rotary echo shows three chambers. The Fourier transform reconstructed the middle 64 points of the data. Distortions are present likely due to higher BW pulses and poor performance of the Fourier reconstruction.

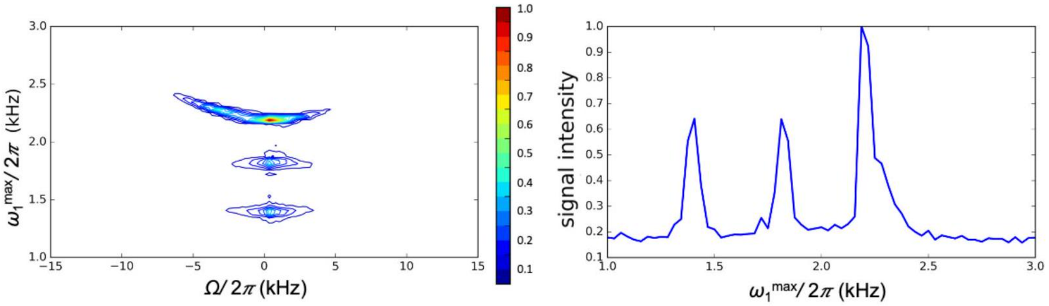

Fig. 6.10. The PE-FREE data was reconstructed using a 2D Fourier transformation. A 2D contour plot (left) shows the three chambers and the B_1 and B_0 inhomogeneities present in the chambers. A 1D projection was generated (right) to compare against FE-FREE (Fig. 6.9) by summing the rows of the 2D contour plot.

schemes that required specialized coils or coil arrays [89], which limit imaging applications, or perform poorly in off-resonance conditions [65], which limit applications in compact magnets. FE-FREE leverages similar encoding principles as PE-FREE, namely the utilization of adiabatic pulses. These adiabatic pulses control the effective magnetic field to ensure uniform spin rotation across variations in B_1 and B_0.

These initial proof-of-concept experiments one-dimensionally imaged a phantom in a highly inhomogeneous, compact 0.5 T Halbach; the magnet had a max of 12 kHz ^{1}H linewidth across the phantom. The magnet had no passive shims, B_0 gradient coils, or Faraday cage. The inhomogeneity of the magnet and lack of infrastructure (e.g., Faraday cage, dedicated gradient coils) would limit most imaging approaches. FREE principles enabled us to produce 1D projections using both PE - and FE - FREE using only a simple surface coil. These results, although one-dimensional, show the capability of FREE approaches to image with non-traditional MRI magnet designs. Expanding the abilities of FREE through advanced hardware and pulse sequences would promote the further use of magnets like the highly affordable, yet inhomogeneous 0.5 T magnet used here. Merging FE - and PE - FREE and using the magnets natural B_0 inhomogeneity to slice-select could enable volumetric imaging. A compact magnet powered by FREE, with no B_0 gradient coils, could offer clinical solutions at a much lower cost than traditional systems.

Conceptually, FE-FREE shares strong similarities with traditional frequency encoding GRE sequences. The dephasing lobe of a *GRE* brings spins to a $-\mathrm{k}_{\mathrm{max}}$, while the refocusing lobe sweeps about k-space to $+\mathrm{k}_{\mathrm{max}}$. FE-FREE mirrors this k-space trajectory with the first and second AFP acting as the dephasing and refocusing lobes, respectively. Likewise, the area of the lobes and AFPs determine the resulting k-values. Similarities between FE-FREE and *GRE* approaches could enable traditional *GRE* post-processing tools to be easily translated to FE-FREE to improve reconstructions, sampling, and trajectories.

In its current implementation, a portion of the gap time is occupied by ringdown delays. Longer ringdown periods are observed due to poor coil loading, high Q-values, and imaging at lower magnetic fields. The duration of ringdown is directly proportional to the strength of the polarizing field. FE-FREE imaging specifically targets mid to low field scanners, where RF coils dissipate energy over an extended period. To ensure the utilization of all acquired data, it is imperative to enable optimized hardware (like Q switching [92]) or post-processing [93] techniques that minimize τ_{rd} . The removal of ringdown will remain a crucial focus in the ongoing development of FE-FREE.

Non-linearities in FE-FREE's k-space trajectory prevented the Fourier transformation from reconstructing all data. Modern approaches could reconstruct a nonlinear k-space trajectory (e.g., gridding, ramp sampling, non-uniform Fourier transformations, or model-reconstructions [86], [93]). But in instances where $A > \gamma B_1$, nonlinearities arise in the spins' spatial frequencies. Spatial-frequency variation during the pulse varies across pulse types (Fig 6.4) has a greater hindrance on reconstruction approaches. To reconstruct these nonlinearities, a more detailed or advanced reconstruction is required. Otherwise, defining the B_1 gradient to hold the condition of $\gamma B_1 \gg A$ removes spatial frequency variation, but higher γB_1 fields could introduce unacceptable levels of SAR.

Unlike a spin-echo, FE-FREE's rotary echo uniquely refocuses in the y'z' plane. Dependent on the pulse selection, adiabatic condition, and strength of the B_1 gradient, the rotary echo has a $x'-, y'-$, and $z'-$ component. Traditional RF approaches detect the transverse components but miss the longitudinal component. Not detecting the longitudinal component reduces SNR and could produce a copy of the object. The object copy arises from the acquired x' and y' component lacking the conjugate relationship that the complex FT requires. If the data is transformed into a second rotating frame, inverting at a specific angular velocity, the x$''$ and y$''$ hold the appropriate relationship and a rotary echo becomes equivalent to a spin-echo in the first rotating frame. However, to appropriately transform into the second rotating frame, a calculation or measurement of the $M_{\mathrm{z}}(t)$ component is required. In the z-direction, only the spins' nutation is available, which is in the kHz range. Longitudinal detection then requires the special development of low-frequency RF sensors that can measure the Rabi frequencies.

The surface coil proved effective at demonstrating FE-FREE's initial experiments, but it introduced spatial nonlinearities, residual M_{z} components, and a limited FOV. A surface coil transmits a nonlinear B_1 gradient that spatially distorts the image and varies the excitation flip angle [83], [84]. Distortion-correction algorithms have shown to be effective at correcting surface coil distortions in FREE, but the spatial variation of flip angles introduced large amounts of residual M_{z} that spin-locked to the AFP's $\mathbf{B}_{\mathrm{eff}}$ trajectory. Magnetization that is spin-locked, currently, does not spatially encode. Correlation removes the prominent spin-locked component (Fig 6.5) but filters out some signal. Advanced RF hardware that can transmit in a homogenous mode (e.g., a bird-cage) would minimize spatial variations in flip angle and improve SNR. The 10 cm surface coil had an approximate max FOV of 10 cm. Spins outside of the coils reach cannot be imaged. Coil designs for specific anatomy or that can image the whole body would expand FREE's imaging capabilities. Promising approaches are already demonstrating how to create highly linear B_1 gradients across large volumes [94]. Overall, improvements in RF coils designed for B_1 encoding would improve many aspects of FREE imaging.

In its first iteration, FE-FREE introduces minimal delays between its dephasing and refocusing pulse; as a result, it only measures the rotary echo. The rotary echo's $TE = T_\mathrm{p}^\mathrm{exc} + 2T_\mathrm{p}{}^\mathrm{dp}$, where $T_\mathrm{p}^\mathrm{exc}$ is the pulse length of the excitation pulse. The refocused spins relax in the presence of the RF field - otherwise known as $T_{2\rho}$ relaxation. $T_{2\rho}$ depends on the RF pulse and spins' overall environment. As applied, the spins $T_{2\rho}$ vary across space due to the B_1 gradient, which may expand FE-FREE sensitivity to $T_{2\rho}$ contrast. $T_{2\rho}$ contrast provides unique benefits to detecting slow molecular dynamics [95] and can be much longer than T_2 [95], [96]. The length of $T_{2\rho}$ could enable the acquisition of many rotary echoes during one experiment - potentially enabling one-shot imaging. Additional contrasts, like T_1 and T_2, could be introduced by varying the delays between the pulses, refocusing the spin-echo, which is produced by the first AFP, or varying the TR.

Typically, B_1 imaging introduces more SAR than B_0 approaches. SAR is $B_0{}^2$-dependent. The MRI field has seen a recent rise in low to mid-field imaging technology [59], [97], and their clinical applications are being thoroughly investigated. B_1 imaging could fit nicely with a low or mid-field scanner. Lower magnetic fields would allow simple, yet accurate, B_1 mapping simulations, through Biot-Savart, and permit FREE to bring its full capabilities to a scanner. A low- to mid- field scanners seems to support FREE's goal of designing a B_0-gradientless system best.

6.6 Conclusion:

In recent years, there has been a surge of interest in the development of affordable, accessible, and portable MRI scanners. The re-emergence of ultra-low, low, and mid-field scanners has gained significant attention and show no signs of slowing down in their development. Among these innovations, B_1 imaging approaches, such as FREE, present themselves as a potent addition to low-cost MRI systems. If B_1 imaging approaches can progress to a point where they can effectively replace B_0 gradient coils, the prospect of a low-field system without B_0 gradient coils becomes particularly intriguing. Such a system would hold immense potential for the $\sim 90\%$ of the world where MRI remains inaccessible.

Chapter 7

Future Directions

In this thesis, we presented the progress towards the development of novel B_1 encoding approaches that could potentially surmount B_0 gradient coils. Two methods were developed: phase-encoded frequency-modulated Rabi encoded echoes and frequency-encoded frequency-modulated Rabi encoded echoes (PE- and FE- FREE). Both approaches share similarities in their encoding principles, and they aim to replace the traditional phase- and frequency- encoding done by B_0 gradient coils. Prior to FREE, a slew of B_1 imaging approaches had been developed. Yet, all approaches suffered from resonance offset sensitivity. FREE imaging was developed to enable a viable and effective B_1 imaging approach that could be used in compact and inhomogeneous magnets like the magnet used in chapters 3 and 5.

PE-FREE is a double spin-echo approach and has the highest resistance to resonance offset. If sufficient RF power is available, PE-FREE sequences could tolerate resonance offsets on the order of tens of kilohertz. Additionally, it is easily reconstructed using traditional Fourier approaches since the data are phase-encoded spin-echoes. FE-FREE on the other hand presents a more complex implementation and reconstruction. Like SWIFT, FE-FREE requires near simultaneous transmit and receive. Although STAR was not utilized in this work, gapping the pulses proved effective. FE-FREE encodes a rotary echo. Uniquely, the rotary echo refocuses during the inversion of a plane leading to part of the signal of interest being present in the z-direction. The z-magnetization of interest is currently undetectable to traditional RF approaches forcing reconstruction with missing information. Additionally, FE-

FREE encoding follows a nonlinear k-space trajectory and encoding scheme - forcing the use of non-Fourier reconstruction approaches.

This work showed how to encode and image using both FE- and PE- FREE, despite the experimental difficulties of FE-FREE. In the future, if advances in hardware can facilitate STAR, more effective gapping, or z-magnetization detection. The potential of FE-FREE could be fully exploited. 2D and 3D pulse sequences that build on FE- and PE- FREE sequences are subsequently easily imagined. These include many of the traditional B_0 2D and 3D pulse sequences like: radial, EPI, and many others.

If FREE technologies can progress to a point where they can effectively replace B_0 gradients, FREE approaches could be merged into scanners developed in chapter 3 and be a potent addition to low-field scanners. Such a package would be affordable, accessible, and clinically valuable. The merger of FREE technologies with compact and affordable magnets could enable the creation of accessible and clinically valuable scanners. Such a system would hold immense potential for the approximate 90 percent of the world where MRI remains inaccessible.

References

[1] S. Geethanath and J. T. Vaughan, "Accessible magnetic resonance imaging: A review," en, *Journal of Magnetic Resonance Imaging*, vol. 49, no. 7, e65–e77, Jun. 2019, ISSN: 1053-1807, 1522-2586. DOI: `10.1002/jmri.26638`. [Online]. Available: `https://onlinelibrary.wiley.com/doi/10.1002/jmri.26638` (visited on 08/11/2023).

[2] E. J. van Beek, C. Kuhl, Y. Anzai, *et al.*, "Value of mri in medicine: More than just another test?" *Journal of Magnetic Resonance Imaging*, vol. 49, no. 7, e14–e25, 2019.

[3] L. L. Wald, P. C. McDaniel, T. Witzel, J. P. Stockmann, and C. Z. Cooley, "Low-cost and portable MRI," en, *Journal of Magnetic Resonance Imaging*, vol. 52, no. 3, pp. 686–696, Sep. 2020, ISSN: 1053-1807, 1522-2586. DOI: `10.1002/jmri.26942`. [Online]. Available: `https://onlinelibrary.wiley.com/doi/10.1002/jmri.26942` (visited on 02/09/2023).

[4] "Introduction to MRI Coils and Magnets," in *Magnetic Resonance Imaging*, John Wiley & Sons, Ltd, 2014, pp. 823–857, ISBN: 978-1-118-63395-3. DOI: `https://doi.org/10.1002/9781118633953.ch27`. [Online]. Available: `https://onlinelibrary.wiley.com/doi/abs/10.1002/9781118633953.ch27`.

[5] D. Griffiths, *Introduction to Electrodynamics*. Prentice Hall, 1998.

[6] M. H. Levitt, *Spin dynamics: basics of nuclear magnetic resonance*. John Wiley & Sons, 2013.

[7] "The Quantum Mechanical Basis of Precession and Excitation," in *Magnetic Resonance Imaging*, John Wiley & Sons, Ltd, 2014, pp. 67–83, ISBN: 978-1-118-

63395-3. [Online]. Available: `https://onlinelibrary.wiley.com/doi/abs/10.1002/9781118633953.ch5`.

[8] "The Quantum Mechanical Basis of Thermal Equilibrium and Longitudinal Relaxation," in *Magnetic Resonance Imaging*, John Wiley & Sons, Ltd, 2014, pp. 85–94, ISBN: 978-1-118-63395-3.

[9] "Magnetization, Relaxation, and the Bloch Equation," in *Magnetic Resonance Imaging*, John Wiley & Sons, Ltd, 2014, pp. 53–66, ISBN: 978-1-118-63395-3. DOI: `https://doi.org/10.1002/9781118633953.ch4`. [Online]. Available: `https://onlinelibrary.wiley.com/doi/abs/10.1002/9781118633953.ch4`.

[10] O. Sørensen, "Product operator formalism for the description of nmr pulse experiments," *Progress in Nuclear Magnetic Resonance Spectroscopy*, 1984.

[11] "A Closer Look at Radiofrequency Pulses," in *Magnetic Resonance Imaging*, John Wiley & Sons, Ltd, 2014, pp. 375–412, ISBN: 978-1-118-63395-3. DOI: `https://doi.org/10.1002/9781118633953.ch16`. [Online]. Available: `https://onlinelibrary.wiley.com/doi/abs/10.1002/9781118633953.ch16`.

[12] M. A. BERNSTEIN, K. F. KING, and X. J. ZHOU, "CHAPTER 3 - BASIC RADIOFREQUENCY PULSE FUNCTIONS," in *Handbook of MRI Pulse Sequences*, M. A. BERNSTEIN, K. F. KING, and X. J. ZHOU, Eds., Burlington: Academic Press, 2004, pp. 67–95, ISBN: 978-0-12-092861-3. DOI: `https://doi.org/10.1016/B978-012092861-3/50007-8`. [Online]. Available: `https://www.sciencedirect.com/science/article/pii/B9780120928613500078`.

[13] "Classical Response of a Single Nucleus to a Magnetic Field," in *Magnetic Resonance Imaging*, John Wiley & Sons, Ltd, 2014, pp. 19–36, ISBN: 978-1-118-63395-3. DOI: `https://doi.org/10.1002/9781118633953.ch2`. [Online]. Available: `https://onlinelibrary.wiley.com/doi/abs/10.1002/9781118633953.ch2`.

[14] F. Bloch, "Nuclear induction," *Physical Review*, 1946.

[15] M. A. BERNSTEIN, K. F. KING, and X. J. ZHOU, "CHAPTER 14 - BASIC PULSE SEQUENCES," in *Handbook of MRI Pulse Sequences*, M. A. BERNSTEIN, K. F. KING, and X. J. ZHOU, Eds., Burlington: Academic Press, 2004, pp. 579–647, ISBN: 978-0-12-092861-3. DOI: `https://doi.org/10.1016/B978-012092861-3/50021-2`. [Online]. Available: `https://www.sciencedirect.com/science/article/pii/B9780120928613500212`.

[16] "Spin Density, T1, and T2 Quantification Methods in MR Imaging," in *Magnetic Resonance Imaging*, John Wiley & Sons, Ltd, 2014, pp. 637–667, ISBN: 978-1-118-63395-3. DOI: `https://doi.org/10.1002/9781118633953.ch22`. [Online]. Available: `https://onlinelibrary.wiley.com/doi/abs/10.1002/9781118633953.ch22`.

[17] C. Brian, *Nuclear Magnetic Resonance and Relaxation*. Cambridge University Press, 2005.

[18] J. C. Sharp1, "Mri using radiofrequency magnetic field phase gradients," *Magnetic Resonance in Medicine*, 2010.

[19] E. Hahn, "Spin echoes," *Physical Review*, 1950.

[20] "Rotating Reference Frames and Resonance," in *Magnetic Resonance Imaging*, John Wiley & Sons, Ltd, 2014, pp. 37–51, ISBN: 978-1-118-63395-3. DOI: `https://doi.org/10.1002/9781118633953.ch3`. [Online]. Available: `https://onlinelibrary.wiley.com/doi/abs/10.1002/9781118633953.ch3`.

[21] J. Pauly, D. Nishimura, and A. Macovski, "A k-space analysis of small-tip-angle excitation," *Journal of Magnetic Resonance (1969)*, vol. 81, no. 1, pp. 43–56, 1989, ISSN: 0022-2364. DOI: `https://doi.org/10.1016/0022-2364(89)90265-5`. [Online]. Available: `https://www.sciencedirect.com/science/article/pii/0022236489902655`.

[22] M. Garwood and L. DelaBarre, "The Return of the Frequency Sweep: Designing Adiabatic Pulses for Contemporary NMR," en,

[23] M. A. BERNSTEIN, K. F. KING, and X. J. ZHOU, “CHAPTER 6 - ADIABATIC RADIOFREQUENCY PULSES,” in *Handbook of MRI Pulse Sequences*, M. A. BERNSTEIN, K. F. KING, and X. J. ZHOU, Eds., Burlington: Academic Press, 2004, pp. 177–212, ISBN: 978-0-12-092861-3. DOI: `https://doi.org/10.1016/B978-012092861-3/50010-8`. [Online]. Available: `https://www.sciencedirect.com/science/article/pii/B9780120928613500108`.

[24] A. Tannús and M. Garwood, “Adiabatic pulses,” en, *NMR in Biomedicine*, vol. 10, no. 8, pp. 423–434, Dec. 1997, ISSN: 0952-3480, 1099-1492. DOI: `10.1002/(SICI)1099-1492(199712)10:8<423::AID-NBM488>3.0.CO;2-X`. [Online]. Available: `https://onlinelibrary.wiley.com/doi/10.1002/(SICI)1099-1492(199712)10:8%3C423::AID-NBM488%3E3.0.CO;2-X` (visited on 02/09/2023).

[25] J. Baum, “Broadband and adiabatic inversion of a two-level system by phase-modulated pulses,” *Physical Review A*, 1985.

[26] T. Froelich, M. Mullen, and M. Garwood, “MRI exploiting frequency-modulated pulses and their nonlinear phase,” en, *Journal of Magnetic Resonance*, vol. 318, p. 106 779, Sep. 2020, ISSN: 10907807. DOI: `10.1016/j.jmr.2020.106779`. [Online]. Available: `https://linkinghub.elsevier.com/retrieve/pii/S1090780720300975` (visited on 06/05/2023).

[27] M. Goldman, “Formal theory of spin-lattice relaxation,” *Advances in Magnetic Resonance*, 2001.

[28] K. K. Papas, R. C. Long, A. Sambanis, and I. Constantinidis, “Development of a bioartificial pancreas: II. Effects of oxygen on long-term entrapped TC3 cell cultures,” en, *Biotechnology and Bioengineering*, vol. 66, no. 4, pp. 231–237, 1999, ISSN: 0006-3592, 1097-0290. DOI: `10.1002/(SICI)1097-0290(1999)66:4<231::AID-BIT4>3.0.CO;2-U`. [Online]. Available: `https://onlinelibrary.wiley.com/doi/10.1002/(SICI)1097-0290(1999)66:4%3C231::AID-BIT4%3E3.0.CO;2-U` (visited on 07/21/2023).

[29] G. Basile, M. Qadir, F. Mauvais-Jarvis, *et al.*, “Emerging diabetes therapies: Bringing back the β-cells,” en, *Molecular Metabolism*, vol. 60, p. 101 477, Jun. 2022, ISSN: 22128778. (visited on 07/21/2023).

[30] M. R. Rickels and R. P. Robertson, "Pancreatic Islet Transplantation in Humans: Recent Progress and Future Directions," en, *Endocrine Reviews*, vol. 40, no. 2, pp. 631–668, Apr. 2019, ISSN: 0163-769X, 1945-7189. DOI: `10.1210/er.2018-00154`. [Online]. Available: `https://academic.oup.com/edrv/article/40/2/631/5239681` (visited on 07/21/2023).

[31] B. Ludwig, A. Reichel, A. Steffen, *et al.*, "Transplantation of human islets without immunosuppression," en, *Proceedings of the National Academy of Sciences*, vol. 110, no. 47, pp. 19 054–19 058, Nov. 2013, ISSN: 0027-8424, 1091-6490. DOI: `10.1073/pnas.1317561110`. [Online]. Available: `https://pnas.org/doi/full/10.1073/pnas.1317561110` (visited on 05/02/2023).

[32] V. Iacovacci, L. Ricotti, A. Menciassi, and P. Dario, "The bioartificial pancreas (BAP): Biological, chemical and engineering challenges," en, *Biochemical Pharmacology*, vol. 100, pp. 12–27, Jan. 2016, ISSN: 00062952. DOI: `10.1016/j.bcp.2015.08.107`. [Online]. Available: `https://linkinghub.elsevier.com/retrieve/pii/S0006295215005663` (visited on 05/02/2023).

[33] K. E. Smith, A. C. Kelly, C. G. Min, *et al.*, "Acute Ischemia Induced by High-Density Culture Increases Cytokine Expression and Diminishes the Function and Viability of Highly Purified Human Islets of Langerhans," en, *Transplantation*, vol. 101, no. 11, pp. 2705–2712, Nov. 2017, ISSN: 0041-1337. DOI: `10.1097/TP.0000000000001714`. [Online]. Available: `https://journals.lww.com/00007890-201711000-00016` (visited on 07/21/2023).

[34] J. D. Gross, R. Long, I. Constantinidis, and A. Sambanis, "Monitoring of dissolved oxygen and cellular bioenergetics within a pancreatic substitute," en, *Biotechnology and Bioengineering*, vol. 98, no. 1, pp. 261–270, Sep. 2007, ISSN: 00063592, 10970290. DOI: `10.1002/bit.21421`. [Online]. Available: `https://onlinelibrary.wiley.com/doi/10.1002/bit.21421` (visited on 07/21/2023).

[35] K. E. Dionne, C. K. Colton, and M. L. Yarmush, "Effect of Hypoxia on Insulin Secretion by Isolated Rat and Canine Islets of Langerhans," en, vol. 42, 1993.

[36] U. Barkai, G. C. Weir, C. K. Colton, *et al.*, "Enhanced Oxygen Supply Improves Islet Viability in a New Bioartificial Pancreas," en, *Cell Transplantation*, vol. 22,

no. 8, pp. 1463–1476, Aug. 2013, ISSN: 0963-6897, 1555-3892. DOI: `10.3727/096368912X657341`. [Online]. Available: `http://journals.sagepub.com/doi/10.3727/096368912X657341` (visited on 05/02/2023).

[37] D. Emerich and G. Orive, *Cell Therapy, Current Status and Future Directions.*

[38] K. K. Papas, "Effect of oxygen supply on the size of implantable islet-containing encapsulation devices," *Panminerva Med*, no. 58, pp. 7–72,

[39] T. Suszynski, E. Avgoustiniatos, S. Stein, E. Falde, B. Hammer, and K. Papas, "Assessment of Tissue-Engineered Islet Graft Viability by Fluorine Magnetic Resonance Spectroscopy," en, *Transplantation Proceedings*, vol. 43, no. 9, pp. 3221–3225, Nov. 2011, ISSN: 00411345. DOI: `10.1016/j.transproceed.2011.09.009`. [Online]. Available: `https://linkinghub.elsevier.com/retrieve/pii/S0041134511011845` (visited on 08/04/2023).

[40] J. R. Griffiths and S. P. Robinson, "The OxyLite: A Ⓡbre-optic oxygen sensor," en, *The British Journal of Radiology*, 1999.

[41] N. A. Wisniewski, S. P. Nichols, S. J. Gamsey, *et al.*, "Tissue-Integrating Oxygen Sensors: Continuous Tracking of Tissue Hypoxia," en, in *Oxygen Transport to Tissue XXXIX*, H. J. Halpern, J. C. LaManna, D. K. Harrison, and B. Epel, Eds., vol. 977, Cham: Springer International Publishing, 2017, pp. 377–383, ISBN: 978-3-319-55229-3 978-3-319-55231-6. DOI: `10.1007/978-3-319-55231-6_49`. [Online]. Available: `http://link.springer.com/10.1007/978-3-319-55231-6_49` (visited on 07/30/2023).

[42] J. Ruiz-Cabello, B. P. Barnett, P. A. Bottomley, and J. W. Bulte, "Fluorine (19F) MRS and MRI in biomedicine," en, *NMR in Biomedicine*, vol. 24, no. 2, pp. 114–129, Feb. 2011, ISSN: 09523480. DOI: `10.1002/nbm.1570`. [Online]. Available: `https://onlinelibrary.wiley.com/doi/10.1002/nbm.1570` (visited on 05/02/2023).

[43] R. P. Mason, H. Shukla, and P. P. Antich, "In vivo oxygen tension and temperature: Simultaneous determination using19F NMR spectroscopy of perfluorocarbon," en, *Magnetic Resonance in Medicine*, vol. 29, no. 3, pp. 296–302, Mar. 1993, ISSN: 07403194, 15222594. DOI: `10.1002/mrm.1910290304`. [On-

line]. Available: `https://onlinelibrary.wiley.com/doi/10.1002/mrm.1910290304` (visited on 05/02/2023).

[44] S. A. Einstein, B. P. Weegman, M. T. Firpo, K. K. Papas, and M. Garwood, "Development and Validation of Noninvasive Magnetic Resonance Relaxometry for the *In Vivo* Assessment of Tissue-Engineered Graft Oxygenation," en, *Tissue Engineering Part C: Methods*, vol. 22, no. 11, pp. 1009–1017, Nov. 2016, ISSN: 1937-3384, 1937-3392. DOI: `10.1089/ten.tec.2016.0106`. [Online]. Available: `https://www.liebertpub.com/doi/10.1089/ten.tec.2016.0106` (visited on 05/02/2023).

[45] C. Hugon, F. D'Amico, G. Aubert, and D. Sakellariou, "Design of arbitrarily homogeneous permanent magnet systems for NMR and MRI: Theory and experimental developments of a simple portable magnet," en, *Journal of Magnetic Resonance*, 2010.

[46] P. Elleaume, O. Chubar, and J. Chavanne, "Computing 3D magnetic fields from insertion devices," en, in *Proceedings of the 1997 Particle Accelerator Conference (Cat. No.97CH36167)*, vol. 3, Vancouver, BC, Canada: IEEE, 1998, pp. 3509–3511, ISBN: 978-0-7803-4376-4. DOI: `10.1109/PAC.1997.753258`. [Online]. Available: `http://ieeexplore.ieee.org/document/753258/` (visited on 07/26/2023).

[47] A. Tannús, *Subsistema multiplataforma para controle de aquisição, visualização e organização dedados de espectrômetro digital de RM: ToRM Console*, Dec. 2015.

[48] D. C. Pizetta, "A Framework for Programming Magnetic Resonance Systems," Ph.D. dissertation, University of Sao Paulo.

[49] D. C. Pizetta, *ToRM-IDE— Integrated development environment for magnetic resonance applications.* Brazil.

[50] R. Crouch, S. Hurlbert, and A. Ragouzeos, "An iterative linear method for calculation of spin-lattice relaxation times," en, *Journal of Magnetic Resonance (1969)*, vol. 49, no. 3, pp. 371–382, Oct. 1982, ISSN: 00222364. DOI: `10.1016/`

`0022-2364(82)90251-7`. [Online]. Available: `https://linkinghub.elsevier.com/retrieve/pii/0022236482902517` (visited on 05/02/2023).

[51] M. Sass and D. Ziessow, "Error analysis for optimized inversion recovery spin-lattice relaxation measurements," en, *Journal of Magnetic Resonance (1969)*, vol. 25, no. 2, pp. 263–276, Feb. 1977, ISSN: 00222364. DOI: `10.1016/0022-2364(77)90021-X`. [Online]. Available: `https://linkinghub.elsevier.com/retrieve/pii/002223647790021X` (visited on 05/02/2023).

[52] P. A. Bottomley and R. Ouwerkerk, "Optimum flip-angles for exciting NMR with uncertainT1 values," en, *Magnetic Resonance in Medicine*, vol. 32, no. 1, pp. 137–141, Jul. 1994, ISSN: 07403194, 15222594. (visited on 05/02/2023).

[53] P. A. Bottomley, T. H. Foster, R. E. Argersinger, and L. M. Pfeifer, "A review of normal tissue hydrogen NMR relaxation times and relaxation mechanisms from 1-100 MHz: Dependence on tissue type, NMR frequency, temperature, species, excision, and age: Review Article: NMR relaxation in tissue," en, *Medical Physics*, vol. 11, no. 4, pp. 425–448, Jul. 1984, ISSN: 00942405. DOI: `10.1118/1.595535`. [Online]. Available: `http://doi.wiley.com/10.1118/1.595535` (visited on 05/02/2023).

[54] D. Zhao, L. Jiang, and R. P. Mason, "Measuring Changes in Tumor Oxygenation," en, in *Methods in Enzymology*, vol. 386, Elsevier, 2004, pp. 378–418, ISBN: 978-0-12-182791-5. (visited on 05/15/2023).

[55] P. Parhami and B. M. Fung, "Fluorine-19 relaxation study of perfluoro chemicals as oxygen carriers," en, *The Journal of Physical Chemistry*, vol. 87, no. 11, pp. 1928–1931, 1983, ISSN: 0022-3654, 1541-5740. (visited on 05/15/2023).

[56] R. Fletcher, "Function Minimization Without Evaluating Derivatives–a Review," en, *The Computer Journal*, vol. 8, no. 1, pp. 33–41, Apr. 1965, ISSN: 0010-4620, 1460-2067. DOI: `10.1093/comjnl/8.1.33`. [Online]. Available: `https://academic.oup.com/comjnl/article-lookup/doi/10.1093/comjnl/8.1.33` (visited on 06/19/2023).

[57] J. Parsa, T. O'Reilly, and A. Webb, "A single-coil-based method for electromagnetic interference reduction in point-of-care low field MRI systems," en, *Journal of Magnetic Resonance*, vol. 346, p. 107 355, Jan. 2023, ISSN: 10907807. DOI: `10.1016/j.jmr.2022.107355`. [Online]. Available: `https://linkinghub.elsevier.com/retrieve/pii/S1090780722002130` (visited on 07/13/2023).

[58] S. A. Srinivas, S. F. Cauley, J. P. Stockmann, *et al.*, "External Dynamic InTerference Estimation and Removal (EDITER) for low field MRI," en, *Magnetic Resonance in Medicine*, vol. 87, no. 2, pp. 614–628, Feb. 2022, ISSN: 0740-3194, 1522-2594. DOI: `10.1002/mrm.28992`. [Online]. Available: `https://onlinelibrary.wiley.com/doi/10.1002/mrm.28992` (visited on 07/13/2023).

[59] Y. Liu, A. T. L. Leong, Y. Zhao, *et al.*, "A low-cost and shielding-free ultra-low-field brain MRI scanner," en, *Nature Communications*, vol. 12, no. 1, p. 7238, Dec. 2021, ISSN: 2041-1723. DOI: `10.1038/s41467-021-27317-1`. [Online]. Available: `https://www.nature.com/articles/s41467-021-27317-1` (visited on 07/13/2023).

[60] "One-Dimensional Fourier Imaging, ϰ-Space, and Gradient Echoes," in *Magnetic Resonance Imaging*, John Wiley & Sons, Ltd, 2014, pp. 141–164, ISBN: 978-1-118-63395-3. DOI: `https://doi.org/10.1002/9781118633953.ch9`. [Online]. Available: `https://onlinelibrary.wiley.com/doi/abs/10.1002/9781118633953.ch9`.

[61] J. Pauly, "A k-space analysis of small-tip-angle excitation," *Journal of Magnetic Resonance*, 1989.

[62] E. Hahn, "Detection of sea-water motion by nuclear precession," *Journal of Geophysical Review*, 1960.

[63] M. A. BERNSTEIN, K. F. KING, and X. J. ZHOU, "CHAPTER 17 - ADVANCED PULSE SEQUENCE TECHNIQUES," in *Handbook of MRI Pulse Sequences*, M. A. BERNSTEIN, K. F. KING, and X. J. ZHOU, Eds., Burlington: Academic Press, 2004, pp. 802–954, ISBN: 978-0-12-092861-3.

[64] "Multi-Dimensional Fourier Imaging and Slice Excitation," in *Magnetic Resonance Imaging*, John Wiley & Sons, Ltd, 2014, pp. 165–206, ISBN: 978-1-118-63395-3. DOI: `https://doi.org/10.1002/9781118633953.ch10`. [Online]. Available: `https://onlinelibrary.wiley.com/doi/abs/10.1002/9781118633953.ch10`.

[65] D. Hoult, "Rotating Frame Zuegmatography," *Journal of Magnetic Resonance*, no. 33, pp. 183–197, May 1979.

[66] J. Stockmann, "Transmit array spatial encoding (trase) using broadband wurst pulses for rf spatial encoding in inhomogenous b0 fields," *Journal of Magnetic Resonance*, 2016.

[67] P. Bohidar, H. Sun, J. C. Sharp, and G. E. Sarty, "The effects of coupled B1 fields in B1 encoded TRASE MRI - A simulation study," en, *Magnetic Resonance Imaging*, vol. 74, pp. 74–83, Dec. 2020, ISSN: 0730725X. DOI: `10.1016/j.mri.2020.09.003`. [Online]. Available: `https://linkinghub.elsevier.com/retrieve/pii/S0730725X20303131` (visited on 06/05/2023).

[68] C. J. Hasselwander and W. A. Grissom, "Bloch-Siegert Phase-Encoded MRI with a Single RF Coil and Frequency-Swept Pulses," en,

[69] L. Sacolick, "B1 mapping by bloch-siegert shift," *Magn. Resonance in Medicine*, 2010.

[70] J. B. Martin, S. A. Srinivas, C. E. Vaughn, H. Sun, M. A. Griswold, and W. A. Grissom, "Selective excitation localized by the Bloch–Siegert shift and a B1+ gradient," *Magnetic Resonance in Medicine*, vol. 88, no. 3, pp. 1081–1097, 2022. DOI: `https://doi.org/10.1002/mrm.29271`. [Online]. Available: `https://onlinelibrary.wiley.com/doi/abs/10.1002/mrm.29271`.

[71] D. Canet, "Radiofrequency field gradient experiments," en, *Progress in Nuclear Magnetic Resonance Spectroscopy*, vol. 30, no. 1-2, pp. 101–135, Mar. 1997, ISSN: 00796565. DOI: `10.1016/S0079-6565(96)01031-X`. [Online]. Available: `https://linkinghub.elsevier.com/retrieve/pii/S007965659601031X` (visited on 02/09/2023).

[72] "Electromagnetic Principles," in *Magnetic Resonance Imaging*, John Wiley & Sons, Ltd, 2014, pp. 893–898, ISBN: 978-1-118-63395-3. DOI: `https://doi.org/10.1002/9781118633953.app1`. [Online]. Available: `https://onlinelibrary.wiley.com/doi/abs/10.1002/9781118633953.app1`.

[73] T. Froelich, "Fast spin-echo approach for accelerated b1 gradient–based mri," *Magnetic Resonance in Medicine*, 2023.

[74] A. Macovski and S. Conolly, "Novel approaches to low-cost MRI," en, *Magnetic Resonance in Medicine*, vol. 30, no. 2, pp. 221–230, Aug. 1993, ISSN: 07403194, 15222594. DOI: `10.1002/mrm.1910300211`. [Online]. Available: `https://onlinelibrary.wiley.com/doi/10.1002/mrm.1910300211` (visited on 08/11/2023).

[75] A. E. Campbell-Washburn, R. Ramasawmy, M. C. Restivo, *et al.*, "Opportunities in Interventional and Diagnostic Imaging by Using High-Performance Low-Field-Strength MRI," en, *Radiology*, vol. 293, no. 2, pp. 384–393, Nov. 2019, ISSN: 0033-8419, 1527-1315. DOI: `10.1148/radiol.2019190452`. [Online]. Available: `http://pubs.rsna.org/doi/10.1148/radiol.2019190452` (visited on 08/11/2023).

[76] P. Radomskij, M. Schmidt, C. Heron, and D. Prasher, "Effect of MRI noise on cochlear function," en, *The Lancet*, vol. 359, no. 9316, pp. 1485–1486, Apr. 2002, ISSN: 01406736. DOI: `10.1016/S0140-6736(02)08423-4`. [Online]. Available: `https://linkinghub.elsevier.com/retrieve/pii/S0140673602084234` (visited on 08/11/2023).

[77] J. C. Sharp and S. B. King, "MRI using radiofrequency magnetic field phase gradients: RF Phase Gradient MRI," en, *Magnetic Resonance in Medicine*, vol. 63, no. 1, pp. 151–161, Jan. 2010, ISSN: 07403194. DOI: `10.1002/mrm.22188`. [Online]. Available: `https://onlinelibrary.wiley.com/doi/10.1002/mrm.22188` (visited on 06/05/2023).

[78] Y. Lee, Y. Han, H. Park, H. Watanabe, M. Garwood, and J.-Y. Park, "New phase-based B_1 mapping method using two-dimensional spin-echo imaging with hyperbolic secant pulses: B_1 Mapping Method Using Spin-Echo Imaging," en, *Magnetic Resonance in Medicine*, vol. 73, no. 1, pp. 170–181, Jan.

2015, ISSN: 07403194. DOI: `10.1002/mrm.25110`. [Online]. Available: `https://onlinelibrary.wiley.com/doi/10.1002/mrm.25110` (visited on 06/05/2023).

[79] J.-Y. Park and M. Garwood, “Spin-echo MRI using π/2 and π hyperbolic secant pulses: Spin-Echo MRI Using Hyperbolic Secant Pulses,” en, *Magnetic Resonance in Medicine*, vol. 61, no. 1, pp. 175–187, Jan. 2009, ISSN: 07403194. DOI: `10.1002/mrm.21822`. [Online]. Available: `https://onlinelibrary.wiley.com/doi/10.1002/mrm.21822` (visited on 06/05/2023).

[80] L. A. Shepp and B. F. Logan, “The fourier reconstruction of a head section,” *IEEE Transactions on Nuclear Science*, vol. 21, no. 3, pp. 21–43, 1974. DOI: `10.1109/TNS.1974.6499235`.

[81] M. J. Martins, “Espectrômetro para uso em sistemas de ressonância magnética e sistemas de ressonância magnética,” BR102015000624-1.

[82] D. C. Pizetta, “PyMR—a framework for programming magnetic resonance systems.,” BR512019001829-0.

[83] E. Torres, T. Froelich, L. DeLaBarre, *et al.*, “B1-gradient based MRI using Frequency-modulated Rabi Encoded Echoes (FREE),” en,

[84] P. Wang, T. Froelich, E. Torres, *et al.*, “Correcting image distortions from a nonlinear B1-gradient field in frequency-modulated Rabi-encoded echoes,” en, *Magnetic Resonance in Medicine*, mrm.29549, Dec. 2022, ISSN: 0740-3194, 1522-2594. DOI: `10.1002/mrm.29549`. [Online]. Available: `https://onlinelibrary.wiley.com/doi/10.1002/mrm.29549` (visited on 02/09/2023).

[85] J. Hennig, A. M. Welz, G. Schultz, *et al.*, “Parallel imaging in non-bijective, curvilinear magnetic field gradients: A concept study,” en, *Magnetic Resonance Materials in Physics, Biology and Medicine*, vol. 21, no. 1-2, p. 5, Mar. 2008, ISSN: 0968-5243, 1352-8661. DOI: `10.1007/s10334-008-0105-7`. [Online]. Available: `https://link.springer.com/10.1007/s10334-008-0105-7` (visited on 06/05/2023).

[86] M. Mullen and M. Garwood, "Contemporary approaches to high-field magnetic resonance imaging with large field inhomogeneity," en, *Progress in Nuclear Magnetic Resonance Spectroscopy*, vol. 120-121, pp. 95–108, Oct. 2020, ISSN: 00796565. DOI: `10.1016/j.pnmrs.2020.07.003`. [Online]. Available: `https://linkinghub.elsevier.com/retrieve/pii/S0079656520300261` (visited on 06/05/2023).

[87] A. Janke, H. Zhao, G. J. Cowin, G. J. Galloway, and D. M. Doddrell, "Use of spherical harmonic deconvolution methods to compensate for nonlinear gradient effects on MRI images," en, *Magnetic Resonance in Medicine*, vol. 52, no. 1, pp. 115–122, Jul. 2004, ISSN: 0740-3194, 1522-2594. DOI: `10.1002/mrm.20122`. [Online]. Available: `https://onlinelibrary.wiley.com/doi/10.1002/mrm.20122` (visited on 06/05/2023).

[88] F. X. Shen, S. M. Wolf, R. G. Gonzalez, and M. Garwood, "Ethical Issues Posed by Field Research Using Highly Portable and Cloud-Enabled Neuroimaging," en, *Neuron*, vol. 105, no. 5, pp. 771–775, Mar. 2020, ISSN: 08966273. DOI: `10.1016/j.neuron.2020.01.041`. [Online]. Available: `https://linkinghub.elsevier.com/retrieve/pii/S0896627320300684` (visited on 08/11/2023).

[89] e. a. Hongwei Sun, "The twisted solenoid rf phase gradient transmit coil for trase imaging," *JMR*, 2019.

[90] I. Solomon, "Rotary spin echoes," *Physical Review Letters*, 1959.

[91] e. a. Djaudat I, "Sweep imaging with fourier transformation (swift)," *Journal of Magnetic Resonance*, 2006.

[92] *A Q-switch system for an MRI RF coil operating at 2.5 MHz*, 2016.

[93] M. Akcakaya, *Magnetic Resonance Image Reconstruction: Theory, Methods, and Applications*. Academic Press, 2022.

[94] *Sequential Gradient Superposition Frequency Modulated Rabi Encoded Echoes*, 2022.

[95] e. a. Michaeli S, "T2ρ and t1ρ adiabatic relaxations and contrasts," *Current Analytical Chemistry*, 2008.

[96] e. a. Michaeli S, “T1ρ mri contrast in the human brain: Modulation of the longitudinal rotating frame relaxation shutter-speed during an adiabatic rf pulse.,” *Journal of Magnetic Resonance*, 2006.

[97] e. a. Sarracanie M, “Low-field mri: How low can we go? a fresh view on an old debate,” *Frontiers in Physics*, 2020.